Direct chirality distinction with nuclear magnetic resonance

Zur Erlangung des akademischen Grades eines

DOKTORS DER INGENIEURWISSENSCHAFTEN
(Dr.-Ing.)

von der KIT -Fakultät für Maschinenbau des

Karlsruher Instituts für Technologie (KIT)

angenommene

DISSERTATION

von

M.Sc. Sagar Wadhwa

Tag der mündlichen Prüfung:	25.07.2024
Hauptreferent:	Prof. Dr. Jan G. Korvink
Korreferent:	Prof. Dr. Stefan Bräse

Kurzfassung

Die Magnetresonanzspektroskopie (MR) ist eine leistungsfähige spektroskopische Methode zur Aufklärung der Struktur von Molekülen mit einer Auflösung bis zur atomaren Ebene. Bisher ist sie jedoch blind für die direkte Unterscheidung der Chiralität. Konventionelle MR-Detektoren sind auf die Erzeugung sowie Detektion magnetischer Felder optimiert. Elektrische Felder spielen jedoch eine notwendige Rolle in der Chiralitätsdetektion. Das zeigt sich in der Tatsache, dass die Terme im MR Hamiltonianoperator unvollständig und damit in Summe unter Parität gerade sind. Lediglich indirekte Methoden zur Chiralitätsdifferenzierung wurden bisher in der MR implementiert. Dadurch ist die MR für die Stereochemie nur bedingt geeignet um chirale Moleküle zu unterscheiden. Die meisten hergestellten Arzneimittel sind chiral und damit wird insbesondere in der pharmazeutischen Industrie das grundlegende Potential der MR nicht genutzt. Chirale Moleküle sind in den biologischen Wissenschaften von großer Bedeutung, da ein Enantiomer je nach der Händigkeit eines chiralen Moleküls entweder eine therapeutische oder toxische Wirkung auf den Körper haben kann. Ein prominentes Beispiel ist der Contergan-Skandal, bei dem ein Enantiomer die morgendliche Übelkeit bei Schwangeren lindern konnte, während das andere Enantiomer Geburtsfehler bei Neugeborenen verursachte.

Um die MR für die direkte chirale Unterscheidung nutzen zu können, besteht eine Lösung darin, den Hamiltonoperator so zu erweitern, dass er einen Term ungerader Parität enthält. Wie von A.D. Buckingham vorhergesagt, sind in einem chiralen Molekül der elektrische und der magnetische Dipol mit einem ungeraden Paritätstensor aneinander gekoppelt. Daher kann durch die Verwendung eines Konjugats aus magnetischen (B_1) und elektrischen (E_2) Feldern in der Präsenz

starker statischer Magnetfelder (B_0) ein ungerader Paritätsterm in den MR Hamiltonianoperator eingeführt werden, der für jedes Enantiomerenpaar einen entgegengesetztes Vorzeichen hat.

In dieser Dissertation wird die Theorie diskutiert, die die Einführung des ungeraden Paritätsterms in den Hamiltonianoperator ermöglicht. Da das nachweisbare chirale Signal im Vergleich zu einem herkömmlichen MR-Signal schwach ist, werden verschiedene Techniken vorgestellt, um es auf der Grundlage der Entwicklung der Spinzustände zu verstärken. Als diese Arbeit geschrieben wurde, gab es noch keine Berichte über Messungen eines direkten chiralen Signals mittels der MR. Dies ist darauf zurückzuführen, dass noch keine funktionsfähigen Detektoren für diesen Zweck entwickelt worden waren. Daher werden verschiedene Resonatordesigns studiert und die Entwicklung sowie schließlich der Weg, der zum erfolgreichen Detektorentwurf führt im Detail diskutiert.

Die erzielten theoretischen sowie experimentellen Ergebnisse werden vorgestellt und analysiert. Abschließend werden in einem Ausblick das Potenzial des entwickelten Detektors sowie weitere zu untersuchende Aspekte diskutiert.

Abstract

Nuclear magnetic resonance (NMR) spectroscopy is a powerful spectroscopic tool used to elucidate the structure of molecules with resolution down to the atomic level. However, it is normally blind to direct chirality distinction. The reason is that all terms in the NMR Hamiltonian are even under parity. Therefore, for stereo-chemistry-related measurements, NMR does not directly provide information about the difference between the enantiomer pairs.

This limitation creates a void for NMR, especially in the pharmacological industry, as most drugs manufactured are chiral. Chiral molecules find great importance in the life sciences, as depending on the handedness of a chiral molecule, its enantiomer can have either therapeutic or toxic effects on the host body. The most infamous example is the thalidomide (or Contergan) scandal, where one enantiomer remedied morning sickness in pregnant women, and its other counterpart caused birth defects in newborns.

To use NMR for direct chiral distinction, the solution is to alter the Hamiltonian to include an odd parity term. A.D. Buckingham predicted that, in a chiral molecule, the electric and magnetic dipole are coupled to each other with an odd parity tensor. Therefore, by using a conjugate of radio-frequency magnetic (B_1) and electric (E_2) fields in the presence of a strong static magnetic field (B_0), this odd parity tensor mentioned as chirality tensor is included in the NMR Hamiltonian. This tensor has an opposite sense for either enantiomer, making an enantiomeric distinction possible.

This dissertation begins with the theory of NMR and the introduction of the chiral tensor in the Hamiltonian. Since the detectable chiral signal is comparatively weaker than a conventional NMR signal, various techniques to enhance it using

the evolution of the magnetisations are explored. When this dissertation was written, no measurements using a direct method with NMR were reported. This can be attributed to the fact that no suitable detectors had been invented for this purpose. Therefore, various attempted designs of resonators, their evolution, and finally, the path that led to a successful detector design are explained.
In the end, the dissertation presents the results obtained using this detector, and concludes with a future outlook and further improvement for the technique developed.

Contents

Nomenclature

Acronym

2-D	two dimensional
3-D	three dimensional
BCH	Baker-Campbell-Hausdorf
CISS	chiral induced spin selectivity
CDA	chiral derivatizing agent
CSA	chiral solvating agent
DMSO	Dimethylsulfoxid
ee	enantiomeric excess
EM	electromagnetic
FID	free induction decay
FWHM	full width half maxima
NMR	nucleur magnetic resonance
NSAIM	non-steroidal anti-inflammatory medicine
PCB	printed circuit board
ppb	parts per billion

ppm parts per million

RF radio-frequency

SNR signal-to-noise ratio

Constants

π $3.14159\ldots$

$\hbar$ $1.055 \times 10^{-34}\,\mathrm{J\,s}$

k_{B} $1.381 \times 10^{-23}\,\mathrm{JK}^{-1}$

ε_0 $8.854 \times 10^{-12}\,\mathrm{F\,m}^{-1}$

μ_0 $1.256 \times 10^{-6}\,\mathrm{kgms}^{-2}\mathrm{A}^{-2}$

c $3 \times 10^{8}\,\mathrm{m\,s}^{-1}$

Symbols

ω angular frequency

ω_0 angular Larmor frequency

ω_{rf} angular RF frequency

δ chemical shift

σ_c chirality coupling constant

$\hat{\rho}$ density operator

γ_{r} gyromagnetic ration

$\hat{H}$ Hamiltonian operator

B_1 RF magnetic field

E_2	RF electric field
$\hat{I}$	spin angular momentum operator
$\hat{\mu}$	spin magnetic moment
m_I	spin projection
I	spin quantum number
B_0	static magnetic field
τ	torque
$\hat{U}$	unitary operator

1 Introduction

This dissertation deals with the method of development for direct chirality distinction in nuclear magnetic resonance (NMR). As this constitutes the first-ever successful attempt reported, the purpose of this dissertation was to clarify the path from theoretical prediction to results obtained. Therefore, to start the explanation we first need to address the question: *"why NMR spectroscopy?"*

NMR is a widely used structure elucidation technique with resolution up to the atomic level of the molecule. Since its first introduction [1], various techniques have been developed to broaden its application. Most of these techniques for example HSQC [2], WATERGATE [3,4], COSY [5], waterLOGSY [6] have now become standard routines in the measurement.

Though, the concept of chirality distinction in NMR, is not something new; however, they rely on indirect methods. Some of them are using chiral alignment medium [7, 8], chiral derivatization agent [9, 10], chiral solvating agents [9–12]. Unfortunately, none of them can be regarded as a direct distinction method.

The absence of a direct distinction method can be regarded as a fact that the Zeeman effect, the phenomenon responsible for NMR signal, is an even parity tensor [13]. Therefore, regardless of the handedness of the enantiomer under observation the NMR signal intensity and the frequency shift on a frequency scale will be the same for a pair of enantiomers; hence, it can righteously be stated that NMR is blind to chirality.

This dissertation takes the brevity to introduce an odd parity tensor to the NMR Hamiltonian followed from the derivation presented by [13, 14]. This allows the distinction of the enantiomer pair in NMR directly; hence, making it sensitive to

the handedness of chiral molecules. To understand, why the odd parity tensor is important for chiral molecules distinction, we need to properly define chirality.

1.1 Chirality

Chirality is a property of asymmetry of an object with respect to its mirror transformation. The word chiral derives from an ancient Greek word $\chi\varepsilon\iota\rho$ (cheir), meaning hand, which perfectly defines the phenomena. The left hand is a mirror image of the right hand, which cannot be superimposed on each other, or it can never coincide with the other one.
Lord Kelvin, during his lecture in 1893, at the Oxford University Junior Science Club, stated that "**I call any geometrical figure, or group of points, 'chiral', and say that it has chirality if its image in a plane mirror, ideally realized, cannot be brought to coincide with itself.**" [15].
To understand it in a broader context, chirality can have different meanings depending on the context and field in which an object is defined as chiral. In the following text use of the word chirality in different fields is explained briefly.

1.1.1 Chirality in geometrical shapes

To explain chiral geometries, we use a three-dimensional (3-D) Euclidean space, such that any point P_i can be defined by a set of coordinates $\{x_i, y_i, z_i\}$. Therefore, to define the corner points of geometry we use a set of points P_i, such that $T = \{P_1, P_2, P_3...\}$, where $P_i \neq P_j$ for $i \neq j$. If we now define two functions R_θ, and M, where R_θ defines the rotation of the T by an angle θ along an axis, and M defines the mirror transformation along a plane parallel to the rotation axis. Then a geometry is said to be chiral if $T \neq \mathrm{M}[\mathrm{R}_\theta[T]]$, where $\forall\theta \in \{0, 2\pi\}$
For a two-dimensional (2-D) Euclidean space a point P_i, defined by a set of coordinates $\{x_i, y_i\}$, forming the corner of the geometry T=$\{\mathrm{P}_1,\mathrm{P}_2,\mathrm{P}_3...\}$, will be chiral if and only if there doesn't exist a symmetry axis. E.g. an equilateral and an isosceles triangle are achiral whereas all other triangles are chiral in 2-D space.

1.1.2 Chirality in physics

Chirality in physics can be explained via the propagation of a circularly polarised electromagnetic (EM) wave. An EM-wave consists of an electric and magnetic field oscillating at a certain frequency. They will be always orthogonal to each other, as well as to the direction of propagation. If another EM-wave oscillating at the same frequency is superimposed on the original wave, it produces a circular polarisation, if the two waves have the same magnitude, and have a phase shift of $\pi/2$ between them. Depending on the direction of the phase shift between the two waves, it can either produce a clockwise (right-handed) or an anticlockwise (left-handed) polarised wave. These two polarisation are chiral, i.e., they are mirror images of each other and are invariant in space.
The handedness of the light wave plays an important role in chiral distinction, where one of the handedness can completely pass through an enantiomer, and the other one will be absorbed. This phenomenon, called optical activity, laid the basics of chiral distinction techniques in optics [16].

1.1.3 Chirality in chemistry

In Chemistry, a molecule is said to be chiral if its mirror image cannot be superimposed on it. The two pairs are called enantiomers and have different physical and chemical behaviour due to their structural orientation.
We observe chiral molecules in our daily lives and can be quite fascinating. For example, the concentration of enantiomer of carvone defines the smell difference between the spearmints and caraway. In spearmints, the enantiomeric excess of (R)-carvone is responsible for the smell whereas, in caraway, the enantiomeric excess of (S)-carvone is responsible for different smells.
The difference in the smell can be attributed to the olfactory receptors in our nose, which may be chiral in nature as well [17–19]. The molecules that are living organisms' building blocks, such as carbohydrates, amino acids, and nucleic acids, are chiral. Therefore, a living organism consists of a large number of chiral compounds [20].

The difference in geometrical arrangement makes chiral molecules highly selective, where a specific enantiomer can interact with the host molecules. This allows chiral molecules to find great importance in the field of pharmacology.
This can be supported by the fact that it is estimated that more than half of the drugs manufactured are synthesized from chiral molecules [21, 22]. Since one of the stereoisomers called the active enantiomer may bind to the receptor site, while the other one remains inactive. As each enantiomer can be metabolized differently, it can either be therapeutic, ineffective or in the worst case toxic. If one looks at history, chirality led to an infamous scandal involving thalidomide, where the active enantiomer was used to cure morning sickness, anxiety, trouble sleeping and tensions, but its counterpart caused birth defects [23, 24]. Another example is ethambutol, where one of the enantiomers is used in the treatment of tuberculosis while its counterpart can cause blindness [25].
Therefore, it becomes crucial to distinct chiral molecules (or drugs), to make them safe for public consumption or to have the beneficial properties of one of the enantiomers. There exist several techniques for chiral distinction some of which are through circular dichroism [26–28], Raman optical activity [28–31], gas chromatography [32] etc. Though there also exists chiral distinction methods using NMR, they involve alteration of the sample under test. At the moment, when this dissertation was written, there were no direct methods to distinguish chiral molecules.

1.2 Chiral distinction in NMR

The general methodology for distinguishing chiral compounds in NMR involves an auxiliary compound called chiral reagents. They react differently with the enantiomer pairs. This causes signal suppression or change in signal intensity from the reaction site. Using this, the enantiomer type can be determined. Depending on the chemical bonds formed by the auxiliary compounds the technique is further divided into two parts as described below [33].

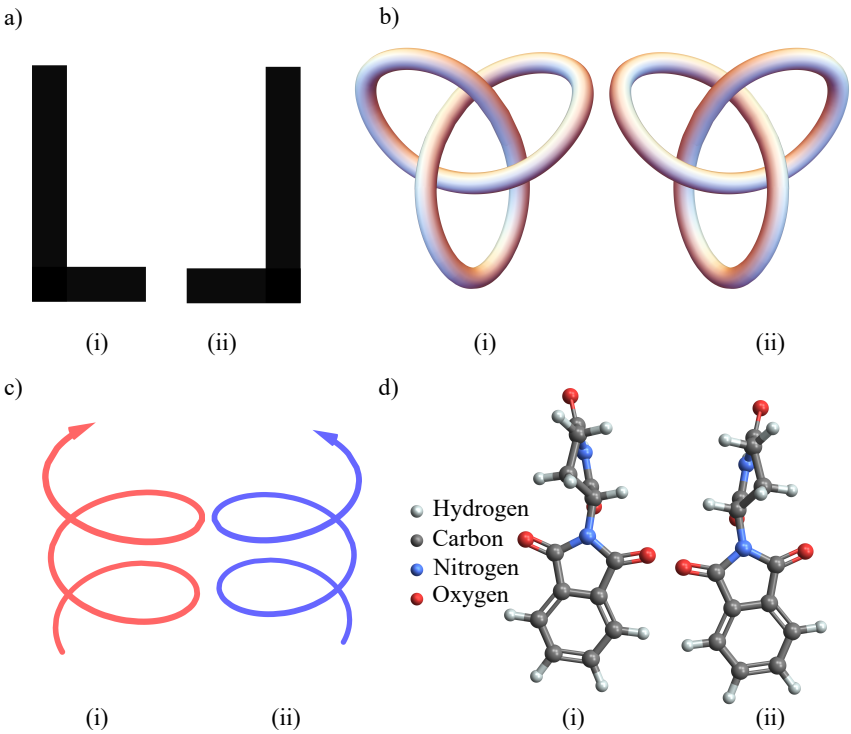

Figure 1.1: Example of chirality in different fields of study. (i) and (ii) in each of the subfigures (a-d) represent the mirror image. As can be seen from the figures no two chiral pairs can be superimposed on each other. (a) A 2-D chiral geometry of an 'L' alphabet of the English language. (b) A 3-D chiral geometry example of Trefoil Knot. (c) Left-handed (i) and right-handed (ii) circularly polarised light propagating in vertical direction. (d) An example of an enantiomer pair of thalidomide. (i) (R)-thalidomide is a toxic molecule which can cause birth defects. (ii) (S)-thalidomide was used as a drug for morning sicknesses.

1.2.1 Chiral derivatising agents (CDA)

CDA results in the formation of a covalent bond between the chiral molecule and the molecule used for differentiation. This method has two drawbacks, the kinetic of the reaction for both the enantiomer needs to be maintained at the same rate, and to avoid the racemisation of the enantiopure compounds [33].

1.2.2 Chiral solvating agents (CSA)

CSA involves the formation of non-covalent bonds between the chiral and the probing molecule. CSA is usually used to determine the enantiopurity [33]. One of the drawbacks of this method is that not all chiral compounds may react with the molecule used for testing. Therefore, in some cases, selector molecules need to be synthesised.

1.3 Motivation

Over the years, improvements to the NMR systems and the introduction of several techniques such as multi-dimensional spectroscopy [34], diffusion measurements [35], Nuclear Overhauser spectroscopy technique [36] etc. have broadened the field of application for NMR compared to other spectroscopic techniques. However, there is still more to be discovered and invented.
As chirality has never been distinguished with NMR using the instrumentation method, it motivated us to discover ways and to invent the equipment which would have enabled us to achieve this feat.
In this dissertation, the focus is on the development of a method which combines electric and magnetic fields. Doing so helped to add an odd parity term in the NMR Hamiltonian.
The reason for applying an electric field is because of a property inherent to the chiral molecules, optical activity. It was due to the optical activity of chiral molecules, that enabled them to distinguish the enantiomer pairs.
The reason for optical activity in chiral molecules is:
Electromagnetic waves consist of an electric field and a magnetic field. When they propagate through a molecule, the interaction of light with the molecules induces an electric and magnetic polarisation given as [37]

$$\vec{P} = N\alpha\vec{E} - N\beta\frac{\partial\vec{B}}{\partial t} \tag{1.1}$$

where, $\vec{P}$ is the strength of electric field polarisation, α is the electric polarisability of a molecule, N is the number of molecules per volume, and β is the electric dipole moment induced by the magnetic field. For an achiral molecule, it is zero due to it being symmetric. The resultant of electric polarisation due to electric field and magnetic field causes a linearly polarised light to rotate in an optically active medium [37].

Similarly, it was shown by [13] and [14] that, a rotating nuclear magnetic moment induces a rotating electric dipole which is orthogonal to the magnetic moment and static magnetic field. The direction of the electric dipole generated is opposite for different enantiomer pairs.

Going by the reciprocity principle of Maxwell's equation, the converse will also be true that, in an asymmetric molecule, a rotating E-field will induce a rotating magnetic dipole which will be opposite in sense for the enantiomers.

This was the motivation to establish a spectroscopic technique which would help cure NMR blindness towards the chiral molecules.

1.4 Overview of the dissertation

- In chapter 2, we establish the theory for the case when an electric field is applied in an NMR environment. From the Hamiltonian, we derive the evolution of the spin and discuss various conditions which can be useful for chiral detection.
- In chapter 3, we demonstrate the present state of the art and based on various experimental conditions discussed in chapter 2, the design of chiral detectors is discussed in detail.
- In chapter 4 we show the experimental setup and characterise the NMR properties of the detector.
- In chapter 5 we conclude the thesis and give an overview of future aspects of chirality measurement.

2 Introduction to nuclear magnetic resonance spectroscopy and the odd-parity chiral tensor

In this chapter, the fundamental theory behind the NMR based on a quantum mechanical approach is explained. Most of the equations and explanations are taken from [38] and [39]. This chapter aims to introduce the chirality-dependent term in the NMR Hamiltonian. The chiral-dependent tensor defines the coupling between the electric and magnetic dipole around the chiral centre of the molecule. With the introduction of the odd-parity term into an NMR Hamiltonian of a spin-1/2 system, the evolution of the net magnetisation under the presence of an radiofrequency (RF) electric field is derived. From this, different scenarios and techniques are presented which enable the detection of chiral signals.

2.1 The basics concepts of nuclear magnetic resonance

2.1.1 Quantum mechanical description of NMR

To explain NMR, we will first have to understand the spins in an atom. Atoms consist of electrons orbiting around the nucleus, which contain neutrons and protons (or nucleons). The electrons, neutrons and protons have spin angular momentum, an intrinsic property. Each atom including its isotopes has a certain number of electrons, neutrons and protons. The number of neutrons and protons defines the net nuclear spin, which defines the spin number of the atom

A particle with a spin can be denoted by the quantum number [38]

$$S_n = \tfrac{1}{2}. \tag{2.1}$$

For a fermion (electron, proton and neutron), the spins are half-integer. Therefore, for a system with n number of protons and neutrons, each can be a source of spin angular momentum with nuclear spin quantum number S_1,S_2,$\cdots$,S_n. The nuclear spin number that such a system can have is given as

$$I = |S_1 + S_2 + \cdots + S_n|, \tag{2.2}$$

$$|S_1 + S_2 + \cdots + S_n| - 1, \cdots |S_1 - S_2 - \cdots - S_n|, \tag{2.3}$$

where I usually denotes the nuclear spin quantum number [38]. An atom with one proton will have a nuclear spin quantum number $I = 1/2$, and an atom with one proton and one neutron will have nuclear spin quantum numbers $I = 1$ and $I = 0$. The total magnitude of the angular momentum for a spin system I is given as

$$\left|\vec{I}\right| = \hbar\sqrt{(I)(I+1)}, \tag{2.4}$$

where $\hbar$ is Plank's constant [38].

To describe the spins in more detail, another quantum number m_I is used, which defines the projection of a spin. As the description suggests, m_I is called the spin projection quantum number.

If a spin system is placed in a static magnetic field (B_0), where the field is along the z-direction (the convention used in the dissertation unless specified), then the projection is given by m_I. The two quantum numbers, m_I and I, are related to each other such that m_I can only have $2I+1$ values, i.e., between $-I$ to $+I$. Therefore, nuclear spins have $2I+1$ energy degeneracy [38].

For example, a spin system with $I = 1/2$ can have two energy levels denoted by $m_I = [-1/2, 1/2]$. A spin system with $I = 1$ can have three energy levels, $m_I = [-1, 0, 1]$ [38].

The angular momentum of the spins parallel to the z-direction is given as [38]

$$\hat{I}_z = m_I \hbar. \tag{2.5}$$

The table 2.1 represents the different scenarios depending on the number of nucleons.

Table 2.1: Nuclear spin and spin direction quantum numbers (for the first spin system) based on the number of nucleons and an example of an isotope [38].

# Neutrons	# Protons	Ground-state (I)	Projection directions (m_I)	Isotope
Odd	Odd	1	-1, 0, 1	^{2}H
Even	Even	0	0	^{16}O
Even	Odd	$1/2$	$-1/2$, $1/2$	^{15}N
Zero	Even	$1/2$	$-1/2$,$1/2$	^{1}H

Therefore, all the nuclei where $I \neq 0$ have an NMR signal for example ^{1}H, ^{2}H ^{13}C, ^{14}N, ^{15}N, etc [38].

Nuclei with $I = 1/2$ are called spin-1/2 systems. Further discussions and the derivation of the Hamiltonian are based on a spin-1/2 system.

As spins have angular momentum ($\hat{I}$), and a magnetic moment ($\hat{\mu}$), they are related to each other as

$$\hat{\mu} = \gamma_r \hat{I}, \tag{2.6}$$

where γ_r is the gyromagnetic ratio [38]. Depending on the direction of $\hat{I}$ and $\hat{\mu}$, γ_r can either have a positive or a negative magnitude. If they are both parallel to each other, then γ_r is positive, else negative [38].

When the spins are placed in B_0, they experience a torque induced on them. This torque is defined as [38]

$$\vec{\tau} = \hat{\mu} \times \vec{B_0}. \tag{2.7}$$

The torque causes the spin to precess around the B_0 direction. The frequency with which the spins precess is called the Larmor frequency. The angular Larmor frequency (ω_0) depends directly on the magnitude of the B_0. The ω_0 and the B_0 are related as [38, 39]

$$\omega_0 = \gamma_r \vec{B}_0. \tag{2.8}$$

Depending on the direction of the spin, i.e., $m_I = \pm 1/2$, the spins can either attain energy [38, 39]

$$E_1 = -\tfrac{1}{2}\hbar\omega_0, \tag{2.9}$$

or

$$E_2 = \tfrac{1}{2}\hbar\omega_0. \tag{2.10}$$

Therefore, this creates a degeneracy for a spin-1/2 system and splits the energy into two sub-levels, with a total energy difference of

$$\Delta E = \hbar\omega_0, \tag{2.11}$$

which is the Zeeman splitting [38, 39].
When such a system is irradiated with an RF-wave, with an angular frequency of ω_0, the spins are excited from the ground level to a higher energy level followed by their relaxation. During the relaxation process, they release photons corresponding to the energy of ω_0. The acquisition of the photons is then converted into a voltage signal, which is the NMR signal [38, 39]. The γ_r and ω_0 in a 11.74 T static magnetic field is summarised for a few NMR relevant isotopes in table 2.2.

2.1.2 Wave function of the ensemble of spins and the observable in the NMR

As defined above, NMR is a quantum effect. Since the distribution of the spins in the energy level can be determined statistically, one can with assumptions deduce the the classical equations that govern the spins dynamic. Since it is difficult to

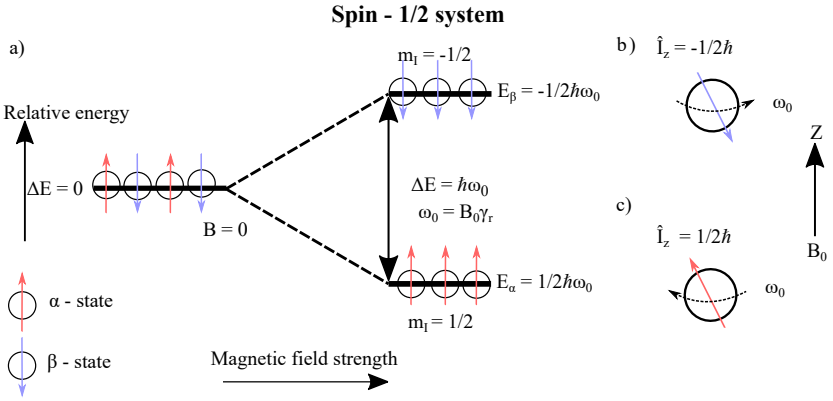

Figure 2.1: (a) Represents the Zeeman splitting effect for a $I = 1/2$ system. In the absence of a magnetic field, there is no degeneracy. After applying a magnetic field of strength B_0 a two-level degeneracy is created, where the ground-state (α), corresponds to the spin aligned along the direction of B_0 and higher energy state (β) corresponds to anti-parallel aligned spins. The difference between the two energy levels can be equated by the angular frequency ω_0, where ω_0 is the product of B_0 and gyromagnetic ratio γ_r. (b) & (c) Shows the spin nutating around the z-axis by ω_0, where $\hat{I}_z$ is the corresponding angular momentum operator.

Table 2.2: The value of γ_r and corresponding ω_0 for different isotopes when placed in a B_0 of 11.74 T [38, 39].

Isotope	γ_r rad µs^{-1} T^{-1}	$\omega_0/2\pi$ MHz
^{1}H	267.522	500
^{19}F	251.815	470.5
^{13}C	67.283	125.75
^{15}N	-27.116	50.67

predict the behaviour of each spin, the calculation is made easier by assuming that the ensemble of spins has a net effect. However, to do so it is important to find a function which describes the ensemble of spins. For the explanation, it is assumed that we have an isolated and uncoupled spin-1/2 system.

If there are N spins in a system, each of them can be represented by their own Hamiltonian. Averaging over each of their behaviour will give the macroscopic behaviour. Since a wave function can be represented as a summation of other wave functions, it is possible to represent the entire spin system from individual spins. The wave function for N spins is

$$|\Psi\rangle = \sum_{n=1}^{N} c_n |\Psi_n\rangle , \tag{2.12}$$

which is the superposition of N states [38, 39]. c_n, which is a complex number, is the superposition coefficient of n^{th} state [38, 39]. Since in a spin-1/2 system, placed under the B_0, there exist only two eigenstates. The wave function of the system is then expressed as a superposition of the two energy states such that [38, 39]

$$|\Psi\rangle = c_\alpha |\alpha\rangle + c_\beta |\beta\rangle , \tag{2.13}$$

where $|\alpha\rangle$ and $|\beta\rangle$ are given as [38, 39]

$$|\alpha\rangle = \left|\tfrac{1}{2}, +\tfrac{1}{2}\right\rangle , \tag{2.14}$$

$$|\beta\rangle = \left|\tfrac{1}{2}, -\tfrac{1}{2}\right\rangle . \tag{2.15}$$

Since $|\alpha\rangle$ and $|\beta\rangle$ are orthonormal basis sets, therefore, the probability of finding a spin in either of the state will be given as [38, 39]

$$\langle\Psi|\Psi\rangle = c_\alpha c_\alpha^* + c_\beta c_\beta^*, \tag{2.16}$$

where, if the term is normalised then [38, 39]

$$c_\alpha c_\alpha^* + c_\beta c_\beta^* = 1. \tag{2.17}$$

This means that the probability of finding spins in either one of the states is unity; whereas, the probability of the spins existing in either of the states is the magnitude of the complex number c_α and c_β.

To calculate the evolution of the spins over time, the Schrödinger's equation is used. Using the wave function it is written as

$$i\hbar \frac{d|\Psi\rangle}{dt} = \hat{H}|\Psi\rangle, \tag{2.18}$$

where $\hat{H}$ is the Hamiltonian of the system [40].
The calculated wave function of the system is then used to define a density operator. The density operator describes the quantum mechanical state of the entire system. As assumed earlier if we have N number of spins, by taking the ensemble average of the wave function we can calculate the density operator, which is given as [38, 39]

$$\hat{\rho} = \overline{|\Psi\rangle\langle\Psi|}. \tag{2.19}$$

On solving the equation we get

$$\hat{\rho} = \overline{c_\alpha c_\alpha^*} + \overline{c_\beta c_\beta^*} + \overline{c_\alpha c_\beta^*} + \overline{c_\beta c_\alpha^*}, \tag{2.20}$$

where the first two terms define the population of the state and the last two terms define the coherence between the energy states [38, 39].
The density operator, when used in the Schrödinger's equation, is given as

$$i\hbar \frac{d|\hat{\rho}\rangle}{dt} = \hat{H}|\hat{\rho}\rangle. \tag{2.21}$$

On solving the equation we get the time evolution of the density operator as [39]

$$\frac{\partial \hat{\rho}}{\partial t} = -\frac{i}{\hbar}\left[\hat{H}, \hat{\rho}\right], \tag{2.22}$$

which is the Liouville-von Neumann equation, where the solution of the equation is given as

$$\hat{\rho}(t) = \exp\left(-i\hat{H}t\right)\hat{\rho}(0)\exp\left(i\hat{H}t\right). \tag{2.23}$$

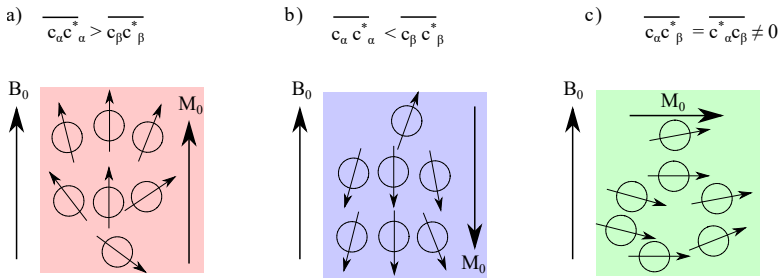

Figure 2.2: Representation of net magnetisation M_0 resulting from the net spin polarisation, where $\overline{c_\alpha c_\alpha^*}$ and $\overline{c_\beta c_\beta^*}$ are the population of α and β states. $\overline{c_\alpha c_\beta^*}$ and $\overline{c_\alpha^* c_\beta}$ are the coherence between α and β states [38]. (a) When the population of spins in α state is more than in β state. (b) Shows the condition to (a), where the spins are aligned anti-parallel to B_0. (c) When an RF-pulse is applied, the spins flip in the transverse plane. If there is a net magnetisation the spins are in coherence.

$\hat{\rho}(0)$ is the initial condition of the density operator, and $\hat{\rho}(t)$ is the state of the density operator after a time t on being driven by a time independent Hamiltonian $\hat{H}$ [39,41]. Once the state of the density operator is known, taking its trace with an observable operator gives the measurable observable signal of the entire system. Therefore, the average of all the spins ensemble for an observable state X is given as [38, 39]

$$\langle X \rangle = \mathrm{Tr}\left\{\hat{\rho}\hat{X}\right\}. \tag{2.24}$$

Since in the case of NMR, the observable operators are the spin operators, in the next section we will define the spin operators for a spin-1/2 system.

2.1.3 Spin projection operators

Since we now know that for a spin-1/2 system placed in a B_0, there exist two possible orientations of the spins given by $m_I = \pm 1/2$. Therefore, there exist two

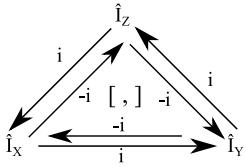

Figure 2.3: Cyclic property of the commutator operator, where the commutation of two angular momentum operators results in the imaginary number of the third. If the order of commutation is reversed, a negative sign represents it [39].

states, which can be represented by α representing $|1/2,-1/2\rangle$, and β representing $|1/2,+1/2\rangle$. We can write them in matrix form as [38, 39]

$$|\alpha\rangle = \begin{pmatrix} 1 \\ 0 \end{pmatrix}, \tag{2.25}$$

$$|\beta\rangle = \begin{pmatrix} 0 \\ 1 \end{pmatrix}. \tag{2.26}$$

If we assume B_0 to be along the z-direction, then the angular momentum operator for the two spin states in the z-direction is

$$\hat{I}_z |I, m_I\rangle = m_I \hbar |I, m_I\rangle . \tag{2.27}$$

The I and m_I quantum numbers are unaffected, and m_I defines the direction of the angular momentum [38, 39].
Similarly, the $\hat{I}_x$ and $\hat{I}_y$ angular momentum operators can be defined in the x and y-directions, respectively [38, 39]. One important property to note here is that these operators are cyclic [39] as shown in fig. 2.3 and table 2.3. This is an important property, which is used extensively for further derivations.

Table 2.3: Commutator operation on the spin angular momentum is cyclic. The results from the table are used in the further derivation to determine the spin evolution [39].

Commutator	Result
$\left[\hat{I}_x, \hat{I}_y\right]$	$\mathrm{i}\hat{I}_z$
$\left[\hat{I}_y, \hat{I}_z\right]$	$\mathrm{i}\hat{I}_x$
$\left[\hat{I}_z, \hat{I}_x\right]$	$\mathrm{i}\hat{I}_y$

From eq. (2.25) and (2.26), $\hat{I}_z$ for the $I = \frac{1}{2}$ system in a static magnetic field in the matrix form is [38, 39]

$$\hat{I}_z = \begin{pmatrix} \langle\alpha|I_z|\alpha\rangle & \langle\alpha|I_z|\beta\rangle \\ \langle\beta|I_z|\alpha\rangle & \langle\beta|I_z|\beta\rangle \end{pmatrix}. \tag{2.28}$$

As the terms β, and α are orthogonal, $\langle\alpha|I_z|\beta\rangle$ and $\langle\beta|I_z|\alpha\rangle$ reduce to zero and using eq. (2.27) we get [38, 39]

$$\hat{I}_z = \frac{\hbar}{2}\begin{pmatrix} 1 & 0 \\ 0 & -1 \end{pmatrix}. \tag{2.29}$$

Now to find the $\hat{I}_x$ and $\hat{I}_y$, the ladder-up ($\hat{I}^+$) and ladder-down ($\hat{I}^-$) operators are used, which are related as [38, 39]

$$\hat{I}_x = \frac{\hat{I}^+ + \hat{I}^-}{2}, \tag{2.30}$$

$$\hat{I}_y = \frac{\hat{I}^+ - \hat{I}^-}{2\mathrm{i}}, \tag{2.31}$$

where [38, 39],

$$\hat{I}^+|I, m_I\rangle = \hbar\sqrt{(I - m_I)(I + m_I + 1)}\,|I, m_I + 1\rangle, \tag{2.32}$$

$$\hat{I}^-|I, m_I\rangle = \hbar\sqrt{(I + m_I)(I - m_I + 1)}\,|I, m_I - 1\rangle. \tag{2.33}$$

Since, $|\alpha\rangle$ and $|\beta\rangle$ are the eigenstates, therefore, the $\hat{I}_+$, and $\hat{I}_-$ when operated on the eigenstates, are given as [38, 39]

$$\hat{I}^+ |\alpha\rangle = 0, \tag{2.34}$$

$$\hat{I}^+ |\beta\rangle = \hbar |\alpha\rangle, \tag{2.35}$$

$$\hat{I}^- |\alpha\rangle = \hbar |\beta\rangle, \tag{2.36}$$

$$\hat{I}^- |\beta\rangle = 0. \tag{2.37}$$

The solution from these equations is then used in the matrix representation of $\hat{I}^+$ and $\hat{I}^-$, where [38, 39]

$$\hat{I}^+ = \begin{pmatrix} \langle\alpha| I^+ |\alpha\rangle & \langle\alpha| I^+ |\beta\rangle \\ \langle\beta| I^+ |\alpha\rangle & \langle\beta| I^+ |\beta\rangle \end{pmatrix}, \tag{2.38}$$

and

$$\hat{I}^- = \begin{pmatrix} \langle\alpha| I^- |\alpha\rangle & \langle\alpha| I^- |\beta\rangle \\ \langle\beta| I^- |\alpha\rangle & \langle\beta| I^- |\beta\rangle \end{pmatrix}. \tag{2.39}$$

Simplifying eq. (2.38) the result is,

$$\hat{I}^+ = \hbar \begin{pmatrix} 0 & 1 \\ 0 & 0 \end{pmatrix}, \tag{2.40}$$

and for eq. (2.39) the solution is

$$\hat{I}^- = \hbar \begin{pmatrix} 0 & 0 \\ 1 & 0 \end{pmatrix}. \tag{2.41}$$

As we have the solution of the $\hat{I}^+$ and $\hat{I}^-$, we can find the $\hat{I}_x$ and $\hat{I}_y$ operators by solving eq. (2.30) and (2.31) respectively. In the matrix form, the solution is [38, 39]

$$\hat{I}_x = \frac{\hbar}{2}\begin{pmatrix} 0 & 1 \\ 1 & 0 \end{pmatrix}, \tag{2.42}$$

$$\hat{I}_y = \frac{\hbar \mathrm{i}}{2}\begin{pmatrix} 0 & -1 \\ 1 & 0 \end{pmatrix}. \tag{2.43}$$

With the spin operators $\hat{I}_x$, $\hat{I}_y$ and $\hat{I}_z$ found, we can now calculate the evolution of the spins in the Liouville-von Neumann space.

2.1.4 Transformation of the Hamiltonian in the rotating frame and solution of the Liouville-von Neumann equation

To find the solution for the Liouville-von Neumann equation as shown in eq. (2.22) we need to first convert the NMR Hamiltonian from the laboratory frame of reference to the rotating frame of reference. The perturbed Hamiltonian for a spin-1/2 isolated system in the laboratory frame of reference is given as [38, 39]

$$\hat{H}_{\mathrm{Lab}}(t) = \omega_0 \hat{I}_z + \omega_{B_1} \cos(\omega_{\mathrm{rf}} t + \phi)\hat{I}_x + \omega_{B_1} \sin(\omega_{\mathrm{rf}} t + \phi)\hat{I}_y, \tag{2.44}$$

where the first term of the equation represents the Zeeman effect such that [38,39]

$$\omega_0 = \gamma_r \vec{B}_0. \tag{2.45}$$

The second and third terms represent the RF magnetic field perturbation such that

$$\omega_{B_1} = \gamma_r \vec{B}_1/2, \tag{2.46}$$

where $\vec{B}_1$ is the RF magnetic field applied along the x-y plane [38, 39]. The $\vec{B}_1$ magnetic field is assumed to be circularly polarised such that there is a constant

phase difference of $\pi/2$ between the x and y-component of the magnetic field vector.

To transform the Hamiltonian to a rotating frame of reference, we assume a unitary operator $\hat{U}$ such that [38, 39]

$$\hat{\rho} = \hat{U}\hat{\rho}\hat{U}^{-1}. \tag{2.47}$$

Therefore, if we solve for $\hat{\rho}$ from,

$$\frac{\partial\hat{\rho}}{\partial t} = \frac{\partial(\hat{U}\hat{\rho}\hat{U}^{-1})}{\partial t}, \tag{2.48}$$

the expansion is

$$\frac{\partial\hat{\rho}}{\partial t} = \frac{\partial\hat{U}}{\partial t}\hat{\rho}\hat{U}^{-1} + \hat{U}\frac{\partial\hat{\rho}}{\partial t}\hat{U}^{-1} + \hat{U}\hat{\rho}\frac{\partial\hat{U}^{-1}}{\partial t}. \tag{2.49}$$

if we rewrite the second term from eq. (2.22) and do some rearrangement by writing $\hat{U}\hat{U}^{-1}$ in the first and third term, the re-arrangement is

$$\frac{\partial\hat{\rho}}{\partial t} = \frac{\partial\hat{U}}{\partial t}\hat{U}^{-1}\hat{U}\hat{\rho}\hat{U}^{-1} + \hat{U}\mathrm{i}\left[\hat{\rho},\hat{H}_{\mathrm{Lab}}\right]\hat{U}^{-1} + \hat{U}\hat{\rho}\hat{U}^{-1}\hat{U}\frac{\partial\hat{U}^{-1}}{\partial t}, \tag{2.50}$$

by cancelling the unitary operator with its inverse in the first, and third terms of the above equation, and rearranging the terms

$$\frac{\partial\hat{\rho}}{\partial t} = \frac{\partial\hat{U}}{\partial t}\hat{U}^{-1}\hat{\rho} + \hat{\rho}\hat{U}\frac{\partial\hat{U}^{-1}}{\partial t} + \hat{U}\mathrm{i}\left[\hat{\rho},\hat{H}_{\mathrm{Lab}}\right]\hat{U}^{-1}. \tag{2.51}$$

Since $\hat{U}\hat{U}^{-1} = E$, where E is an identity matrix; therefore, the time derivative is

$$\frac{\partial(\hat{U}\hat{U}^{-1})}{\partial t} = 0. \tag{2.52}$$

On solving,

$$\frac{\partial\hat{U}}{\partial t}\hat{U}^{-1} = -\hat{U}\frac{\partial\hat{U}^{-1}}{\partial t}, \tag{2.53}$$

and rewriting eq. (2.51) again,

$$\frac{\partial\hat{\rho}}{\partial t} = (-\hat{\rho}\hat{U}\frac{\partial\hat{U}^{-1}}{\partial t} + \hat{\rho}\hat{U}\frac{\partial\hat{U}^{-1}}{\partial t}) + \hat{U}\mathrm{i}\left[\hat{\rho},\hat{H}_{\mathrm{Lab}}\right]\hat{U}^{-1}. \tag{2.54}$$

The first and second terms in the brackets are the result of a commutator, therefore,

$$\frac{\partial\hat{\rho}}{\partial t} = \left[\hat{\rho},U\frac{\partial\hat{U}^{-1}}{\partial t}\right] + \hat{U}\mathrm{i}\left[\hat{\rho},\hat{H}_{\mathrm{Lab}}\right]\hat{U}^{-1}. \tag{2.55}$$

If we now include $\hat{U}$ and $\hat{U}^{-1}$, inside the commutator, the term $\hat{U}\rho\hat{U}^{-1}$ from eq. (2.47) becomes $\hat{\rho}$, which simplifies the above equation to

$$\frac{\partial\hat{\rho}}{\partial t} = \left[\hat{\rho},\hat{U}\frac{\partial\hat{U}^{-1}}{\partial t}\right] + \mathrm{i}\left[\hat{\rho},\hat{U}\hat{H}_{\mathrm{Lab}}\hat{U}^{-1}\right]. \tag{2.56}$$

By using the commutation properties,

$$\frac{\partial\rho}{\partial t} = \mathrm{i}\left[\rho,-\mathrm{i}\hat{U}\frac{\partial\hat{U}^{-1}}{\partial t} + \hat{U}\hat{H}_{\mathrm{Lab}}U^{-1}\right]. \tag{2.57}$$

if we take the second term to be equal to $\hat{H}_{\mathrm{Rot}}$, then

$$\hat{H}_{\mathrm{Rot}} = -\mathrm{i}\hat{U}\frac{\partial\hat{U}^{-1}}{\partial t} + \hat{U}\hat{H}_{\mathrm{Lab}}\hat{U}^{-1}. \tag{2.58}$$

Here we assumed that $\hat{H}_{\mathrm{Rot}}$ is the Hamiltonian in a rotating frame of reference [39].

$$\frac{\partial\hat{\rho}}{\partial t} = \mathrm{i}\left[\hat{\rho},\hat{H}_{\mathrm{Rot}}\right], \tag{2.59}$$

whose solution is [39, 41],

$$\hat{\rho}(t) = \exp\left(-\mathrm{i}\hat{H}_{\mathrm{Rot}}t\right)\hat{\rho}(0)\exp\left(\mathrm{i}\hat{H}_{\mathrm{Rot}}t\right). \tag{2.60}$$

As $\hat{H}_{\text{Rot}}$ was assumed to be the transformation of $\hat{H}_{\text{Lab}}$ in rotating frame of reference. Therefore, a suitable unitary operator needs to be used which will allow this transformation.

2.1.5 Unitary operator to transform the Hamiltonian from the laboratory to a rotating frame of reference

From the discussions in subsection 2.1.1, we know that the spins precess around the z-axis with ω_0. It is possible to transform the spatial coordinates systems from a laboratory frame of reference to a rotatory frame of reference with a suitable unitary operator. Therefore, the unitary operator is chosen to be close to the ω_0. As the applied RF pulse's frequency is closer to ω_0, we can write

$$\hat{U} = \exp\left(\mathrm{i}\omega_{\text{rf}} t \hat{I}_z\right), \tag{2.61}$$

such that

$$\hat{U}\hat{U}^{-1} = -\exp\left(\mathrm{i}\omega_{\text{rf}} t \hat{I}_z\right)\exp\left(\mathrm{i}\omega_{\text{rf}} t \hat{I}_z\right) = E, \tag{2.62}$$

where ω_{rf} is the angular frequency of the RF pulse applied [39]. This allows us to fix the frame of the spins with respect to the RF field oscillations.
To find the transformed Hamiltonian we use eq. (2.58) and (2.61), where from eq. (2.58) we have

$$\hat{H}_{\text{Rot}} = -\mathrm{i}\hat{U}\frac{\partial \hat{U}^{-1}}{\partial t} + \hat{U}\hat{H}_{\text{Lab}}\hat{U}^{-1}. \tag{2.63}$$

The eq. is split into two parts for the ease of solving it, such that

$$\hat{H}_{\text{Rot}} = A + B, \tag{2.64}$$

where

$$A = -\mathrm{i}\hat{U}\frac{\partial \hat{U}^{-1}}{\partial t}, \tag{2.65}$$

and

$$B = \hat{U}\hat{H}_{\text{Lab}}\hat{U}^{-1}. \tag{2.66}$$

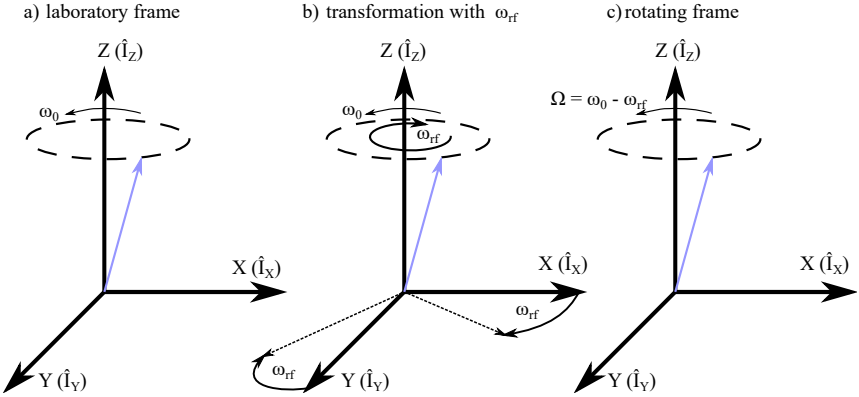

Figure 2.4: (a) When a spin system is placed under an external magnetic field (B_0 along the z-axis), the net magnetisation of the system precesses around the B_0 with the Larmor frequency. (b) If the RF pulse is applied with the angular frequency, ω_{rf}, then for ease of calculation it is possible to transform the laboratory frame of reference to a rotating frame. To do so, the axes are rotated with ω_{rf}. (c) This leads to the transformation in the rotating frame of reference, where the net magnetisation precesses around B_0 axis with an angular frequency of Ω [38, 39].

Eq. (2.65) is straightforward and on solving we get

$$A = -\mathrm{i}\exp\left(\mathrm{i}\omega_{rf}t\right)\hat{I}_z\frac{\partial\left(\exp\left(-\mathrm{i}\omega_{rf}t\hat{I}_z\right)\right.}{\partial t}. \tag{2.67}$$

The derivative of the above eq. is

$$A = -\mathrm{i}\exp\left(\mathrm{i}\omega_{rf}t\hat{I}_z\right)\left(-\mathrm{i}\omega_{rf}\hat{I}_z\right)\exp\left(-\mathrm{i}\omega_{rf}t\hat{I}_z\right). \tag{2.68}$$

The exponential terms cancel each other out and the result for A is

$$A = -\omega_{rf}\hat{I}_z. \tag{2.69}$$

If we now look at eq. (2.66),

$$\begin{aligned} B = \exp\left(\mathrm{i}\,\omega_{\mathrm{rf}} t \hat{I}_z\right)(\omega_0 \hat{I}_z + \omega_{B_1}\cos(\omega_{\mathrm{rf}} t + \phi)\hat{I}_x \\ + \omega_{B_1}\sin(\omega_{\mathrm{rf}} t + \phi)\hat{I}_y)\exp\left(-\mathrm{i}\,\omega_{\mathrm{rf}} t \hat{I}_z\right), \end{aligned} \tag{2.70}$$

where the Hamiltonian is an NMR Hamiltonian mentioned in eq. (2.44)

$$\begin{aligned} B = \exp\left(\mathrm{i}\,\omega_{\mathrm{rf}} t \hat{I}_z\right)(\omega_0 \hat{I}_z)\exp\left(-\mathrm{i}\,\omega_{\mathrm{rf}} t \hat{I}_z\right) \\ + \exp\left(\mathrm{i}\,\omega_{\mathrm{rf}} t \hat{I}_z\right)(\omega_{B_1}\cos(\omega_{\mathrm{rf}} t + \phi)\hat{I}_x \\ + \omega_{B_1}\sin(\omega_{\mathrm{rf}} t + \phi)\hat{I}_y)\exp\left(-\mathrm{i}\,\omega_{\mathrm{rf}} t \hat{I}_z\right). \end{aligned} \tag{2.71}$$

Splitting the above equation into two parts C and D, and solving first for C, where

$$C = \exp\left(\mathrm{i}\,\omega_{\mathrm{rf}} t \hat{I}_z\right)(\omega_0 \hat{I}_z)\exp\left(-\mathrm{i}\,\omega_{\mathrm{rf}} t \hat{I}_z\right), \tag{2.72}$$

this equation can be expanded using the Baker-Campbell-Hausdorf (BCH) formula, which gives the expansion series for [42]

$$\exp(-at)A\exp(at), \tag{2.73}$$

as

$$A - \frac{(t)}{1!}[a,A] + \frac{(t)^2}{2!}[a,[a,A]] - \frac{(t)^3}{3!}[a,[a,[a,A]]] + \cdots, \tag{2.74}$$

therefore, using eq. (2.72), and (2.74), the part C simplifies to

$$C = \omega_0 \hat{I}_z, \tag{2.75}$$

since commutation $\left[\hat{I}_z, \hat{I}_z\right] = 0$.
To solve D, we have

$$\begin{aligned} D = \exp\left(\mathrm{i}\,\omega_{\mathrm{rf}} t \hat{I}_z\right)(\omega_{B_1}\cos(\omega_{\mathrm{rf}} t + \phi)\hat{I}_x \\ + \omega_{B_1}\sin(\omega_{\mathrm{rf}} t + \phi)\hat{I}_y)\exp\left(-\mathrm{i}\,\omega_{\mathrm{rf}} t \hat{I}_z\right), \end{aligned} \tag{2.76}$$

where for the ease of calculation, we will split D into F and G such that

$$F = \exp\left(\mathrm{i}\omega_{\mathrm{rf}} t\hat{I}_z\right)\left(\omega_{B_1}\cos\left(\omega_{\mathrm{rf}} t + \phi\right)\hat{I}_x\right)\exp\left(-\mathrm{i}\omega_{\mathrm{rf}} t\hat{I}_z\right), \tag{2.77}$$

and

$$G = \exp\left(\mathrm{i}\omega_{\mathrm{rf}} t\hat{I}_z\right)\left(\omega_{B_1}\sin\left(\omega_{\mathrm{rf}} t + \phi\right)\hat{I}_x\right)\exp\left(-\mathrm{i}\omega_{\mathrm{rf}} t\hat{I}_z\right). \tag{2.78}$$

Since ω_{B_1} is constant, we can rewrite eq. (2.77) as

$$F = \omega_{B_1}\left(\exp\left(\mathrm{i}\omega_{\mathrm{rf}} t\hat{I}_z\right)\hat{I}_x\exp\left(-\mathrm{i}\omega_{\mathrm{rf}} t\hat{I}_z\right)\right)\left(\cos\left(\omega_{\mathrm{rf}} t + \phi\right)\right). \tag{2.79}$$

The part F is now similar to eq. (2.73), except for the order of the terms. Therefore, we can use the BCH formula [42] to solve it which gives

$$\begin{aligned} F = \omega_{B_1}\Big(&\hat{I}_x - \frac{\mathrm{i}t}{1!}\left[-\omega_{\mathrm{rf}}\hat{I}_z, \hat{I}_x\right] \\ &+ \frac{(\mathrm{i}t)^2}{2!}\left[-\omega_{\mathrm{rf}}\hat{I}_z, \left[-\omega_{\mathrm{rf}}\hat{I}_z, \hat{I}_x\right]\right] \\ &- \frac{(\mathrm{i}t)^3}{3!}\left[-\omega_{\mathrm{rf}}\hat{I}_z, \left[-\omega_{\mathrm{rf}}\hat{I}_z, \left[-\omega_{\mathrm{rf}}\hat{I}_z, \hat{I}_x\right]\right]\right] + \cdots\Big)\left(\cos\left(\omega_{\mathrm{rf}} t + \phi\right)\right). \end{aligned} \tag{2.80}$$

Since $\hat{I}_x, \hat{I}_y, \hat{I}_z$, have cyclic commutation, therefore, $\left[\hat{I}_z, \hat{I}_x\right] = \mathrm{i}\hat{I}_y$. Simplifying the above eq. using this we get

$$\begin{aligned} F = \omega_{B_1}\Big(&\hat{I}_x - \frac{\mathrm{i}t}{1!}\left(-\mathrm{i}\omega_{\mathrm{rf}}\hat{I}_y\right) \\ &+ \frac{(\mathrm{i}t)^2}{2!}\left[-\omega_{\mathrm{rf}}\hat{I}_z, -\mathrm{i}\omega_{\mathrm{rf}}\hat{I}_y\right] \\ &- \frac{(\mathrm{i}t)^3}{3!}\left[-\omega_{\mathrm{rf}}\hat{I}_z, \left[-\omega_{\mathrm{rf}}\hat{I}_z, -\mathrm{i}\omega_{\mathrm{rf}}\hat{I}_y\right]\right] + \cdots\Big)\cos\left(\omega_{\mathrm{rf}} t + \phi\right). \end{aligned} \tag{2.81}$$

Similarly, $[\hat{I}_z, \hat{I}_y] = -\mathrm{i}\hat{I}_x$, since it is in the reverse direction

$$\begin{aligned} F = \omega_{B_1}(\hat{I}_x - \frac{\omega_{\mathrm{rf}} t}{1!}(\hat{I}_y) \\ + \frac{(\mathrm{i}t\omega_{\mathrm{rf}})^2}{2!}(\hat{I}_x) \\ - \frac{(\mathrm{i}t)^3}{3!}\left[-\omega_{\mathrm{rf}}\hat{I}_z, \omega_{\mathrm{rf}}^2\hat{I}_x\right] + \cdots)\cos(\omega_{\mathrm{rf}}t + \phi). \end{aligned} \tag{2.82}$$

On further simplification

$$\begin{aligned} F = \omega_{B_1}(\hat{I}_x - \frac{\omega_{\mathrm{rf}} t}{1!}(\hat{I}_y) \\ + \frac{(\mathrm{i}t\omega_{\mathrm{rf}})^2}{2!}(\hat{I}_x) \\ + \frac{(\mathrm{i}t\omega_{\mathrm{rf}})^3}{3!}(\mathrm{i}\hat{I}_y) + \cdots)\cos(\omega_{\mathrm{rf}}t + \phi). \end{aligned} \tag{2.83}$$

We obtain alternating terms of $\hat{I}_x$ and $\hat{I}_y$. Re-writing them separately we get

$$\begin{aligned} F = \omega_{B_1}(\hat{I}_x(1 - \frac{(t\omega_{\mathrm{rf}})^2}{2!} + \frac{(t\omega_{\mathrm{rf}})^4}{4!} - \cdots) \\ - \hat{I}_y(\frac{\omega_{\mathrm{rf}} t}{1!} - \frac{(t\omega_{\mathrm{rf}})^3}{3!} + \cdots))\cos(\omega_{\mathrm{rf}}t + \phi). \end{aligned} \tag{2.84}$$

The multiplication terms of $\hat{I}_x$ and $\hat{I}_y$ are Taylor series expansions for *cos* and *sin* respectively, where the angle is $\omega_{\mathrm{rf}} t$. Therefore,

$$F = \omega_{B_1}(\hat{I}_x \cos(\omega_{\mathrm{rf}}t) - \hat{I}_y \sin(\omega_{\mathrm{rf}}t))\cos(\omega_{\mathrm{rf}}t + \phi). \tag{2.85}$$

Similarly, if we solve for G we get

$$G = \omega_{B_1}(\hat{I}_x \sin(\omega_{\mathrm{rf}}t) + \hat{I}_y \cos(\omega_{\mathrm{rf}}t))\sin(\omega_{\mathrm{rf}}t + \phi). \tag{2.86}$$

Adding F and G to get D

$$\begin{aligned} D = \omega_{B_1}(\hat{I}_x \cos(\omega_{\mathrm{rf}} t) - \hat{I}_y \sin(\omega_{\mathrm{rf}} t)) \cos(\omega_{\mathrm{rf}} t + \phi) \\ + \omega_{B_1}(\hat{I}_x \sin(\omega_{\mathrm{rf}} t) + \hat{I}_y \cos(\omega_{\mathrm{rf}} t)) \sin(\omega_{\mathrm{rf}} t + \phi). \end{aligned} \tag{2.87}$$

Expanding the terms and separating the $\hat{I}_x$ and $\hat{I}_y$ terms we get

$$\begin{aligned} D = \omega_{B_1}(\hat{I}_x(\cos(\omega_{\mathrm{rf}} t)\cos(\omega_{\mathrm{rf}} t + \phi) + \sin(\omega_{\mathrm{rf}} t)\sin(\omega_{\mathrm{rf}} t + \phi)) \\ + \hat{I}_y(\cos(\omega_{\mathrm{rf}} t)\sin(\omega_{\mathrm{rf}} t + \phi) - \sin(\omega_{\mathrm{rf}} t)\cos(\omega_{\mathrm{rf}} t + \phi))) \end{aligned}. \tag{2.88}$$

Using trigonometric properties the equation reduces to

$$D = \omega_{B_1}(\hat{I}_x(\cos(\phi + \omega_{\mathrm{rf}} t - \omega_{\mathrm{rf}} t) + \hat{I}_y(\sin(-\omega_{\mathrm{rf}} t) + \omega_{\mathrm{rf}} t + \phi))), \tag{2.89}$$

$$= \omega_{B_1}(\hat{I}_x(\cos(\phi) + \hat{I}_y(\sin(\phi))). \tag{2.90}$$

Now combining C and D to get B

$$B = \omega_0 \hat{I}_z + \omega_{B_1}(\hat{I}_x(\cos(\phi) + \hat{I}_y(\sin(\phi))), \tag{2.91}$$

and finally combining A and B to get $\hat{H}_{\mathrm{Rot}}$ the result is

$$\hat{H}_{\mathrm{Rot}} = (\omega_0 - \omega_{\mathrm{rf}})\hat{I}_z + \omega_{B_1}(\hat{I}_x(\cos(\phi) + \hat{I}_y(\sin(\phi))) \tag{2.92}$$

. If $\omega_0 - \omega_{\mathrm{rf}} = \Omega$, then

$$\hat{H}_{\mathrm{Rot}} = \Omega \hat{I}_z + \omega_{B_1}(\hat{I}_x(\cos(\phi) + \hat{I}_y(\sin(\phi))). \tag{2.93}$$

In this section, we found the NMR Hamiltonian in the rotating frame of reference, which is used in the Liouville-von Neumann equation to find spin evolution [38, 39].

2.1.6 Spin density operator in the equilibrium state

To find the evolution of the spins with time t, we need to know their initial condition at time $t = 0$, or at the beginning of the experiment.
To find the initial condition we assume that the sample is placed in B_0, which is not yet perturbed by an external RF field. Another assumption is that it is an isolated system; therefore, at thermal equilibrium, the spin population obeys the Boltzmann distribution and there is no coherence among the states. Therefore, with these assumptions the population probability of the spins for such a system is

$$\hat{\rho}^{eq}(0) = \begin{pmatrix} n_\alpha/N & 0 \\ 0 & n_\beta/N \end{pmatrix}, \tag{2.94}$$

where n_α is the number of spins in the state α, n_β is the number of spins in the state β, and N is the total number of spins. The population in any one of the states is [38, 39]

$$n_\alpha = \frac{1}{2} N \exp(-E_\alpha/k_B T), \tag{2.95}$$

and

$$n_\beta = \frac{1}{2} N \exp\big(-E_\beta/k_B T\big), \tag{2.96}$$

as the spins obey the Boltzmann distribution. Using high-temperature approximation

$$E/k_B T \ll 1, \tag{2.97}$$

and Taylor series expansion the spin populations simplified for α and β states are

$$n_\alpha = \frac{1}{2} N (1 - E_\alpha/k_B T), \tag{2.98}$$

and

$$n_\beta = \frac{1}{2} N (1 - E_\beta/k_B T), \tag{2.99}$$

respectively [38, 39].

The energy of the α and β states are given as

$$E_\alpha = -\frac{1}{2}\hbar\omega_0, \tag{2.100}$$

and

$$E_\beta = \frac{1}{2}\hbar\omega_0. \tag{2.101}$$

and inserting them in eq. (2.100) and (2.101) gives

$$n_\alpha = \frac{1}{2}N(1+\hbar\omega_0/2k_BT), \tag{2.102}$$

and

$$n_\beta = \frac{1}{2}N(1-\hbar\omega_0/2k_BT), \tag{2.103}$$

respectively [38, 39]. Using the numbers of spins in their α and β states in eq. (2.94) will give the equilibrium distribution in a matrix form as

$$\hat{\rho}^{eq}(0) = \begin{pmatrix} \frac{1}{2}+\hbar\omega_0/4k_BT & 0 \\ 0 & \frac{1}{2}-\hbar\omega_0/4k_BT \end{pmatrix}. \tag{2.104}$$

Simplifying it

$$\hat{\rho}^{eq}(0) = \begin{pmatrix} \frac{1}{2} & 0 \\ 0 & \frac{1}{2} \end{pmatrix} + \omega_0/k_BT \begin{pmatrix} +\hbar/2 & 0 \\ 0 & -\hbar/2 \end{pmatrix}. \tag{2.105}$$

Since the first matrix is invariable to any operation and the second matrix is proportional to the $\hat{I}_z$ operator (from eq. (2.29)), the initial density of states can be approximated to [38, 39]

$$\hat{\rho}^{eq}(0) \propto \hat{I}_z \tag{2.106}$$

where the constant terms can be introduced later.

From the above derivation, it can be concluded that the net magnetisation for a spin system is aligned along the B_0 direction when it is at its equilibrium condition.

2.1.7 Evolution of the magnetisation in NMR

As seen from the derivation till now, it is possible to represent the ensemble of spins and form a density matrix. The density matrix represents the net magnetisation of the system. The evolution of the density matrix in the Schrödinger's equation results in the Liouville-von Neumann equations [39, 41]. Since the solution of the Liouville-von Neumann equations consists of Hamiltonian terms in a rotating frame of reference. The transformation from a laboratory frame to a rotating frame was done with respect to the RF oscillation. Finally, in the previous section, we derived the net magnetisation at the equilibrium position, i.e., at the initial stage of the experiment, which was given as

$$\hat{\rho}(0) \propto \hat{I}_z. \tag{2.107}$$

Now to find the observable NMR signal we will follow the sequence as shown in fig. 2.5. For a conventional NMR experiment there exists mainly three states, first: the equilibrium condition at $t = 0$, second: irradiation of an $\pi/2$ RF pulse for time t_1, and third: relaxation and free induction decay (FID) of the magnetisation during time t_2. By recording the signal during the FID, we can observe an NMR signal [38, 39].
Since we know $\hat{\rho}(0)$, we can calculate $\hat{\rho}(t_1)$, from the Liouville-von Neumann equation [39]. Therefore, from eq. (2.93) the Hamiltonian in rotating frame for an RF perturbation is given as

$$\hat{H}_{\text{Rot-rf}} = \omega_{B_1}(\hat{I}_x cos(\phi) + \hat{I}_y sin(\phi)). \tag{2.108}$$

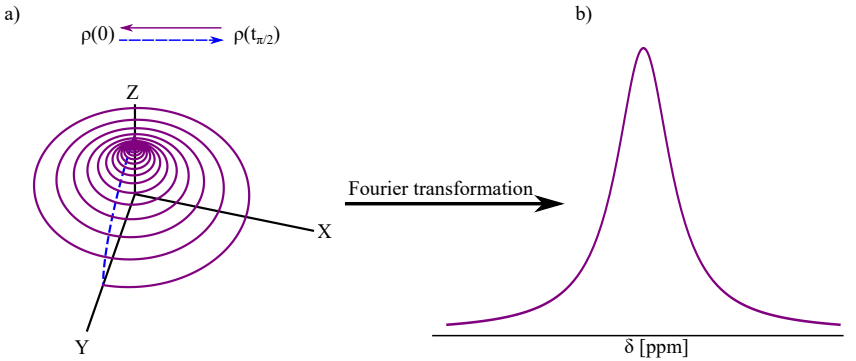

Figure 2.5: (a) Evolution of the magnetisation during a conventional NMR process. In the equilibrium state, the density of states or the net magnetisation ($\rho(0)$) are aligned along the B_0, in the z-direction. When a $\pi/2$ RF-pulse is applied, it causes the magnetisation to flip in the x-y plane. The density function $\rho(t_{\pi/2})$ represents the magnetisation in this state. The relaxation of the magnetisation from the state $\rho(t_{\pi/2})$ to $\rho(0)$ is called free induction decay (FID), which is recorded by a receiver coil. (b) The Fourier transformation of the time-dependent signal acquired by the coil reveals the NMR signal in the frequency domain, where ppm scale is the relative frequency shift, with respect to a referenced frequency.

At the beginning of the derivation, we assumed a circularly polarised RF B_1. If we now assume a uni-directional B_1. The above equation reduces to

$$\hat{H}_{\text{Rot-rf}} = \omega_{B_1} \hat{I}_y. \tag{2.109}$$

From the solution Liouville-von Neumann given by eq. (2.60), we can find the state of the magnetisation after time t_1 as

$$\hat{\rho}(t_1) = \exp\left(-\mathrm{i}\omega_{B_1} \hat{I}_y t_1\right) \hat{\rho}(0) \exp\left(\mathrm{i}\omega_{B_1} \hat{I}_y t_1\right) \tag{2.110}$$

,

$$\hat{\rho}(t_1) = \exp\left(-\mathrm{i}\omega_{B_1} \hat{I}_y t_1\right) \hat{I}_z \exp\left(\mathrm{i}\omega_{B_1} \hat{I}_y t_1\right), \tag{2.111}$$

and by using the BCH expansion [42] we get

$$\begin{aligned}\hat{\rho}(t_1) = \hat{I}_z &- \frac{\mathrm{i}t_1}{1!}\left[\omega_{B_1}\hat{I}_y, \hat{I}_z\right] \\ &+ \frac{(\mathrm{i}t_1)^2}{2!}\left[\omega_{B_1}\hat{I}_y, \left[\omega_{B_1}\hat{I}_y, \hat{I}_z\right]\right] \\ &- \frac{(\mathrm{i}t_1)^3}{3!}\left[\omega_{B_1}\hat{I}_y, \left[\omega_{B_1}\hat{I}_y, \left[\omega_{B_1}\hat{I}_y, \hat{I}_z\right]\right]\right] + \cdots .\end{aligned} \tag{2.112}$$

Simplifying the above eq. similar to the steps from eq. (2.79) to (2.85) [38, 39]

$$\hat{\rho}(t_1) = \hat{I}_z(\cos(\omega_{B_1}t_1)) + \hat{I}_x(\sin(\omega_{B_1}t_1)). \tag{2.113}$$

Since the pulse applied is to flip the spins by $\pi/2$; therefore, from the equation of flip angle

$$\omega_{B_1}t_1 = \pi/2 \tag{2.114}$$

the above equation is further reduced to

$$\hat{\rho}(t_1) = \hat{I}_x. \tag{2.115}$$

Now to find $\hat{\rho}(t_2)$, during the FID, the Hamiltonian in the rotating frame will be given as [38, 39]

$$\hat{H}_{\text{Rot-FID}} = \Omega\hat{I}_z, \tag{2.116}$$

and using the same procedure to calculate the state of the magnetisation after time t_2 we get

$$\hat{\rho}(t_2) = \exp\left(-\mathrm{i}\Omega\hat{I}_z t_2\right)\hat{I}_x \exp\left(\mathrm{i}\Omega\hat{I}_z t_2\right). \tag{2.117}$$

Following the BCH expansion [42] and simplifying the equation gives [38, 39]

$$\hat{\rho}(t_2) = \hat{I}_x(\cos(\Omega t_2)) + \hat{I}_y(\sin(\Omega t_2)). \tag{2.118}$$

We now know the density operator at the end of the NMR experiment. From eq. (2.118) it can be seen that the net magnetisation is freely precessing in an x-y

plane. To find the NMR signal or the observable we need to observe the spins in the x-y plane. This can be presented by a ladder-plus operator as [38, 39]

$$\hat{I}^{+} = \hat{I}_x + \mathrm{i}\hat{I}_y, \tag{2.119}$$

therefore, the observable signal can be determined by taking the trace of the ladder plus operator with the density operator during the FID [38, 39],

$$\langle \overline{\mathrm{FID}} \rangle = \mathrm{Tr}\left\{\hat{I}^{+}\hat{\rho}(t_2)\right\}. \tag{2.120}$$

Since

$$\mathrm{Tr}\left\{\hat{I}^{+}\hat{\rho}(t_2)\right\} = \mathrm{Tr}\left\{\hat{\rho}(t_2)\hat{I}^{+}\right\}, \tag{2.121}$$

therefore,

$$\mathrm{Tr}\left\{\hat{I}^{+}\hat{\rho}(t_2)\right\} = \hat{I}^{+}\cdot\hat{\rho}(t_2). \tag{2.122}$$

On writing the operator terms we get

$$\mathrm{Tr}\left\{\hat{I}^{+}\hat{\rho}(t_2)\right\} = (\hat{I}_x(\cos(\Omega t_2)) + \hat{I}_y(\sin(\Omega t_2)))(\hat{I}_x + \mathrm{i}\hat{I}_y), \tag{2.123}$$

and expanding the equation we get

$$\begin{aligned}\mathrm{Tr}\left\{\hat{I}^{+}\hat{\rho}(t_2)\right\} = \hat{I}_x^2\cos(\Omega t_2) + \hat{I}_x\hat{I}_y(\sin(\Omega t_2)) \\ + \mathrm{i}\hat{I}_x\hat{I}_y(\cos(\Omega t_2)) + \mathrm{i}\hat{I}_y^2(\sin(\Omega t_2).\end{aligned} \tag{2.124}$$

Using the equation from the $\hat{I}_z$,$\hat{I}_x$ and $\hat{I}_y$ operator, i.e, from eq. (2.29),(2.30), and (2.31) respectively, the terms can be solved with normal matrix multiplication. On simplification

$$\mathrm{Tr}\left\{\hat{I}^{+}\hat{\rho}(t_2)\right\} = \frac{\hbar^2}{4}(\cos(\Omega t_2) + \mathrm{i}\sin(\Omega t_2)), \tag{2.125}$$

or

$$\mathrm{Tr}\left\{\hat{I}^{+}\hat{\rho}(t_2)\right\} = \frac{\hbar^2}{4}e^{\mathrm{i}\Omega t_2}. \tag{2.126}$$

After applying an RF pulse, the spins will tend to relax to a lower energy state or their initial state. Therefore, the only term missing in the observation equation is the relaxation term. Since the relaxation can be defined by an exponential function, we assume R_2 as the decay rate for transverse relaxation [38,39]. Therefore, the final equation is

$$\mathrm{Tr}\left\{\hat{I}^{+}\hat{\rho}(t_2)\right\} = \frac{\hbar^2}{4} e^{\mathrm{i}\Omega t_2} e^{-R_2 t_2} \tag{2.127}$$

If we plot this equation we get the FID, and by taking the Fourier transformation from time to frequency space we get the spectrum, where R_2 determines the linewidth assuming everything else is in perfect conditions [38,39].

To summarise the discussion so far, the section explained the evolutionary phase of the net magnetisation in a conventional NMR experiment. The magnetisation conditions were derived for a simple isolated $I = 1/2$ system. However, taking into account other parameters such as nuclear shielding tensor, J-coupling, more than two levels of degeneracy etc., the Hamiltonian and the spin operators can be modified. Since this is out of the scope of the dissertation, these conditions are not derived here.

In the next section, we will use the approach discussed for determining the NMR signal and try to derive the Hamiltonian and conditions which would lead to a chiral signal.

2.2 NMR for a chiral molecule in the presence of an RF electric field

NMR cannot reveal the handedness of a chiral molecule directly. The reason is that the nuclear shielding tensor and the J-coupling tensor are even under parity [13]. Therefore, regardless of the handedness of the molecule the NMR spectra will be same for the enantiomer pairs. If we take an example of a chiral molecule 1,1,1-trifluoropropan-2-ol. If a spectroscopist acquires spectra for (R) and (S)-enantiomer, it will be similar to if one needs to distinguish between (R)-C3H5F3O and (S)-C3H5F3O just by looking at their chemical formulae. The

task seems impossible without additional information. Similarly, the task of distinguishing chiral molecules directly cannot be achieved with simple NMR measurement. To solve the problem, there needs to be additional information provided, i.e., detail of a three-dimensional (3-D) structure of the enantiomers. Similarly, an odd parity term needs to be present in the NMR Hamiltonian, which would then automatically take care of the handedness of the enantiomers.

As discussed in chapter 1, optical activity is an inherent property of chiral molecules. One of the first experiments, where optical activity in chiral molecules was observed by Jean-Baptiste Biot in 1812. The polarization of plane-polarised light passing through the enantiomer produced a rotation [43].

Following a similar approach, in 2004 A.D. Buckingham [13] theoretically showed that when a chiral molecule is placed in a strong magnetic field, the spins are coupled to an electric dipole, where the coupling factor is an odd parity tensor. The assumption was based on the findings of the experiments of [44], where a rotating electric polarisation was detected for the ^{35}Cl at noncentrosymmetric sites and relative silence when placed at centrosymmetric sites. This combined with the theory of optics laid the basis of the derivation by A.D. Buckingham [13], where he postulated that an odd parity tensor is produced for chiral molecules, which acts as a coupling factor between an electric dipole, and rotating magnetic moment of a nucleus in a molecule. It was also postulated that a magnetic field is produced around the nucleus in the presence of an oscillating electric field for the chiral molecules. The dependencies were postulated by the equations below,

$$\vec{\mu}^{(N)} = \overline{\xi}^{(N)} \vec{m}^{(N)} \times \vec{B}^0 + \omega^{-1} \xi'^{(N)} \frac{\partial \vec{m}^{(N)}}{\partial t} + \cdots , \tag{2.128}$$

$$\vec{B}^{(N)} = (1 - \sigma^{(N)}) \vec{B}^0 - \overline{\xi}^{(N)} \vec{E} \times \vec{B}^0 - \omega^{-1} \xi'^{(N)} \frac{\partial \vec{E}}{\partial t} + \cdots . \tag{2.129}$$

The above equations are taken from [13] eq. (11) and (12), where $^{(N)}$ represents the nucleus, $\vec{B}^0$ represents the static magnetic field, and $\overline{\xi}^{(N)}$ represents the odd parity tensor which vanishes for achiral molecules.

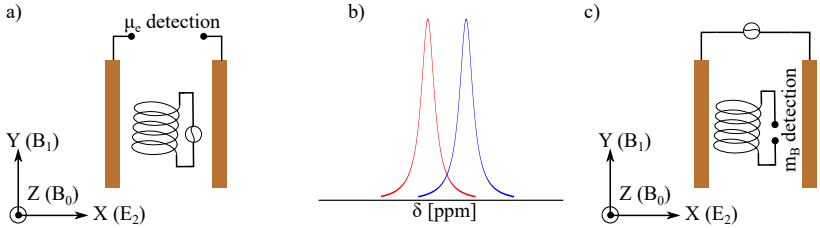

Figure 2.6: The figure summarises the discussion for chiral detection schemes with different possibilities under a strong static magnetic field (B_0) as suggested by [14]. (a) The chiral distinction is made possible by sensing the electric dipole induced by placing two capacitor plates close to the sample. The direction of the electric dipole will be opposite in sense for the enantiomer pairs. (b) The chiral distinction is made possible by the chemical shift produced. For this type of measurement, the system needs to be shimmed finely to produce linewidths in the range of a few Hz as the chemical shifts are predicted to be in the range of mHz. (c) The final possibility is by detecting any changes produced in the magnetic dipole for the enantiomer pairs, when an E_2 is applied.

From these relations, it was shown by [14], that similar to the magnetic field, the oscillating electric field produces a magnetic moment which is related as

$$\vec{m}^{(N)} = (1-\sigma^{(N)})\vec{m}^{(N)} - \overline{\xi}^{(N)}\vec{E}\times\vec{m}^{(N)} - \omega^{-1}\xi'^{(N)}\frac{\partial\vec{E}}{\partial t} + \cdots . \tag{2.130}$$

Therefore, there are three ways to detect the chiral molecules which are [14]:

- Measure the direction of the electric dipole induced, which would be opposite in sense for the enantiomer pairs.
- Measure the chemical shift produced due to the magnetic field produced around the nucleus when an RF electric field is applied.
- Measure the change in the magnetic dipole for the two enantiomers when an RF electric field is applied.

From the three possibilities discussed above, the dissertation focuses on the later part, i.e., the measurement of the magnetic moment induced when an RF electric field is applied (E_2). The reason is that the NMR spectroscopy setup is prepared for this kind of measurement setup. To measure the chemical shifts would have been a challenge, since shimming precisely to few Hz depends on lots of fac-

tors, some of which are not in user-controlled e.g., the shim coil temperature, sample temperature, exact sample filling volume etc [38]. This technique would have also required contaminating the chiral sample for referencing the shifts to a known value.

Since, there can be two forms of electric field sources, namely, oscillating and non-oscillating, it was shown by [45], that when an oscillating electric field is applied, the chiral signal is enhanced by an order proportional to the frequency of oscillation. A significant enhancement when compared to a non-oscillating source, as the ω_0 is in the range of MHz.

By applying an RF E_2, for a chiral molecule, we can now introduce the odd parity tensor in the NMR Hamiltonian as [45],

$$\hat{H}_{\text{chiral-Lab}} = \omega_0 \hat{I}_z + \omega_{B_1} \cos(\omega_{\text{rf}} t)\hat{I}_x \pm \sigma_c \gamma_r (\vec{E}_2(t) \sin(\omega_{\text{rf}} t) \times \vec{B}_0) \cdot \hat{I}_x, \quad (2.131)$$

which is similar to the NMR Hamiltonian, but instead, there is an additional term representing E_2 perturbation, which is present only in a chiral molecule. The tensor σ_c, is opposite in sign for the pair of enantiomers and vanishes for achiral molecules. In the dissertation, $\pm$[1] represents the difference in the signs produced due to the structure of the enantiomer pairs. The second term is the B_1 and can be regarded as noise or an unwanted part of the signal for chiral detection. For further derivations, it was assumed that the phase difference between the E_2 and B_1 due to the change in the material properties is negligible.

Similar to the spin evolution defined for the NMR, we will use the density function approach to find the state of the net magnetisation at each evolution step of the measurement. The solution of the Liouville-von Neumann equation for the calculation is used. In order to do that, we need to again transform the Hamiltonian from a laboratory frame of reference to a rotating frame of reference.

[1] $\pm$ is used for the enantiomer pair in the Hamiltonian, since the electrical dipoles of the enantiomer pair are in the opposite direction due to asymmetry. The additional term in the Hamiltonian flips the net magnetisation, either along the flip direction (indicated by "$+$"), or in the opposite direction (indicated by "$-$").

2.2.1 Transformation of the chiral Hamiltonian from the laboratory to a rotating frame of reference

The Hamiltonian for a spin-1/2 system, with an E_2 applied to it, was defined by eq. (2.131). The simplified form of this Hamiltonian is

$$\hat{H}_{\text{chiral-Lab}} = \omega_0 \hat{I}_z + \omega_{B_1} \cos(\omega_{\text{rf}} t)\hat{I}_x \pm \omega_{E_2} \sin(\omega_{\text{rf}} t)\hat{I}_x. \tag{2.132}$$

Here we have assumed that the magnetic field due to the E_2 in the z-direction is negligible compared to the B_0 field. Similar to the magnetic nutation frequency defined by eq. (2.46), an analogous electrical nutation frequency ω_{E_2} is defined, which is

$$|\omega_{E_2}| = |\sigma_c E_2 B_0 \gamma_r|/2, \tag{2.133}$$

where, σ_c (in the order of 1×10^{-15} m/V) [46] is opposite in magnitude for the enantiomer pairs. Similar to the NMR Hamiltonian transformation, we will transform the NMR chiral Hamiltonian from the laboratory frame of reference to the rotating frame of reference using ω_{rf} as the unitary operator. The Zeeman term converts to

$$\hat{H}_{\text{Rot}} = (\omega_0 - \omega_{\text{rf}})\hat{I}_z. \tag{2.134}$$

For the RF terms, the magnetic and the electric part of the Hamiltonian were transformed separately. First for the associated magnetic field

$$\hat{H}_{\text{Rot-B}_1} = \exp\left(\mathrm{i}\omega_{\text{rf}} t \hat{I}_z\right)(\omega_{B_1} \cos(\omega_{\text{rf}} t)\hat{I}_x)\exp\left(-\mathrm{i}\omega_{\text{rf}} t \hat{I}_z\right), \tag{2.135}$$

which is similar to eq. (2.77); therefore, the transformation leads to

$$\hat{H}_{\text{Rot-B}_1} = \omega_{B_1}(\hat{I}_x \cos(\omega_{\text{rf}} t) - \hat{I}_y \sin(\omega_{\text{rf}} t))\cos(\omega_{\text{rf}} t). \tag{2.136}$$

Similarly, for the Hamiltonian part due to E_2 perturbation

$$\hat{H}_{\text{Rot-E}_2} = \exp\left(\mathrm{i}\omega_{\text{rf}} t \hat{I}_z\right) \pm \omega_{E_2} \sin(\omega_{\text{rf}} t)\hat{I}_x \exp\left(-\mathrm{i}\omega_{\text{rf}} t \hat{I}_z\right) \tag{2.137}$$

using the BCH approximation [42],

$$\hat{H}_{\text{Rot-E}_2} = \pm\omega_{E_2}(\hat{I}_x\cos(\omega_{\text{rf}}t) - \hat{I}_y\sin(\omega_{\text{rf}}t))\sin(\omega_{\text{rf}}t). \tag{2.138}$$

From equation (2.136) and (2.138), if we combine the RF perturbations, the resultant Hamiltonian is

$$\begin{aligned}\hat{H}_{\text{Rot-B}_1\text{E}_2} =& \pm\omega_{E_2}(\hat{I}_x\cos(\omega_{\text{rf}}t) - \hat{I}_y\sin(\omega_{\text{rf}}t))\sin(\omega_{\text{rf}}t) \\ &+ \omega_{B_1}(\hat{I}_x\cos(\omega_{\text{rf}}t) - \hat{I}_y\sin(\omega_{\text{rf}}t))\cos(\omega_{\text{rf}}t).\end{aligned} \tag{2.139}$$

To simplify the equation we use the trigonometric properties defined below,

$$\cos a\sin a = \frac{1}{2}(\sin 2a), \tag{2.140}$$

$$\sin^2 a = \frac{1}{2}(1-\cos 2a), \tag{2.141}$$

and

$$\cos^2 a = \frac{1}{2}(\cos 2a - 1). \tag{2.142}$$

On solving the RF perturbation Hamiltonian, based on the above properties there will be a $2\omega_{\text{rf}}$ oscillation produced in the Hamiltonian. To simplify the calculations, we assume that the terms, which generate frequencies of $2\omega_{\text{rf}}$, can be neglected. The reason for this is that the detectors would be matched and tuned to ω_{rf}, therefore, $2\omega_{\text{rf}}$ will not be transmitted or detected by the resonator. Hence, the RF perturbation part of the chiral Hamiltonian then is

$$\hat{H}_{\text{Rot-B}_1\text{E}_2} = -\omega_{B_1}\hat{I}_x \mp \omega_{E_2}\hat{I}_y \tag{2.143}$$

Combining the Zeeman term and the RF part of the chiral Hamiltonian, the final result is

$$\hat{H}_{\text{chiral-Rot}} = (\omega_0 - \omega_{\text{rf}})\hat{I}_z - \omega_{B_1}\hat{I}_x \mp \omega_{E_2}\hat{I}_y, \tag{2.144}$$

which, is in good agreement with the Hamiltonian derived by [45]. However, B_1 was neglected in the Hamiltonian by [45]. This can be realised if the detector is designed such that B_1 is aligned along the B_0 direction. The problems and challenges of designing such detectors are discussed in chapter 3. Therefore, for to study the evolution of the magnetisation, we have taken the effect of the associated B_1 field into account. Based on it, we presented different scenarios that could enable chiral signal detection, and also scenarios that should be avoided as they could have led to the weakening of the detectable chiral signal.

2.2.2 Calculation of the net magnetisation for a chiral molecule in the presence of an RF electric fields

After transforming the chiral Hamiltonian to a rotating frame of reference, we can now calculate the density operator over time as we did for the NMR experiment. When the spin-1/2 isolated system is placed in B_0, similar to section 2.1.6, the initial density of states can be approximated to

$$\hat{\rho}(0) \propto \hat{I}_z \tag{2.145}$$

When the system is perturbed by an RF pulse, the magnetic moments are influenced due to E_2 and B_1. The net magnetisation is the result of the influence of the magnetic moment produced by these two fields.
The z-components of the RF magnetic fields have been ignored, as it is negligible compared to the magnitude of B_0, in which the samples was placed. For this example, we consider that the chiral molecule is placed in a magnetic field strength of 11.74 T. For the chiral distinction, we assume that the RF pulse applied is for time t_1. The RF perturbation Hamiltonian will be given as

$$\hat{H}_{\text{Rot-B}_1\text{E}_2} = -\omega_{B_1}\hat{I}_x \mp \omega_{E_2}\hat{I}_y. \tag{2.146}$$

The density operator from an initial state after time t_1 can be found from the solution of the Liouville-von Neumann equation [39], which is

$$\hat{\rho}(t_1) = \exp\Big(-\mathrm{i}\hat{H}_{\text{Rot-B}_1\text{E}_2}\, t_1\Big)\hat{I}_z \exp\Big(\mathrm{i}\hat{H}_{\text{Rot-B}_1\text{E}_2}\, t_1\Big), \tag{2.147}$$

which leads to

$$\hat{\rho}(t_1) = \exp\big(\mathrm{i}(\omega_{B_1}\hat{I}_x \pm \omega_{E_2}\hat{I}_y)t_1\big)\hat{I}_z \exp\big(-\mathrm{i}(\omega_{B_1}\hat{I}_x \pm \omega_{E_2}\hat{I}_y)t_1\big). \tag{2.148}$$

Further simplifying the equation by separating the E-field and B-field perturbation we get

$$\hat{\rho}(t_1) = \exp\big(\pm\mathrm{i}\,\omega_{E_2}\hat{I}_y t_1\big)\exp\big(\mathrm{i}\,\omega_{B_1}\hat{I}_x t_1\big)\hat{I}_z \exp\big(-\mathrm{i}\,\omega_{B_1}\hat{I}_x t_1\big)\exp\big(\mp\mathrm{i}\,\omega_{E_2}\hat{I}_y t_1\big). \tag{2.149}$$

For ease, we solve B_1 perturbation first, i.e.,

$$\hat{\rho}_{B_1}(t_1) = \exp\big(\mathrm{i}\,\omega_{B_1}\hat{I}_x t_1\big)\hat{I}_z \exp\big(-\mathrm{i}\,\omega_{B_1}\hat{I}_x t_1\big). \tag{2.150}$$

Expanding using the BCH formula [42], and simplifying the above equation we get

$$\hat{\rho}_{B_1}(t_1) = (\hat{I}_z \cos(\omega_{B_1} t) + \hat{I}_y \sin(\omega_{B_1} t)), \tag{2.151}$$

and adding the missing terms

$$\hat{\rho}(t_1) = \exp\big(\pm\mathrm{i}\,\omega_{E_2}\hat{I}_y t_1\big)\cdot\big(\hat{I}_z \cos(\omega_{B_1} t_1) + \hat{I}_y \sin(\omega_{B_1} t_1)\big)\cdot\exp\big(\mp\mathrm{i}\,\omega_{E_2}\hat{I}_y t_1\big). \tag{2.152}$$

From here, we assumed three scenarios that can be produced due to the B_1 perturbations. These are; flipping the net magnetisation by an arbitrary angle, $\pi/2$ flipping of the magnetisation, and finally, π flipping. Based on these cases, the above equation was solved to find the best possible scenario to detect a chiral signal generated. All these cases are discussed in the following subsections.

2.2.3 Net magnetisation flipped at an arbitrary angle

A closer approximation to the real-world environment would be to consider an arbitrary flipping of the magnetisation by the combination of E_2 and B_1 perturbations. Therefore, for this particular case starting from eq. (2.152)

$$\hat{\rho}(t_1) = \exp\left(\pm \mathrm{i}\,\omega_{E_2}\hat{I}_y t_1\right)\cdot\left(\hat{I}_z\cos\omega_{B_1}t_1 + \hat{I}_y\sin\omega_{B_1}t_1\right)\cdot\exp\left(\mp \mathrm{i}\,\omega_{E_2}\hat{I}_y t_1\right). \quad (2.153)$$

Solving the two parts separately, first for the spin projection along the y-direction

$$\exp\left(\pm \mathrm{i}\,\omega_{E_2}\hat{I}_y t_1\right)\cdot\left(\hat{I}_y\sin\omega_{B_1}t_1\right)\cdot\exp\left(\mp \mathrm{i}\,\omega_{E_2}\hat{I}_y t_1\right), \quad (2.154)$$

since the self-commutation of an operator with itself is zero, the above equation simplifies to

$$= \hat{I}_y\sin\omega_{B_1}t_1. \quad (2.155)$$

On solving the second part of the equation

$$\exp\left(\pm \mathrm{i}\,\omega_{E_2}\hat{I}_y t_1\right)\cdot\left(\hat{I}_z\cos\omega_{B_1}t_1\right)\cdot\exp\left(\mp \mathrm{i}\,\omega_{E_2}\hat{I}_y t_1\right), \quad (2.156)$$

and using the BCH expansion [42], and simplifying the equation,

$$\hat{\rho}(t_1) = (\hat{I}_z\cos\omega_{E_2}t_1 \mp \hat{I}_x\sin\omega_{E_2}t_1)\cos\omega_{B_1}t_1 + \hat{I}_y,\sin\omega_{B_1}t_1. \quad (2.157)$$

Adding the two parts of the equations we get

$$\hat{\rho}(t_1) = (\hat{I}_z\cos\omega_{E_2}t_1 \mp \hat{I}_x\sin\omega_{E_2}t_1)\cos\omega_{B_1}t_1 + \hat{I}_y\sin\omega_{B_1}t_1. \quad (2.158)$$

Separating the projection operators

$$\hat{\rho}(t_1) = \hat{I}_z\cos\omega_{E_2}t_1\cos\omega_{B_1}t_1 \mp \hat{I}_x\sin\omega_{E_2}t_1\cos\omega_{B_1}t_1 + \hat{I}_y\sin\omega_{B_1}t_1. \quad (2.159)$$

Now during relaxation, the magnetisation precesses around the z-axis, which is represented by the Hamiltonian [38, 39]

$$\hat{H}_{\mathrm{FID}} = \Omega \hat{I}_z. \tag{2.160}$$

To find the density of states, we will solve each term of eq. (2.159) separately. For the first term, since the commutation $\hat{I}_z$ with $\hat{I}_z$ is zero, we get

$$\hat{I}_z \cos \omega_{E_2} t_1 \cos \omega_{B_1} t_1 . \tag{2.161}$$

Solving the second term,

$$\mp \sin \omega_{E_2} t_1 \cos \omega_{B_1} t_1 e^{-\mathrm{i}\Omega \hat{I}_z t_2} \hat{I}_x e^{\mathrm{i}\Omega \hat{I}_z t_2}, \tag{2.162}$$

which is similar to equation (2.117), therefore, on simplification

$$\mp \sin \omega_{E_2} t_1 \cos \omega_{B_1} t_1 (\hat{I}_x(\cos(\Omega t_2)) + \hat{I}_y(\sin(\Omega t_2))). \tag{2.163}$$

Finally, for the projection along the y-axis, we get

$$\sin \omega_{B_1} t_1 (e^{-\mathrm{i}\Omega \hat{I}_z t_2} \hat{I}_y e^{\mathrm{i}\Omega \hat{I}_z t_2}). \tag{2.164}$$

Expanding using the BCH formula [42], and simplifying the equation we get

$$\sin \omega_{B_1} t_1 (\hat{I}_y \cos \Omega t_2 - \hat{I}_x \sin \Omega t_2). \tag{2.165}$$

Adding back the terms from the solutions

$$\begin{aligned} \hat{\rho}(t_2) = {} & \sin \omega_{B_1} t_1 (\hat{I}_y \cos \Omega t_2 - \hat{I}_x \sin \Omega t_2) \\ & \mp \sin \omega_{E_2} t_1 \cos \omega_{B_1} t_1 (\hat{I}_x(\cos(\Omega t_2)) + \hat{I}_y(\sin(\Omega t_2))) \\ & + \hat{I}_z \cos \omega_{E_2} t_1 \cos \omega_{B_1} t_1 . \end{aligned} \tag{2.166}$$

Separating the projection operators, for the x,y and z directions, the equation simplifies to

$$\begin{aligned}\hat{\rho}(t_2) =& \hat{I}_y(\sin(\omega_{B_1}t_1)\cos(\Omega t_2) \mp \sin(\omega_{E_2}t_1)\cos(\omega_{B_1}t_1)\sin(\Omega t_2)) \\ &- \hat{I}_x(\sin(\omega_{B_1}t_1)\sin(\Omega t_2) \pm \sin\omega_{E_2}t_1\cos\omega_{B_1}t_1\cos(\Omega t_2) \\ &+ \hat{I}_z\cos\omega_{E_2}t_1\cos\omega_{B_1}t_1.\end{aligned} \tag{2.167}$$

To estimate the observable of the signal, we would need to take the trace of the density matrix with respect to the $\hat{I}^+$ operator, as the spins are rotating in the x-y plane, i.e., [38, 39]

$$\langle \mathrm{FID}_{\mathrm{Chiral}} \rangle = \mathrm{Tr}\left\{\hat{I}^+\hat{\rho}(t_2)\right\}. \tag{2.168}$$

Therefore,

$$\begin{aligned}\mathrm{Tr}\left\{\hat{I}^+\hat{\rho}(t_2)\right\} =& (\hat{I}_y(\sin(\omega_{B_1}t_1)\cos(\Omega t_2) \mp \sin(\omega_{E_2}t_1)\cos(\omega_{B_1}t_1)\sin(\Omega t_2)) \\ &- \hat{I}_x(\sin(\omega_{B_1}t_1)\sin(\Omega t_2) \pm \sin\omega_{E_2}t_1\cos\omega_{B_1}t_1\cos(\Omega t_2) \\ &+ \hat{I}_z\cos\omega_{E_2}t_1\cos\omega_{B_1}t_1)(\hat{I}_x + \mathrm{i}\hat{I}_y).\end{aligned} \tag{2.169}$$

Using the same property as before, i.e., the trace of an operator with another operator will lead to zero, therefore, the equation simplifies to

$$\begin{aligned}\mathrm{Tr}\left\{\hat{I}^+\hat{\rho}(t_2)\right\} =& \frac{\hbar^2}{4}(\mathrm{i}(\sin(\omega_{B_1}t_1)\cos(\Omega t_2) \mp \sin(\omega_{E_2}t_1)\cos(\omega_{B_1}t_1)\sin(\Omega t_2)) \\ &- \sin(\omega_{B_1}t_1)\sin(\Omega t_2) \mp \sin\omega_{E_2}t_1\cos\omega_{B_1}t_1\cos(\Omega t_2)).\end{aligned} \tag{2.170}$$

Separating the chiral terms from the non-chiral terms, the rearrangement of the equation is,

$$\begin{aligned}\mathrm{Tr}\left\{\hat{I}^+\hat{\rho}(t_2)\right\} =& \frac{\hbar^2}{4}((\sin(\omega_{B_1}t_1)(\mathrm{i}\cos(\Omega t_2) - \sin(\Omega t_2)) \\ &\mp \sin(\omega_{E_2}t_1)(\cos(\omega_{B_1}t_1)(\mathrm{i}\sin(\Omega t_2) + \cos(\Omega t_2)).\end{aligned} \tag{2.171}$$

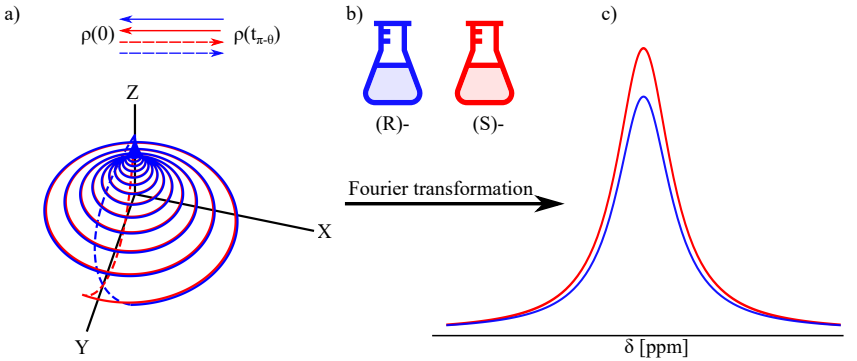

Figure 2.7: (a) Represents a situation in an enantiopure chiral molecule, when an RF-pulse applied is such that it flips the net magnetisation close to π. The relaxation of the (R)- and the (S)- enantiomer magnetisation will follow a different path to the equilibrium state. (b) (R)-enantiomer is represented by blue, and the (S)-enantiomer by red. (c) Fourier transformation for a signal from the enantiomer pairs will have a magnitude difference.

From the equation above, it can be seen that the chiral signal is projected only along the x-direction. Therefore, to be able to distinguish a chiral molecule it is necessary to have a receiver coil, which is sensitive to the magnetic fields in the x-direction.

If we now consider the design of the chiral exciter/detector, it needs to have certain characteristics, which are, that the E_2 which is responsible for the spin excitation should be perpendicular to the B_0. If we assume that the B_0 is in the z-direction, and the E_2 is in the y-direction, then a detector should be sensitive in the x-direction. The design of the detectors based on the scenarios derived is discussed in more detail in the next chapter.

2.2.4 Net magnetisation flipped by $\pi/2$

If the RF pulse duration is such that it produces a $\pi/2$ flipping of the net magnetisation, then the magnetic nutation frequency and the pulse duration can be related as

$$\omega_{B_1} t_1 = \pi/2, \tag{2.172}$$

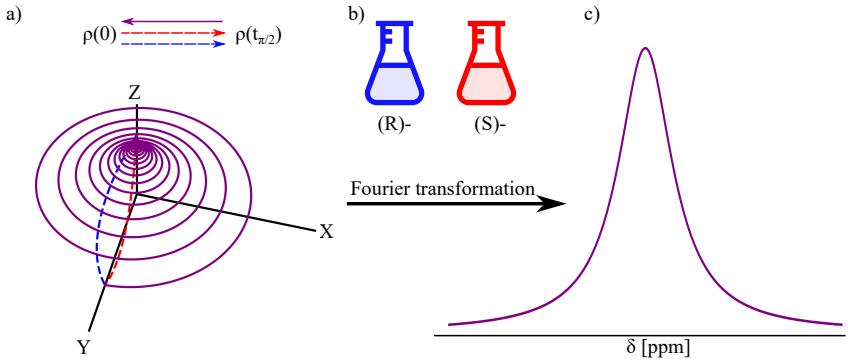

Figure 2.8: (a) Represents a situation, when an $\pi/2$ RF-pulse is applied to an enantiopure chiral molecule. For the (R) and the (S) enantiomers, the FID is exactly same. b) (R)-enantiomer is represented by blue, and the (S)-enantiomer by red. (c) Therefore, a Fourier transform for a signal from enantiomer pairs is equal and no distinction is observed.

which, when used in equation (2.152) simplifies to

$$\hat{\rho}(t_1) = \exp\left(\pm i\,\omega_{E_2}\hat{I}_y t_1\right)(\hat{I}_y)\exp\left(\mp i\,\omega_{E_2}\hat{I}_y t_1\right). \tag{2.173}$$

Since the Commutation of the operator with itself results in zero, using the BCH expansion [42] and the simplification is

$$\hat{\rho}(t_1) = \hat{I}_y. \tag{2.174}$$

As can be seen from the solution of the equation, the chiral term in this case vanishes and the signal for the two enantiomers will be indistinguishable. In such a scenario, if a spectroscopist excites the spins such that B_1 part of the RF perturbation flips the magnetisation by $\pi/2$, then the observed chiral signal will be non-existent.

2.2.5 Net magnetisation flipped by π

Another scenario can be that the net magnetisation is flipped by π, i.e., in the opposite direction with respect to the B_0. Therefore, the spin alignment from the initial state will be reserved. For this particular case, the magnetic nutation frequency and the pulse duration can be related as

$$\omega_{B_1} t_1 = \pi, \tag{2.175}$$

and the equation (2.152) simplifies to

$$\exp\left(\pm \mathrm{i}\,\omega_{E_2} \hat{I}_y t_1\right) \cdot \hat{I}_z \cos\omega_{B_1} t_1 \cdot \exp\left(\mp \mathrm{i}\,\omega_{E_2} \hat{I}_y t_1\right). \tag{2.176}$$

. Solving the above equation using the BCH expansion [42] and the simplification is

$$\hat{\rho}(t_1) = -(\hat{I}_z \cos\omega_{E_2} t_1 \mp \hat{I}_x \sin\omega_{E_2} t_1). \tag{2.177}$$

Therefore, the density function now contains a chiral distinction term which is opposite in the sense for an enantiomeric pair.

If we look at the above equation, it is similar to transforming the density of states from the initial condition if the B_1 was neglected. The spin evolution for these two cases is similar, i.e., the case where the magnetic fields are neglected and when the net magnetisation is flipped by π due to magnetic perturbation. The evolution of the density operator can be considered under single derivation.

After the RF perturbation, the spins relax from the excited state to the ground state. This is followed by a precession around the z-axis. Therefore, the Hamiltonian for spins in precession is

$$\hat{H}_{\mathrm{FID}} = \Omega \hat{I}_z, \tag{2.178}$$

and hence the evolution of the density operator is

$$\hat{\rho}(t_2) = \exp\left(-\mathrm{i}\Omega \hat{I}_z t_2\right)\left(-\hat{I}_z \cos\omega_{E_2} t_1 \pm \hat{I}_x \sin\omega_{E_2} t_1\right) \exp\left(\mathrm{i}\Omega \hat{I}_z t_2\right). \tag{2.179}$$

Since the commutation of an operator with itself is zero, therefore, the term with the projection operator along the z-axis remains unaffected. For the projection along the x-direction, the equation can be simplified using the BCH expansion [42], similar to equation (2.117),

$$\hat{\rho}(t_2) = -\hat{I}_z \cos\omega_{E_2} t_1 \pm \sin\omega_{E_2} t_1 (\hat{I}_x \cos(\Omega t_2) + \hat{I}_y \sin(\Omega t_2)). \tag{2.180}$$

Now since the magnetisation is precessing in the x-y plane, therefore, to measure the signal we need to find the trace of the density matrix with respect to the $\hat{I}^+$, i.e.,

$$\langle\overline{\text{FID}}\rangle_{\text{chiral}} = \text{Tr}\left\{\hat{I}^+ \hat{\rho}(t_2)\right\}, \tag{2.181}$$

where,

$$\hat{I}^+ = \hat{I}_x + \text{i}\hat{I}_y. \tag{2.182}$$

Therefore,

$$\begin{aligned}\text{Tr}\left\{\hat{I}^+ \hat{\rho}(t_2)\right\} = \text{Tr}\{-\hat{I}_z \cos\omega_{E_2} t_1 \pm \sin(\omega_{E_2} t_1) \\ (\hat{I}_x(\cos(\Omega t_2)) + \hat{I}_y(\sin(\Omega t_2)))(\hat{I}_x + \text{i}\hat{I}_y)\}.\end{aligned} \tag{2.183}$$

The equation can be simplified using the property, that the trace of an operator with a different operator (in this case here), is zero. Therefore, the simplified equation is

$$\text{Tr}\left\{\hat{I}^+ \hat{\rho}(t_2)\right\} = \pm\sin(\omega_{E_2} t_1)(\frac{\hbar^2}{4})(\cos\Omega t_2 + \text{i}\sin\Omega t_2), \tag{2.184}$$

or,

$$\text{Tr}\left\{\hat{I}^+ \hat{\rho}(t_2)\right\} = \pm\sin(\omega_{E_2} t_1)(\frac{\hbar^2}{4})\exp(\text{i}\Omega t_2). \tag{2.185}$$

Therefore, if one compares the FID for the NMR and chiral NMR process, the additional term, i.e., $\sin(\omega_{E_2} t_1)$ defines the strength of the chiral signal that can be acquired. Since the analogous electrical nutation frequency will be in an opposite sense for the enantiomeric pairs, the magnetisation will be flipped to the

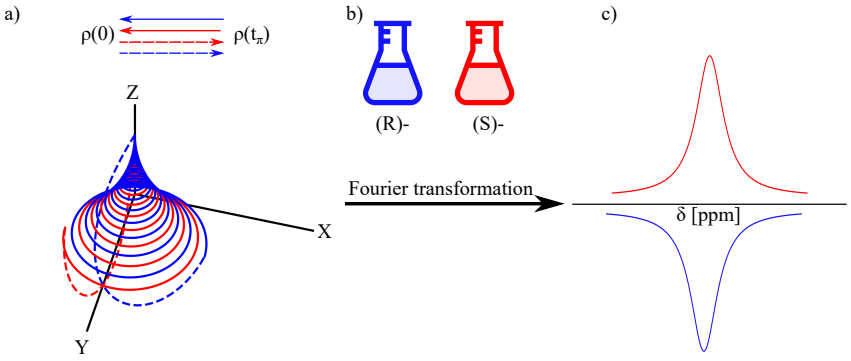

Figure 2.9: (a) Represents a situation, when an exact π RF-pulse applied to an enantiopure chiral molecule. The relaxation of the (R)- and the (S)- enantiomer spins is in a different quadrant. b) (R)-enantiomer is represented by blue, and the (S)-enantiomer by red. (c) Therefore, a Fourier transform for a signal from enantiomer pairs is going to be opposite in phase and equal in magnitude.

x-y plane, but in different quadratures. Hence, the precession of the two chiral molecules will be exactly π out of phase with each other.

From the above derivations, it can be seen that the strength of the chiral signal will depend on the magnitude of the E_2, B_0, γ_r, and the RF pulse duration. However, there is a limit up to which the magnitude of E_2 can be used, which is limited by the dielectric breakdown of the surrounding materials, as well as, that of the sample. By increasing the RF pulse duration the chiral signal can be enhanced, but the duration time will be limited by the spin transverse relaxation time. Increasing the amplitude of B_0 after a certain value also has its drawback, which is explained in chapter 3. The dependence of the chiral strength on the γ_r, suggests that the chiral centre should be around a nucleus with a higher γ_r. The choice of suitable molecule is explained in chapter 4

3 NMR chiral signal exciter and receiver

In the previous chapter, it was shown that three possible scenarios can occur when exciting the spins using E_2 and B_1. It was shown that, when the B_1 perturbation produces a $\pi/2$-flip, the chiral signal was not distinguishable and was the same for an enantiomer pair. However, if the magnetisation is flipped by π or the B_1 perturbation is negligible, the chiral signal detection probability is higher. As it was difficult to produce an exact π-flip due to stray fields, another case, where the magnetisation was flipped at an arbitrary angle with respect to the B_0. In all of these cases, there was a need to design a chiral detector which could produce an E_2 and simultaneously be sensitive to the magnetisation detection.
Since the chiral signal is embedded in the magnetisation projected along the x-direction. The E_2 needs to be produced along the y-direction, and finally, these two should be perpendicular to B_0 in the z-direction. Therefore, B_1, E_2, and B_0 should be orthogonal to each other.
In this chapter, we explore the current state of the art for direct chiral detection, and based on the scenarios discussed in chapter 2, optimise and design a suitable chiral exciter and detector geometry. Since the functioning of the detectors was based on the RF pulse, therefore, we need to understand the behaviour of the EM-waves for a suitable geometry.

3.1 Electromagnetic waves description based on Maxwell's equations

EM-waves is an inherent part of NMR [38]. Since the alignment of the magnetisation, and its detection during relaxation depends on the magnetic perturbation in the frequency range of MHz. The magnetic field propagation at this frequency

range is governed by Maxwell's equation. Depending upon the strength of B_0, the ω_0 can be calculated using eq. (2.45). Table 3.1, shows different values of $\omega_0/2\pi$ corresponding to B_0 amplitudes for ^{1}H. At present, for the commercially

Table 3.1: Corresponding values of $\omega_0/2\pi$ for ^{1}H at different B_0 magnitude [38].

$\omega_0/2\pi$ (MHz)	42.577	300	500	600
B_0 (T)	1	7.05	11.74	14.09

available spectrometers ω_0 lies in the RF range.

Therefore, if a a device is built that can transmit EM-waves, and be sensitive to them at the desired frequency; this will allow to excite the magnetisation and detect the signal during their relaxation.

Since EM-waves consist of electric and magnetic fields, the relationship between them can be defined using Maxwell's equations. These are:

Gauss' law,

$$\nabla \cdot \varepsilon_0 \varepsilon_r \vec{E} = \rho. \tag{3.1}$$

Gauss' law for magnetism

$$\nabla \cdot \vec{B} = 0. \tag{3.2}$$

Faraday's law of induction

$$\nabla \times \vec{E} = -\frac{\partial \vec{B}}{\partial t}. \tag{3.3}$$

Ampere's law

$$\nabla \times \vec{B} = \mu_0 \mu_r \left(\vec{J} + \varepsilon_0 \varepsilon_r \frac{\partial \vec{E}}{\partial t} \right). \tag{3.4}$$

Of these four equations, the most relevant to the NMR process are eq. (3.3), and (3.4), i.e., Ampere's law, and Faraday's law.

During the irradiation process, we use the principle behind Ampere's law, i.e., the current flowing along a conductor produces a magnetic field. The direction of the magnetic field will follow a circular loop, which is normal to the direction of current flow. Since, the net magnetic field is the superimposition of the mag-

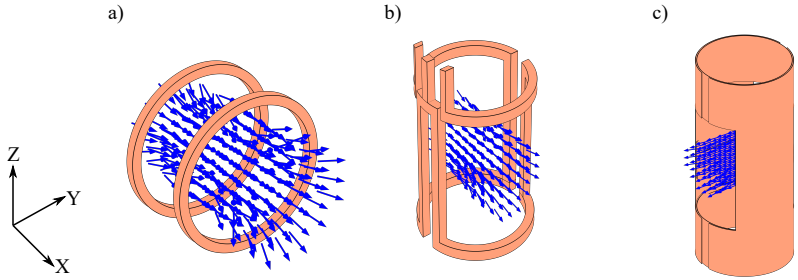

Figure 3.1: Few examples of volumetric detectors used in NMR and the direction of the magnetic field produced shown with blue arrows. (a) A 15 mm Helmholtz coil arrangement [47]. (b) A 12 mm diameter saddle coil with a detection height of 15 mm [48]. (c) A 12 mm diameter Aldermann-Grant coil with a detection height of 9 mm [49].

netic fields produced by the conductive parts, by finding an appropriate path for the current flow or the shape of the conductor, the magnetic fields can be made unidirectional. This is one of the basic requirements for the transmitter coil used in the NMR. Figure 3.1, shows some examples of coils used for NMR.

The second phase of the NMR involves the detection of energy released when the magnetisation relaxes to its ground state. The design of the detector is based on the principle of Faraday's law of induction. This is explained as, when there is a change in a magnetic field (produced due to precession and transverse relaxation of the magnetisation) experienced by a closed-loop conductor, there is voltage induced in it. The magnitude of the voltage produced is proportional to the rate of change of the magnetic flux in the conductor, and the direction of the voltage produced is to oppose the change in the magnetic flux. Therefore, if spins precess at ω_0, the voltage produced also oscillates at ω_0, and hence by measuring the voltage one can acquire the NMR signal [38]. Though this is a simple explanation of the process, for the enhancement of the signal strength and its quality, different circuit techniques and instruments are used. The fig. 3.2 is a representation of such an arrangement.

Similar to the transmission coil, the receiver coil is geometrically designed to acquire a signal from a uni-directional, magnetic field. In principle, one can use

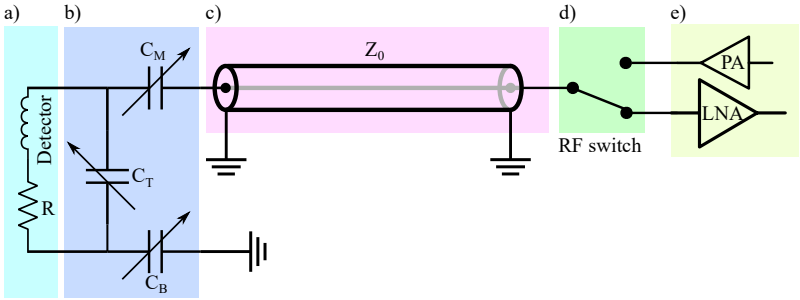

Figure 3.2: Electrical circuit schematic of an NMR excitation and detection scheme [50]. (a) A transceiver coil is placed near the sample under investigation. (b) The capacitor circuit arrangement is connected to the coil to tune the coil to the desired ω_0 using C_T, and C_M to match the impedance of the coil to 50 Ω. C_B is used to balance the electrical length of the coil at ω_0. (c) The detector and tuning-matching circuit is connected to the single pole double throw RF-switch via a transmission line. (d) The RF-switch is used to switch between the power amplifier (PA) and low-noise amplifier (LNA). (e) At the control of the spectrometer the RF-switch switches between the PA during the excitation phase, and to the LNA during signal acquisition.

a single coil for transmission as well as detection of the signal. This is achieved by switching between the transmission and receiver circuit using appropriate RF switches [50] as shown in fig. 3.2. In general, Maxwell's equation follows the reciprocity principle, i.e., the two processes are reciprocal to each other. Therefore, the electric field produces the desired magnetic field to flip the magnetisation, and the magnetic field radiated by the spins is detected as a voltage signal by the coil. As discussed in chapter 2, the NMR process can be defined in three phases; the initial or equilibrium phase, the excitation phase and finally the detection phase. If the excitation and the detection phases are performed sequentially, then the coil can be used for transmission as well as for receiving the signal.

From the above discussion, it was shown how to direct the magnetic fields based on the electrical path of the currents. For the chiral NMR measurements we have three dependants that affect the signal, which are E_2, B_1 and B_0. Based on this, the experimental and the current state of the art described from the literature are explained, and as to why they were not used for the detection. Following

this, the designs of the chiral detectors and their shortcomings before reaching a successful detector design are described.

3.2 Direct NMR chiral distinction methods proposed in the literature

At present, there are no successful methods proposed for direct chiral signal detection using NMR; however, there were some methods ideas, which could have led to chiral detection, and are discussed below.

The first method was proposed by [14], which was, after applying a $\pi/2$ pulse, if the setup is designed in a way such that the sample is placed between two metal plates, then these metal plates would detect a signal from electric polarisation due to their precession. The precession of the electric dipole would be opposite in sense for enantiomers. One particular problem in this setup would have been that the chirality constant is of a lower order of magnitude, i.e., in the range of $1 \times 10^{-15}\,\mathrm{V\,m^{-1}}$ [46, 51]; therefore, the detection of the electric polarisation might be difficult.

To overcome this problem, it was proposed by [45], that instead of detecting electric polarisation after the application of $\pi/2$ pulse, another way could be to excite the electric dipole using E_2. Since, electric dipole and magnetic moment, are coupled to each other in a chiral molecule, it will induce the flipping of the magnetisation, and then by detecting the magnetisation during their relaxation, we would detect a chiral signal.

One of the advantages of this process was that using an E_2 oscillating at ω_0 instead of a DC field could enhance the chiral signal by a factor of $10^6 - 10^8$ [45]. However, using a RF field instead of a DC field comes with its challenges. As can be seen from eq. (3.4), the rate of change of electric field with respect to time, produces a magnetic field. The amplitude of the magnetic field produced directly depends on the frequency of the oscillation. Therefore, the higher ω_0 is, the higher is the amplitude of the magnetic fields. As explained in chapter 2, the magnetic field perturbations are a source of noise for a chiral signal and need

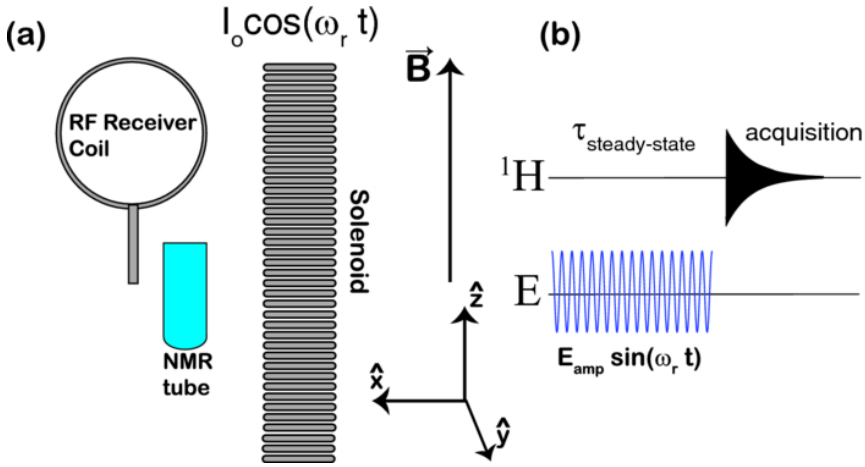

Figure 3.3: One of the first proposed experimental setups with oscillating electric fields was recommended to be used for chiral detection. (a) Shows a solenoid coil, which was to be used for the E_2 source. The B_1 produced from the solenoid was directed towards B_0. A receiver coil was to be placed next to the sample, which would detect the magnetic dipole altercations. (b) Proposed pulse sequence for the setup in (a), assuming that there were no stray magnetic fields produced from the solenoid coil in the transverse plane. (Reprinted from [45] fig.1, with the permission of AIP Publishing).

to be suppressed to be able to observe the chiral signal. This limits the strength of B_0 in which a sample can be placed, as with increasing field strengths the ω_0 increases. Hence, there is a trade-off between the B_0 strengths, and the amount of spin polarisation required.

One approach was, instead of suppressing the magnetic fields, to design the current path in a way that they are in the direction of B_0. Since the B_1 when operated by $\hat{I}_z$ operator doesn't contribute to an NMR signal [38, 39]. In this situation, one can simply ignore their effect on the evolution the magnetisation.

Based on this idea, there was a setup proposed by [45] as shown in fig. 3.3, where it was shown that instead of suppressing the magnetic fields associated with oscillating electric fields, one could design the exciter in such a way that the magnetic fields are aligned along the direction of the B_0. Hence, the effect of stray B_1 could be neglected.

Nevertheless, one of the shortcomings of this design was that the amplitude of the E_2 produced is lower. As shown in eq. (2.133) the strength of the chiral signal depends on the amplitude of the E_2, therefore the exciter would not have performed efficiently.
Another drawback of this design was that the resonator used for excitation would have been different than a receiver coil. Since the sample would have been enclosed by a detection coil it would be difficult to place or position an excitation coil.
Another issue was that since the metal acts as a reflector for the magnetic fields, which can be explained by the boundary conditions equations,

$$\vec{n} \cdot \vec{B}_A = \vec{n} \cdot \vec{B}_B = 0, \tag{3.5}$$

$$\vec{n} \times \vec{B}_A = \vec{n} \times \vec{B}_B, \tag{3.6}$$

$$\vec{n} \cdot \vec{E}_A = \vec{n} \cdot \vec{E}_B, \tag{3.7}$$

and

$$\vec{n} \times \vec{E}_A = \vec{n} \times \vec{E}_B = 0. \tag{3.8}$$

where, $\vec{n}$, is the normal vector between material A and material B as shown in fig. 3.4 [52]. These equations hold for a perfect conductor boundary where the electric field parallel to the boundary is zero; therefore, by Faraday's law, the time-dependent magnetic field outside the metal boundary will be zero [52]. If we assume the metal used is copper and not perfectly conductive, i.e., has finite conductivity then the magnetic field picked up by the receiver coil will be attenuated [53]. Another challenge was the formation of eddy currents due to oscillating fields in the two conductors. Though the eddy currents eventually decay and the signal could be recorded after a delay, this would have led to the loss of coherence for the chiral signal [38]. As the magnetic moment produced due to a chiral signal is already weak, the setup would not have been ideal for the measurement of the chiral signals.

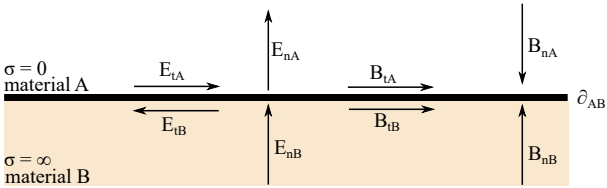

Figure 3.4: EM-wave boundary condition on a perfect electric conductor [52].

Based on the design proposed by [45], there was an improvement by [54], as shown in fig 3.5. The design was based on a ring loop resonator, where the detector has a capacitor plate and conductive ring loop surrounding it in either direction to maintain symmetry. The reason for including the loop was that the displacement current, flowing through the copper, has a conductive path that produces a magnetic field between the capacitor plates. The superposition of the magnetic fields between the capacitor plates, and that produced by the ring, was such that it directs the magnetic fields in the B_0's direction. This arrangement produces a region asteroidea shape, which is the chiral-sensitive area, where E_2 is more dominant than the B_1 in the x-y plane. The chiral-sensitive region's boundary was limited by the equation

$$k = \frac{c\sqrt{\vec{B}_x^2 + \vec{B}_y^2}}{\sqrt{\vec{E}_x^2 + \vec{E}_y^2}} \tag{3.9}$$

where c is the speed of light in vacuum, $\vec{E}$ and $\vec{B}$, represent the electric field and the magnetic field, respectively, in their respective directions [46, 54]. The unit less factor k defined the chiral sensitive region, where the chiral signal could be expected for volumes where $k < 10^{-4}$ [46, 54].

The limiting value of k was calculated from the chiral NMR Hamiltonian. To find this value it was assumed by [46,54] if the normal NMR signal generated and the chiral NMR signal generated are equal then

$$k_N = c\,|\sigma_c|\,B_0, \tag{3.10}$$

This value was calculated to be $\approx 10^{-4}$ in [54] for 1,1,1-trifluoropropan-2-ol.
Though a promising setup, the resonator had its challenges which made the detection of the chiral signal difficult. The challenges were acknowledged by the authors, which were: dielectric heating, alignment of the resonator, shimming the small sample volume (in µl) below a Hz, and permittivity inhomogeneity.
Of all the problems mentioned above the permittivity inhomogeneity was the biggest issue since the asteroidea shape produced by the resonator was sensitive to any permittivity changes. A difference of 1%, between the dielectric constant of the material, would have reduced the chiral-sensitive region [54].
This produces two major roadblocks: first, the sample concealment, which should have a similar dielectric constant to the container, and second, the introduction of a sensor to detect the magnetisation.
Since the detector cannot be introduced between the parallel plates for the reason stated above, one option could be to transport the sample between the resonator and the detector. However, the detector could not be placed close to the resonator due to its size and limited B_0 homogeneity region (around 3 cm). The length of the resonator was 7 cm, therefore, one option was to use two spectrometers or magnets to transfer the samples. This would have had its limitation since the chiral signal is weak, which meant fast sample shuttling time.
The alignment of the resonator was also important since it was reported that even a tilt of 0.1°, reduces the signal by 10%. Though not a major issue it could still create problems in the detection of enantiomers, where the chiral coupling tensor is weak.
And final biggest challenge considering all the points mentioned above was the application of the E_2. Since there were no ports for RF excitation, it was not

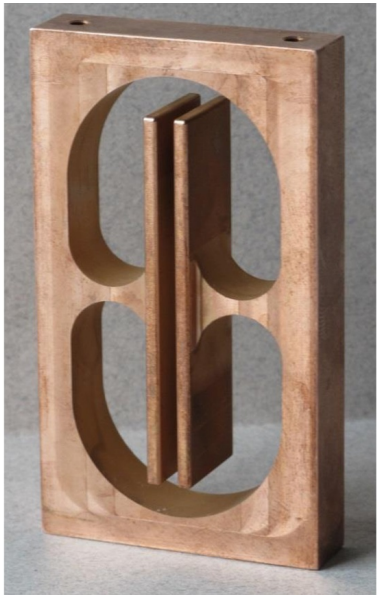

Figure 3.5: Ring loop resonator design developed by [54], where the function of the resonator was to maintain a high magnitude E_2 while reducing the stray magnetic fields produced. The dimension of the resonator in length and width was 70 mm by 40 mm respectively. (Reprinted from [54] fig. 5(A), with the permission of AIP Publishing).

reported by the authors on how this would be achieved. If one assumes that an antenna which couples with the ring loop of the detector could be used for excitation, this would require, a high current flowing through the antenna, to achieve the target fields in the range of $\mathrm{kV\,m^{-1}}$.
To overcome the challenges discussed in the two present states of art, the improvement of the detector designed in this dissertation is discussed further.

3.3 Miniaturised ring loop resonator

In section 3.2, it was discussed that one of the issues was to place a detector inside the chiral sensitive region, as it disturbed the asteroidea shape. To overcome this

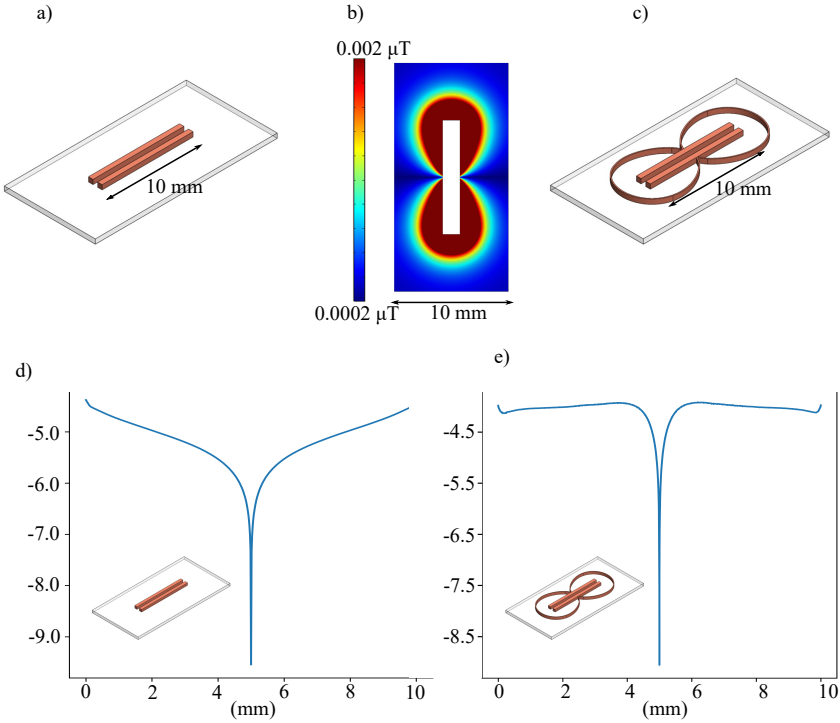

Figure 3.6: (a) Two conductors arranged as a parallel plate capacitor used to define the capacitor geometry. The length of the capacitor plate is 10 mm, and the distance between them is 0.5 mm. The capacitor plates are placed on a glass substrate, so that the dimension of the glass substrate could fit in a 10 mm saddle coil. (b) Magnetic field generated around the metal plates. The contour produced at a field value of 0.0018 µT was used to define the geometry of the compensating loop. (c) The ring loop resonator defining the compensating field. The lower inserts (d) and (e) show a comparison of the profile of the *k*-value, d) with and e) without the compensating conductive loop.

problem, a miniaturised ring loop resonator was designed such that the resonator could be placed inside the detector.

To design such a resonator, two metal plates were placed parallel to each other to produce electric fields, i.e., they act as a capacitor. The geometry of the design was as shown in the fig 3.6 (a). The length of the plates was set to 10 mm, based

on the sensitive region of interest of a commercially available Bruker's 10 mm saddle coil. The metal plates were separated by a distance of 0.5 mm.
The resonator aimed to have a uniform *k*-value distribution given by the eq. (3.9). The reason was to increase the sensitive volume, which would have led to enhancement of the chiral signal generated.
To design the *k*-value compensating conductive loops similar to as shown in fig 3.5, the first step was to excite the metal plates such that they had an electric field present between them. This was achieved by setting a source of electric field at the metal boundaries. As the metal feature size was much greater than the skin depth of copper at 470 MHz, the boundaries of the metal domains were truncated using the impedance boundary condition. The impedance boundary condition and the setting of a source of electric field was defined as

$$\frac{1}{\sqrt{\mu(\varepsilon+\frac{\sigma}{i\omega})}}\vec{n}\times\vec{B}+\vec{E}-\left(\vec{n}\cdot\vec{E}\right)\vec{n}=\begin{cases}(\vec{n}\cdot E_y)\,\vec{n}-E_y \text{ on } \partial\Omega_{M1},\\ 0 \text{ on } \partial\Omega_M-\partial\Omega_{M1}.\end{cases} \tag{3.11}$$

The source field on the boundary $\partial\Omega_{M1}$, was set to $1\,\mathrm{MV\,m^{-1}}$ [55].
The electric fields were then used to compute the magnetic fields surrounding the metallic boundaries. The magnetic field value at the boundary of the red domain (0.0018 µT) was used to set as the boundary for the placement, and shape of the compensating loop.
The working principle behind the design was that the metal tracks placed around the capacitor would have a current induced in them from the capacitor plates' stray magnetic field. This current induced will produce a magnetic field distribution between the capacitor plates. Since the position of the loops is located where the magnetic fields are produced by the capacitor, this would help to compensate the magnetic fields between the plates and homogenise *k*-value distribution. Figure 3.6 (d) and (e) compare the *k*-value distribution for the two cases.
The final *k*-value is uniform compared to without the loops due to the magnetic field components added from the loops.

This was the first design approach, which was abandoned. Since the coupling of the energy into the resonator, would require high powers.
A possible solution could be to connect the capacitor from the side via an RF port rather than exciting with a coupling antenna. This approach would produce a curl of the magnetic field between the plates governed by eq. (3.4). To compensate magnetic fields in such a case we would require, 3-D arrangement such that loops protrude outside the plan of paper, which in itself will be difficult to fabricate for geometries with small dimensions. However, this is something achievable with larger dimensions which led to the second resonator design, which overcomes these limitations, i.e., excitation of the ring resonator, and compensation of the magnetic field between the metal.

3.4 Active ring loop resonator

In the above section, the approach to fitting a chiral-sensitive resonator inside a detector was discussed. However, one of the challenges was to excite the resonator such that the parallel plates could have an electric field between them. Since coupling the energy to excite the resonator was not an efficient approach, to overcome this issue an active RF port was included, which could produce the same behaviour as discussed in [54], and at the same time could be excited using an RF source. In this section, we discuss how the design was achieved and its limitations.
In this resonator design the rectangular metal plates were replaced with the circular parallel plates as shown in fig 3.7 (a). The circular plates were connected through a current feeding wire at its centre. The reason for making the plates circular was to allow smooth distribution of the currents on the plates as shown in fig 3.7 (b), which produces a symmetric distribution of the current on the surface. If we now look inside the capacitor, between the metal plates, there is an electric field, which can be represented by a displacement current density J_D such that,

$$J_D = \varepsilon_0 \varepsilon_r \frac{\partial \vec{E}}{\partial t}. \tag{3.12}$$

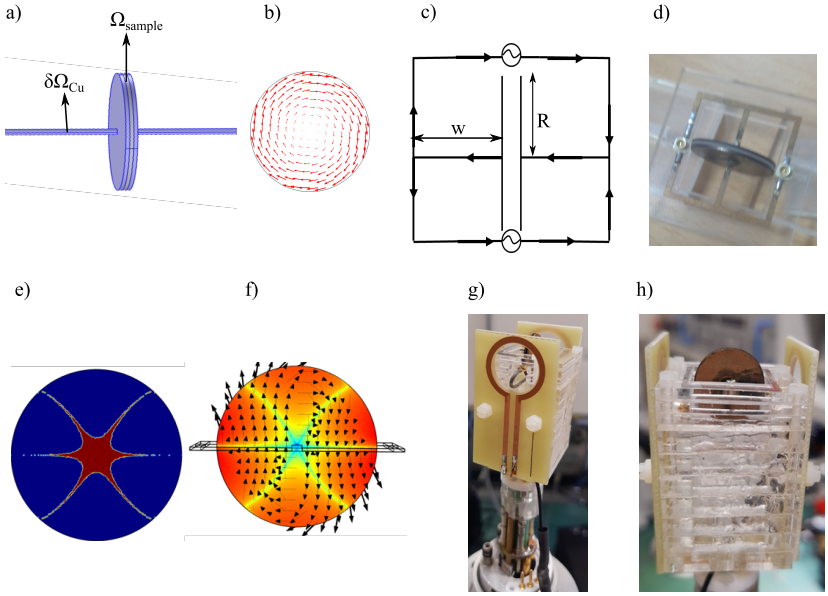

Figure 3.7: (a) Shows a circular plate capacitor, where the sample is placed between the metal plates. Two wire extending from the circular metal disk is used as a feed line for RF excitation. (b) When the circular disks are excited they produce a magnetic field between the metal plates. The direction of the magnetic field produced depends upon the direction of the electric fields (displacement current), which is the curl of the electric field direction. (c) Since the magnetic field in the B_0 direction can be neglected, and the field in the x-y plane is the noise for the chiral signal, it needs to be minimised. This is done by placing a conductive loop around the circular disk, where the parameters w and R affect the magnetic field compensation. The RF ports are placed on either side to uniformise the field distribution. (d) Shows the final fabricated active ring loop resonator, where the loop is excited using a U.FL RF connector. (e) Is the boundary of k-value produced for regions where $k < 10^{-4}$ in red. (f) Shows the magnetic field direction produced by the compensating loops. The field direction around the detection zone is in the B_0 direction. (g) The NMR coil used for the magnetic dipole detection is mounted on a probe head. (h) The side-view of the setup showing the ring-loop resonator placed between the coil. The dimension of the ring-loop resonator fabricated, and its feature shown in this figure is taken from the highlighted row of table 3.2

Therefore, the capacitor plates are analogous to a large wire carrying a current. From Ampere's law, we know that a straight current-carrying wire has a magnetic field, where the vector is given as the curl in the direction of current flow as shown

in eq (3.4). Therefore, for an electric field in the y-direction, the magnetic field will be along the x- and, z-direction.

From the previous discussion, orienting B_1 along B_0 helps in the detection of the chiral signal. Therefore, aligning the magnetic fields inside the capacitor such that the component along the x-direction is cancelled and the effective field is along the z-direction can improve chiral NMR detection.

This effect was achieved by placing two parallel wires such that the current flowing along them is in the opposite direction as the displacement current. Figure 3.7 (c) shows the effect of parallel current wires and the direction of the current. Using the same principle, the goal was to minimise the x-component of the magnetic fields.

The computation was setup with the geometric dimensions shown in fig 3.7 (c), where the distance between the plates and the wire was swept to find the best suitable conditions for chiral detection. The optimal geometric conditions were chosen such that, it is the one which produces an asteroidea-shaped k-value distribution, and fulfils the condition set in eq. (3.9). Table 3.2 summarises the outcome of the computational results

Table 3.2: Comparison of different parameters for the active ring loop resonator. The highlighted row represents the optimised geometry, where the averaged k-value was the lowest, and the detection volume the highest.

Plate radius mm	Distance between the circular plates and the wires mm	averaged k-value (in a volume)
2.5	3.97	-5.5 (0.56 mm^3)
5.0	6.57	-6.0 (1.57 mm^3)
8.0	9.66	-7.0 (4.0 mm^3)
10.0	11.57	-7.4 (3.53 mm^3)

From the above results, the capacitor plates with the radius 8.0 mm were selected, as they had the features desired for chirality detection, which was uniform k-value in a larger volume.

The metal plates were fabricated using an Ultraviolet (UV) laser source (Pirahna, ACSYS GmbH). The parameters for the laser cutting procedure are discussed in Appendix A.1.

The sample holder was fabricated from 500 µm borosilicate glass (Mempax, Schott AG) and was cut using the UV laser source (Pirahna, ACSYS GmbH). The parameters of the UV laser and the dimensions of the parts used for the detectors assembly are detailed in Appendix A.1 and A.2 respectively.

The coil as shown in fig. 3.7 (d), was fabricated on FR4 substrate. It was tuned to 500 MHz, and matched to 50 Ω. To test the sensitivity of the coil a ^{1}H spectroscopy with water was performed. An NMR signal could not be observed. Possible reasons for the failure of the device were:

- As was shown by [56], the NMR signal depends upon the projection of the magnetic field on the sample region (or the filling). In this case, the filling factor was quite low. The effective volume of the sample sensitive to magnetic field excitation was mm^3
- The reduction in effective sample volume followed by the sample surrounded by the metallic walls, further reduced the sensitivity of the magnetic detection of the setup. As was discussed in section 3.2, the metal boundaries act as magnetic insulation.

Therefore, to overcome the above two limitations it was important to have a larger volume with sufficient filling factor, which is not affected by the orientation of the magnetic and electric fields. The magnetic detection of the detector should be sensitive enough to detect a weak chiral signal. This led to the invention of the micro-stripline-based transceiver chiral detector, which could achieve the above-mentioned shortcomings.

3.5 Chiral sensitive transciever

So far the resonator designs discussed were based on a separate excitation and detection method. As shown in fig 3.1, there are several possibilities to design an NMR detector. From the shortcomings of the above design approach, the requirements for a chiral-sensitive transceiver can be listed as

- The E_2 produced should be perpendicular to the B_0.
- The detector should be sensitive to spins' detection in the direction orthogonal to E_2, and B_0.
- The metal plates should be placed as close to each other since the amplitude of E_2 required is large.
- The device should be able to tuned and matched to improve the signal-to-noise ratio (SNR) of the signal.
- The detector should have sufficient sample volume to increase the number of spins which would improve the probability of detecting the chiral signal.
- The magnetic field detection, and electric field detection part should be in the same region where the sample is placed to accommodate the detector in the bore of the spectrometer and position the sample at its iso-centre.
- Fabrication ease of the detector itself. Which should be easy to reproduce to maintain proper alignment between the E_2, B_1 and B_0.

From these requirements, an obvious fact is that, the transceiver should have metal plates, where the sample is placed between these plates. The problem with this arrangement is to make this type of detector sensitive to magnetic fields. This was a major limitation for abandoning the previous designs proposed.
One of the NMR sensors which has metal plates surrounding it is the microstrip configuration [57, 58]. The principle behind the working of the microstrip is shown in fig. 3.8.
From the fig. 3.8, it is clear that EM-wave propagates through the microstrip, in a quasi-TEM mode [53], i.e., the B_1 will always be orthogonal to the electric

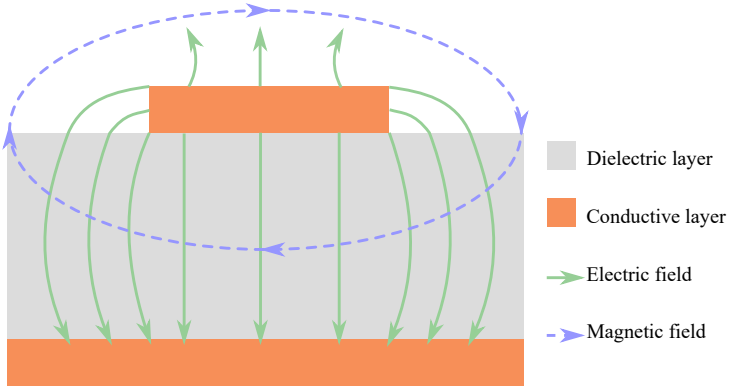

Figure 3.8: EM-field lines produced in a microstrip when excited with an RF source. The top conductive layer is the signal line, and the bottom conductive layer is the ground plane [53].

fields. The reason behind this is that the thickness of the dielectric layer is much lower than the wavelength of EM-wave, which allows the magnetic fields to be concentrated between the conductive layers [53]. To understand the design of the microstrip for chiral detection we need to first understand their working.

3.5.1 Microstrip transmission line

Most of the equations and the text explanation for the transmission lines are taken from the book [53].

The propagation of EM-wave through a transmission line is related by the eq. (3.3), and eq. (3.4). The propagation of the field is given by a propagation constant which is

$$\beta = \omega \sqrt{\mu_r \mu_0 \varepsilon_r \varepsilon_0}, \tag{3.13}$$

where, ω is the angular frequency of oscillation, μ_r is the relative permeability of the material between the metal plates, and ε_r is the relative permittivity of the dielectric between the metal plates [53].

Since for most materials $\mu_r = 1$, and

$$c = \frac{1}{\sqrt{\mu_0 \varepsilon_0}}, \tag{3.14}$$

where c is the velocity of light in a vacuum.
Therefore, the phase velocity of the propagation can be related as [53]

$$v_{\mathrm{p}} = \frac{c}{\sqrt{\varepsilon_{\mathrm{r}}}}. \tag{3.15}$$

These equations hold when the wave propagates in TEM mode; however, as stated above in the case of the microstrip, the wave propagates in a quasi-TEM mode [53]. As shown in fig 3.8, there are stray electric fields on the edges, and since the cross-section of the microstrip is finite, one needs to apply a correction factor to take the stray field effect into account.
The stray fields are taken into account by applying the necessary changes in the relative permittivity of the dielectric, as some parts of the electric fields propagate through free medium and some through the dielectric material.

$$\varepsilon_{\mathrm{eff}} = \frac{\varepsilon_{\mathrm{r}}+1}{2} + \frac{\varepsilon_{\mathrm{r}}-1}{2}\left(\sqrt{1+12\frac{d}{w}}\right)^{-1}, \tag{3.16}$$

where, $\varepsilon_{\mathrm{eff}}$ is the effective permittivity [59, 60]. Therefore, the eq. (3.13) and eq. (3.15) can be replaced with the $\varepsilon_{\mathrm{eff}}$ and the modified terms will be [59, 60].

$$\beta = \omega\sqrt{\mu_0 \varepsilon_{\mathrm{eff}} \varepsilon_0}, \tag{3.17}$$

and

$$v_{\mathrm{p}} = \frac{c}{\sqrt{\varepsilon_{\mathrm{eff}}}}. \tag{3.18}$$

Another important parameter to take into consideration is the characteristics impedance of the microstrip (Z_0), which depends on the ratio of the width of

the microstrip conductor (w) to the height of the dielectric layer (d). The Z_0 for the two cases is given as [59, 60]

$$Z_0 = \frac{60}{\sqrt{\varepsilon_{\text{eff}}}} \ln\left(8\frac{d}{w} + 0.25\frac{w}{d}\right), \tag{3.19}$$

when $w < d$, and

$$Z_0 = \frac{120\pi}{\sqrt{\varepsilon_{\text{eff}}}\left[\frac{w}{d} + 1.393 + \frac{2}{3}\ln\left(\frac{w}{s} + 1.444\right)\right]}, \tag{3.20}$$

when $w \geq d$.

These equations are important because to have a transmission of the EM-waves with low reflection it is important to match the Z_0 of the microstrip to the Z_0 of the feed line which is used for feeding the microstrip. For example, if the microstrip with a characteristic impedance of Z_0 of length l is connected to a feed line of impedance Z_{L}, then the input impedance that the microstrip will see is given by the equation [53]

$$Z_{\text{in}} = Z_0 \frac{Z_{\text{L}} + Z_0 \tanh(\beta l)}{Z_0 + Z_{\text{L}} \tanh(\beta l)}, \tag{3.21}$$

and the reflection coefficient as [53]

$$\Gamma = \frac{Z_{\text{L}} - Z_0}{Z_{\text{L}} + Z_0}. \tag{3.22}$$

If the feed line represents the Z_{L}, then to have minimum reflection, the Z_0 should be equal to the Z_{L}. In this case, the reflection coefficient will be zero. Therefore, from eq. (3.19) and (3.20) depending on the w and d of the microstrip, it is important to find the correct dimension to have the microstrip as impedance close to the feed line impedance.

Generally, the microstrip is designed for lengths much less than a quarter of the effective wavelength, to avoid standing waves on it [53]. It is possible to define the functioning of the microstrip with the width of the conductor. Depending

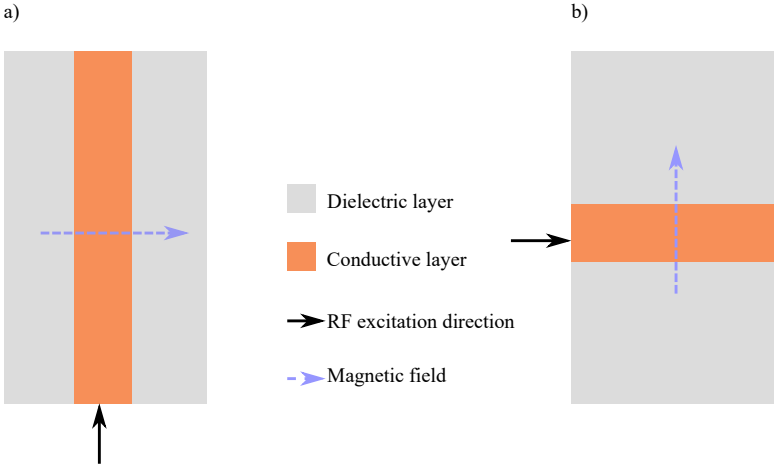

Figure 3.9: (a) and (b) show the effect on the direction of the magnetic field produced depending on the excitation direction. The arrow shows the position where the signal line is fed through, and the side opposite to it is either electrically shorted or open to the ground plane [53].

on the dimensions of the width, it can either act as an inductor or a capacitor. As shown in eq. (3.20) and (3.19), by defining the width the impedance of the microstrip can be set. For the region of the microstrip to work as an inductor it should have a higher impedance, and to work as a capacitive element it should have a lower impedance. The narrower section will have more current density; therefore, this particular region will produce a higher magnetic field compared to the capacitive section of the microstrip. Based on this principle, the NMR microstrip detectors are designed, where the sensitive region is made narrower than the rest of the section of the microstrip [57, 58].

Therefore, by adjusting the width of the conductor, a section of a microstrip can be made sensitive to magnetic moments, or electric dipoles. This feature is quite useful for designing the chiral detector since it is required to be sensitive to E_2 and B_1.

In chapter 2, in the chiral NMR Hamiltonian, it was shown that the RF perturbation had E_2 and B_1 component which had a phase difference of $\pi/2$, between them. A general question arises, since the magnetic and electric fields in the EM-waves are in phase with each other, then how come the fields were considered to be out of phase? To explain this, the microstrip needs to be considered as an antenna, as they radiate EM-waves. The equations used to explain this behaviour are taken from the book [61] chapter 9.
If we consider the RF's wavelength used for the experiments, then the wavelength associated with it is in the range of meters. The region of interest, i.e., where the sample will be placed on the microstrip will exhibit near-field effects since,

$$D \ll \lambda, \tag{3.23}$$

where, D is the maximum dimension of the microstrip, and λ is the wavelength of the RF excitation [61]. In this case, the reactive field with the radiating field will also need to be considered since there will be strong inductive and capacitive effects (or electric dipole moment in the case of antennas). To determine the effective field we will need to consider the magnetic vector potential which is related to the magnetic field by the following relation [61]

$$\nabla \times \vec{A} = \vec{B}. \tag{3.24}$$

Therefore, for an RF current flowing through the conductor, the solution for the magnetic vector potential can be found at position r' using the current density in the Lorenz gauge [61] (to find a unique solution for the EM-wave)

$$\vec{A}(r) = \frac{1}{c} \int \frac{\vec{J}(\vec{r'}) e^{i\vec{k}(\vec{r}-\vec{r'})}}{\left|\vec{r}-\vec{r'}\right|} d^3 r', \tag{3.25}$$

where, k is the wavenumber.

From the continuity equation, the charge density and the current density will be [61]

$$\frac{\partial \rho}{\partial t} = \nabla \cdot \vec{J}, \tag{3.26}$$

and the electric dipole moment as [61]

$$\vec{p} = \int \vec{r'} \rho(r') \, d^3 r'. \tag{3.27}$$

Using eq. (3.24), and (3.4) the electric field and the magnetic field will be [61]

$$\vec{B} = \frac{\mu c k^2}{4\pi} (\vec{n} \times \vec{p}) \frac{e^{\mathrm{i}k\vec{r}}}{r} \left(1 - \frac{1}{\mathrm{i}k\vec{r}}\right), \tag{3.28}$$

and

$$\vec{E} = \frac{1}{4\pi\varepsilon} \left(k^2 (\vec{n} \times \vec{p}) \times \vec{n} \frac{e^{\mathrm{i}k\vec{r}}}{r} + 3\vec{n}(\vec{n} \cdot \vec{p} - \vec{p}) \left(\frac{1}{\vec{r}^3} - \frac{\mathrm{i}k}{\vec{r}^2} \right) e^{\mathrm{i}k\vec{r}} \right). \tag{3.29}$$

where c is the speed of light in vacuum and $\vec{n}$ is the normal vector
From eq. (3.28) and eq. (3.29) it can be seen that for smaller values of r' the two fields can be approximated as [61]

$$\vec{B} = \frac{\mu c k^2}{4\pi} (\vec{n} \times \vec{p}) \frac{e^{\mathrm{i}k\vec{r}}}{r}, \tag{3.30}$$

and

$$\vec{E} = \frac{1}{4\pi\varepsilon} \left(3\vec{n}(\vec{n} \cdot \vec{p} - \vec{p}) \left(\frac{1}{\vec{r}^3} \right) \right). \tag{3.31}$$

Therefore, the two fields will oscillate with a phase difference of $\pi/2$, hence the reason for considering the out-of-phase E_2 and B_1 in the RF perturbation in eq. (2.132).
The next step in the design series is to design the microstrip which is sensitive to electric dipole and magnetic moment.

Microstrip design for sensitivity to electric dipoles

As explained in the previous section, if the width of the microstrip is widened, it behaves as a capacitive element.

One of the methods to excite electric dipoles is to place the sample between the capacitive plates. The voltage applied will charge the metal plates and hence an electric field is produced. The magnitude of the electric field produced will be inversely proportional to the distance between the plates. To have a sufficient volume of the sample, and to have a sensitive detector, the distance between the plates was fixed to 0.5 mm.

Since the Maxwell equations are reciprocal, therefore, the device which is sensitive to the electric dipole excitation is also sensitive to detect the electric dipole. Figure 3.10, shows the conductor arrangement to obtain such characteristics from the device, where the wider part produces more electric field than the narrow part. Another important factor that plays a role here is the direction along which the current is fed to the conductors. As it was seen from the fig. 3.9, the direction of the magnetic fields will depend on the direction of the current; therefore, the feed ports for the conductors are placed horizontally, with respect to the direction of B_0.

This ensured that the magnetic field produced was in the direction of the B_0. Since the fields produced due to the E_2 will be negligible compared to the magnitude of B_0, therefore, it could be neglected. This ensures that the magnetic field perturbation during the chiral spin excitation is limited, which will help reduce the noise in the chiral signal.

It was also important to feed the conductor simultaneously from the opposite direction, this ensured that the current flowing in the sample region was minimised and the symmetry of the current distribution was maintained.

This did not affect the potential difference between the plates, hence the E_2 between the metal plates is maintained.

After designing the electric dipole-sensitive part of the detector, the next step was to design the magnetic moment sensitive section of the microstrip.

Microstrip design for sensitivity to magnetic moment dipoles

After having designed the capacitor part of the detector, we need to design the section which was sensitive to magnetic dipole moments. As seen from the previous section, by adjusting the width of the microstrip, the section can be made to exhibit the property of an inductor. The fig. 3.10, shows the typical design for a conventional NMR experiment. The metal conductor is broader at the ends, which narrows itself towards the region of interest, i.e., where the sample would be placed. The optimisation of the detector and the computation was done using the commercially available software, COMSOL Multiphysics v5.4.
However, it needs to be integrated with the electric dipole-sensitive part. This was done by introducing a small gap between the magnetic section, and the remaining microstrip as shown in the fig. 3.11. Since, the current flowing sees a higher magnitude of impedance at this cross-section, than a directly connected path, the flow of the current is restricted. Therefore, when the magnetic section of the microstrip is active, the continuous current flow path is maintained along the length, which restricts the flow of the current in the electrical section of the microstrip. In this way, the condition that B_0, B_1 and E_2 need to be perpendicular to each other is maintained.
The conductor geometry was now optimised to have a sensitive detector with a maximum detection volume, where the k-value [46] condition was satisfied in the detection region. With this, a detector which obeys the properties required for chiral signal detection was designed. The design rules and the implementation are explained in the next section.

3.6 Optimising the chiral signal sensitive microstrip design for maximising detection volume

In the previous section, the integration of the electric dipole and magnetic moment-sensitive section of a microstrip was explained. However, the design which gave

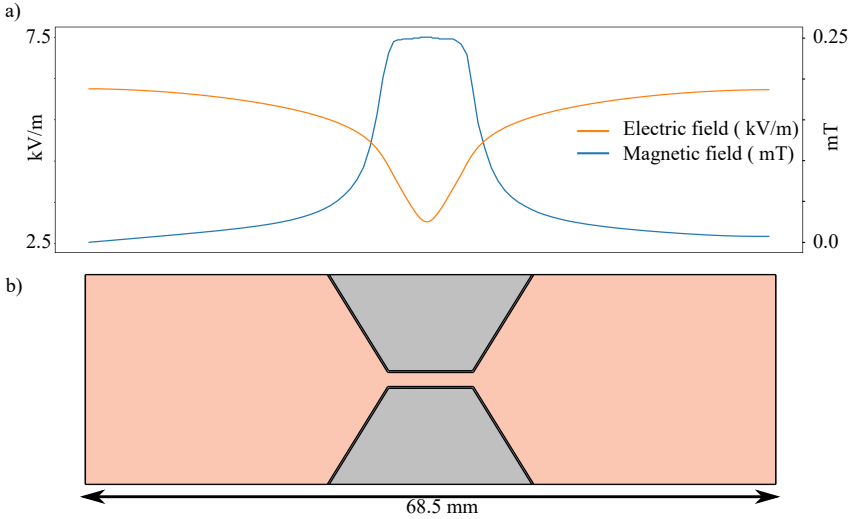

Figure 3.10: Typical design for a microstrip detector used in NMR [57, 58]. (a) Plot of the magnitude of the electric field and the magnetic field produced along the detector in (b) between the two conductive layers. As can be seen, the inductive region produces a high-magnitude magnetic field, and is sensitive to magnetic dipoles, whereas the capacitive region produces high-order electric fields.

the strongest signal still needed to be found. The objective function was to find the maximum detection volume which satisfies the k-value condition.

The initial geometric notations are shown in the fig. 3.11. Based on this, the geometrical coordinates of the conductor geometry for the region of interest, i.e., where the sample was placed were defined on the width (w_{ROI}) and the length (l_{ROI}) of the detection region. By sweeping the length of the detection region, the optimum sample length was found. The relations between the coordinates and the detection region dimensions were

$$x_1 = 0.5\ w_{\mathrm{ROI}}, \tag{3.32}$$

$$y_1 = 0.5\ l_{\mathrm{ROI}}. \tag{3.33}$$

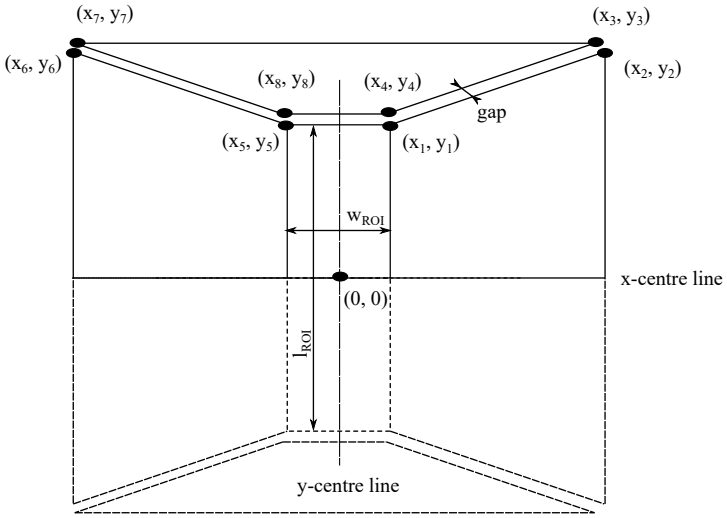

Figure 3.11: Geometrical definition.

For x_2,

$$x_2 = (8.5 - 0.5\ w_{\mathrm{ROI}})\tan(\theta) - 0.5\ l_{\mathrm{ROI}}, \tag{3.34}$$

if $x_2 > 8.5$ then

$$x_2 = 8.5. \tag{3.35}$$

For y_2,

$$y_2 = (8.5 - 0.5\ w_{\mathrm{ROI}})\tan\theta - 0.5\ l_{\mathrm{ROI}}, \tag{3.36}$$

if $y_2 > 8.5$ then

$$y_2 = 8.5. \tag{3.37}$$

For x_3 and y_3,

$$x_3 = 0.5\ w_{\mathrm{ROI}} - \mathrm{gap}\ \sin(\theta), \tag{3.38}$$

$$y_3 = 0.5\ l_{\mathrm{ROI}} + \mathrm{gap}\ \cos(\theta). \tag{3.39}$$

For x_4,

$$x_4 = 0.5\ w_{\mathrm{ROI}} - \mathrm{gap}\ \sin(\theta) + \frac{8.5 - 0.5\ w_{\mathrm{ROI}} + \mathrm{gap}\ \sin(\theta)}{\tan(\theta)}, \tag{3.40}$$

if $x_4 > 8.5$ then,

$$x_4 = 8.5. \tag{3.41}$$

For y_4,

$$y_4 = 0.5\ w_{\mathrm{ROI}} - \mathrm{gap}\ \sin(\theta) + \frac{8.5 - 0.5\ w_{\mathrm{ROI}} + \mathrm{gap}\ \sin(\theta)}{\tan(\theta)}, \tag{3.42}$$

if $y_4 > 8.5$ then,

$$y_4 = 8.5. \tag{3.43}$$

where the values of the variables defined are summarised in table 3.3.

Table 3.3: Values of the variable fixed for the microstrip geometry

Variable	Value
w_{ROI}	2 mm
θ	70°
gap	0.2 mm
l	17 mm
w	17 mm

After defining the first four coordinates, the other coordinates' definition became easier. Since the detector is symmetric about the x- and y-axis, therefore, the

other points were mirror symmetries along the centre planes. For the remaining coordinates

$$(x_5, y_5) = M_y\,[x_1, y_1]\,, \tag{3.44}$$

$$(x_6, y_6) = M_y\,[x_2, y_2]\,, \tag{3.45}$$

$$(x_7, y_7) = M_y\,[x_3, y_3]\,, \tag{3.46}$$

$$(x_8, y_8) = M_y\,[x_4, y_4]\,, \tag{3.47}$$

where, M_y is the mirror transformation about the y-axis. Similarly, for the geometry below the centre lines, the coordinates are the reflection of points 1-8 respectively, about the x-axis.

To, interface the detector with the RF ports, the microstrip was adjusted to have a characteristic impedance of $50\,\Omega$. The reason for doing this was explained in section 3.5.1, i.e., to reduce reflection losses. Another reason for having the extruded impedance line was that the RF port connections should not interfere with the electric and magnetic field profile produced by the detector. The width of the RF ports was calculated from eq. (3.19) and (3.20). The geometry with the interface lines is shown in fig 3.12

After finding the optimum length, the swept boundaries were made smaller and the sweep steps finer. The final search was carried between the length of 9 mm to 9.5 mm, in the steps of 0.1 mm. Table 3.4 summarises the result of the length adjustment, and fig 3.13 shows the k-value distribution in the sample region. From the results, the length of the sample chosen was 9.2 mm, since at this length the k-value is minimum which satisfies the equation, and the volume where the sample could be placed, or the chiral sensitive region is larger compared to the other lengths.

The final step in the design optimisation series, was to minimise the current density distribution, as it directly relates to the B_1 produced, which is something that needs to be avoided at the E_2 ports of the detector. This was done by tapering the

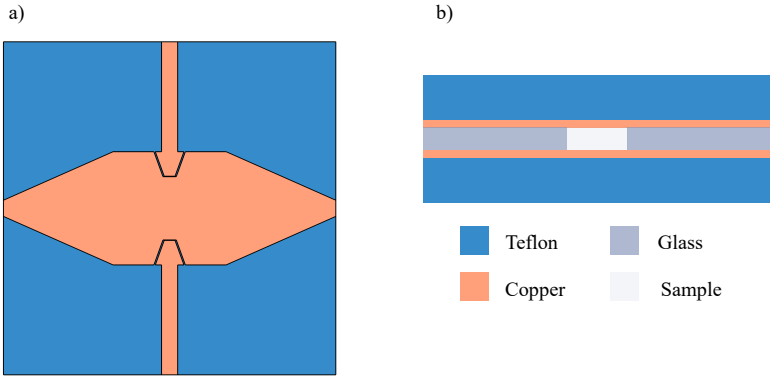

Figure 3.12: (a) Final microstrip geometry with the 50 Ω transmission line connected to the detection zones. (b) Side sectional view of the stacked microstrip detectors.

Table 3.4: The sensitive volume obtained with the averaged *k* for different sample lengths.

Sample Length mm	ROI Volume mm^3	Averaged k-value in Ω_{sample} $\log_{10}$
9.0	6.088	-4.177
9.1	6.403	-4.165
9.2	6.605	-4.106
9.3	6.672	-4.036
9.4	5.937	-3.967
9.5	3.476	-3.899

conductor from the 50 Ω connection to the detection region. Figure 3.12 shows the final design of the detector.

3.7 Setup for electromagnetic field calculation for the chiral sensitive microstrip detector

The figure 3.12, shows the cross-section of the device with different layers. The domain and the material used are defined in the table 3.5

Table 3.5: Computational domains and the material properties assigned to mimic the electromagnetic behaviour of the material [53]

Domain	material	Conductivity ($\mathrm{S\,m^{-1}}$)	dielectric constant
Ω_{PCB}	Teflon	0	2.55
Ω_M	Copper	5.998×10^7	1
Ω_{sp}	glass	0	4.6
Ω_{sample}	enantiomeric sample	0	1

E_2 and B_1, can be represented with a time-harmonic behaviour, where the amplitude is proportional to $\exp(\mathrm{i}\omega t)$, where ω, is the angular frequency of oscillation, and t is the time. The eq. (3.3) and (3.4) can be transformed to frequency domain such that the EM-wave propagation can be defined by the following equations

$$\nabla \times \mu_{\mathrm{r}}^{-1}(\nabla \times \vec{E}) = \mu_0 \varepsilon_0 \omega^2 \left(\varepsilon_{\mathrm{r}} - \frac{\mathrm{i}\sigma}{\omega_0} E \right) \in \Omega, \tag{3.48}$$

where,

$$\Omega = \Omega_{PCB} \cup \Omega_M \cup \Omega_{sp} \cup \Omega_{sample}, \tag{3.49}$$

and μ_{r} is assumed to be unity for the calculation. ε_{r} is the relative permittivity and σ is the electrical conductivity [55] . The values for different domains (or materials) are taken from table 3.5. The simulation domain Ω is truncated by a perfectly electric conductor, such that on its boundary [55]

$$\vec{n} \times \vec{E} = 0 \text{ on } \partial\Omega. \tag{3.50}$$

Since the electric field dependence on the current density is defined in the equation above, and there are no free charges; therefore, from eq (3.48) one can derive a divergence-free condition to find a unique solution for the EM-field, which will be given as [55]

$$\nabla \cdot \vec{E} = 0 \in \Omega. \tag{3.51}$$

Generally, for RF simulation in COMSOL Multiphysics, to define a conductive material the domain is truncated by an impedance boundary condition. By doing so, the decay of current is mimicked by assigning electric current on the exterior of its boundary. This excludes the metallic domain and the number of nodes for calculation. Though it is a good approximation, where the metal thickness is much larger than the skin depth, in this calculation we used a transition boundary condition. The reason was, the design of the detector and the eventual chiral signal measurement is sensitive to the magnetic field produced by the electric field, it was important to calculate the effects of the decaying current as well. The metal thickness was 35 µm, and the skin depth corresponding to 500 MHz is approx. 3 µm.

This doubles, the mesh node points for the calculation, but ensures an accurate output to a real-world environment. The transition boundary condition was implemented using the equation below

$$\vec{J}_1 = \frac{\mathrm{i}\sqrt{\sigma + \mathrm{i}\omega\varepsilon}}{\sqrt{\mathrm{i}\omega\mu}} \left[\frac{E_{\mathrm{t}1} \cos \gamma d - E_{\mathrm{t}2}}{\cos^2 \gamma d - 1} \right] \text{ on } \partial\Omega_{M1}, \tag{3.52}$$

and

$$\vec{J}_2 = \frac{\mathrm{i}\sqrt{\sigma + \mathrm{i}\omega\varepsilon}}{\sqrt{\mathrm{i}\omega\mu}} \left[\frac{E_{\mathrm{t}2} \cos \gamma d - E_{\mathrm{t}1}}{\cos^2 \gamma d - 1} \right] \text{ on } \partial\Omega_{M2}. \tag{3.53}$$

where Ω_{M1}, and Ω_{M2} are the boundaries on either side of the metallic domain, and $E_{\mathrm{t}1}, E_{\mathrm{t}2}$ are the tangential component of electric fields on its surface [55].

The final setup in the computation was to add the excitation ports for E_2 and B_1 as shown in fig 3.13. When the E_2 ports were active, the B_1 ports were turned off and

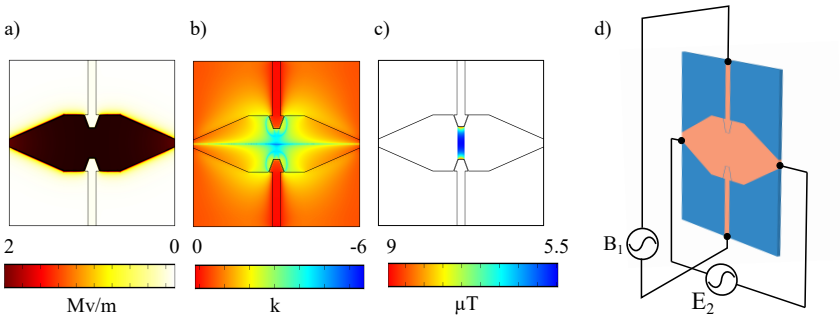

Figure 3.13: (a) Electric field sensitivity of the detector for a kV of voltage applied. (b) *k*-value distribution of the detector. At the sensitive region where the sample will be placed, it is less than -4. (c) Magnetic field sensitivity of the detector. The sensitivity was calculated by exciting the ports with an RF current of 1 A, and determining the magnitude of the magnetic field produced (d) Circuit schematic for the electric field excitation and magnetic field detection.

vice-versa. Both the ports were set such that the termination has a characteristic impedance of 50 Ω.

The E_2 ports were excited with a voltage of 1 kV. Figure 3.13, shows the E-field sensitivity of the detector for 1 kV of the voltage applied.

To find the sensitivity of the detector for the magnetic moment the reciprocity principle of Maxwell's equation was used, i.e., by calculating the magnetic field produced at 1 A, we calculated the $\mu T\,A^{-1}$ field produced, as shown in fig 3.13.

3.8 Electric and magnetic field decoupled microstrip detector

One of the major drawbacks of all the detectors discussed above was the dependence on the electric field and the magnetic field for the chiral signal measurement. This poses a challenge for chirality detection, since any altercations in the design due to fabrication limitations, positioning of the detector, mounting of the detector on a probe head, or changes in the dielectric permittivity of either the

sample or the printed circuit board (PCB) material affects the k-sensitive region of the detector.

Therefore, it was important to have a detector which overcomes these challenges while having separate ports for the E_2 and B_1.

From the discussions for the microstrip, and as shown in the fig. 3.14 most of the microstrip-based NMR detectors have certain geometry, i.e., a wider capacitive region, a narrow inductive region followed by a wider region.

By adjusting the length of the total conductive part, and the width of the different regions it was possible to design the microstrips for the required eigenfrequency.

Another important aspect of the microstrip was that depending upon the angle of the conductive part between the capacitive and the inductive region, it was possible to optimise the shape of the microstrip to minimise B_0 inhomogeneity.

This gave design flexibility to optimise the detector for high RF efficiency while reducing inhomogeneity due to the susceptibility mismatch.

Figure 3.14 summarises the above discussion while showing the computation setup.

Another advantage of having a microstrip for chiral NMR measurement is that the sample is placed between two metallic plates. This gave a perfect opportunity for high magnitude E_2 excitation, while allowing independent control over the E-field and the B-field excitation.

One remaining challenge was that the microstrip circuit was optimised for the B_1 excitation, using the same RF port for the E_2 would require electrical components which could handle high voltages (in the range of kV). Switching between the transmitter and receiver circuit, and finally taking care of the magnetic field produced between the metal plates.

To overcome these challenges, we place the microstrip between metallic plates used for E_2 production as shown in fig. 3.14. The excitation of the outer metal plates produced the required E_2 between the metal surfaces on the microstrip. This allows for a higher magnitude of the E_2, which depends inversely on the distance between the metal plates.

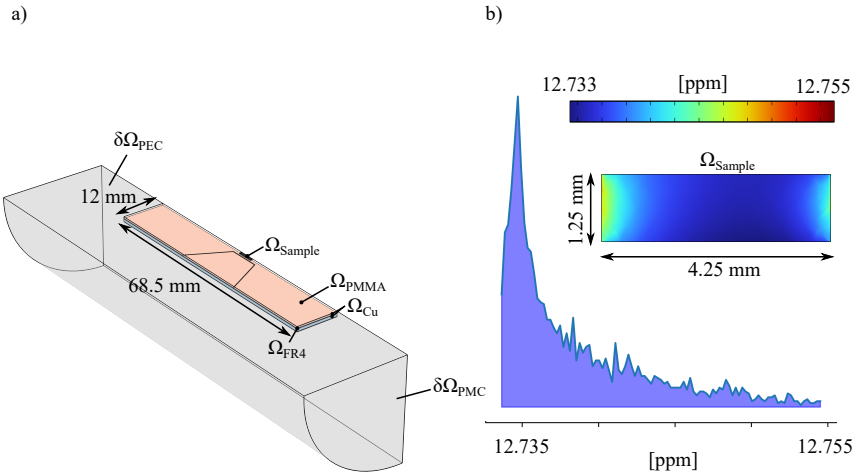

Figure 3.14: (a) Simulation setup for measuring the eigenfrequency of the microstrip design used for chiral measurements. The computational domain was set up in a quadrant, where the symmetry conditions were set with a perfect magnetic conductor boundary (PMC), and perfect electric conductor (PEC) boundary conditions. The entire computational domain was truncated with a PEC boundary condition. The eigenfrequency was computed using COMSOL and was determined to be 684 MHz. (b) Magnetic field distortion in the sample region to characterise the intrinsic inhomogeneities caused by the detector's design. The values in parts per million (ppm) correspond to a difference in the magnetic field values relative to 11.74 T. The magnetic susceptibility values were taken from [62], and the computational error tolerance was set to 0.01 parts per billion (ppb). The magnetic field inhomogeneity was calculated using COMSOL, and from the results, the difference between maximum and minimum distortion corresponds to 10.64 Hz for ^{1}H at 11.74 T.

One of the cases discussed in chapter 2 for chirality detection was that it was possible to achieve a high chiral signal by flipping the net magnetisation to π. With the detector design mentioned in this section, it is now possible to achieve that by the combination of the B_1 produced by the magnetic port, superimposed by the magnetic fields produced due to the E_2.

To achieve the condition of the detection it was important to design a circuit such that the magnetic port of the circuit is tuned and matched to the desired frequency, while the impedance of the electrical port of the circuit remains capacitive. These

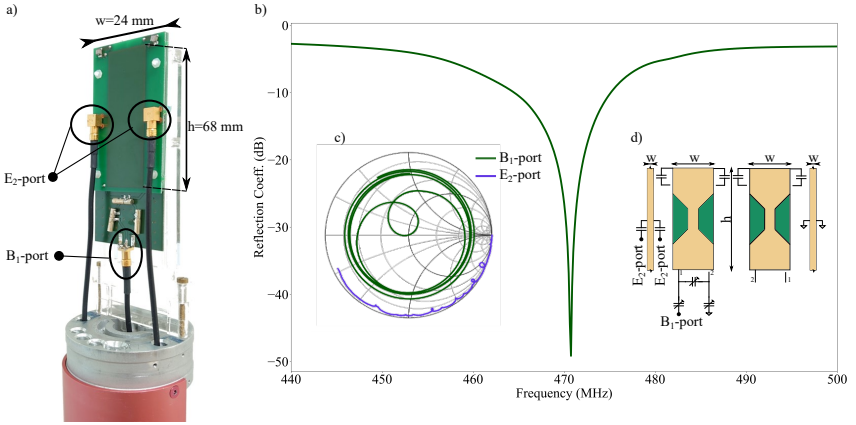

Figure 3.15: (a) Microstrip-based chiral detector mounted on a customised probe head. The sample, sealed in a glass capillary was placed between the metal plates. (b) Reflection curve of the magnetic field port. (c) Smith chart for the magnetic and electric field ports plotted in the frequency range 440 MHz to 500 MHz. (d) Circuit schematic of the chiral microstrip detector.

characteristics of the detector were achieved using the circuit design shown in fig. 3.15 (d).

The designed circuit was fabricated on a 2-layer printed circuit board (PCB) with FR4 as the core material. The PCB was ordered from Multi Leiterplatten GmbH, Germany.

Figure 3.15 shows the measurement results acquired using vector network analyser E5071C, (Keysight, Germany), with the coaxial cable calibrated to mimic a 50 Ω port.

To summarise the discussion in this chapter, we started with the design proposed by [54]. It had its shortcoming of which the main factor was placement of the magnetic moment detector. This was overcome by the design of a miniaturised version of the detector explained in section 3.3. One of the major challenges with this approach was the coupling of energy into the resonator, as the magnitude E_2 required for chiral distinction was in the range of kV. To overcome this challenge the miniaturised ring loop resonator was designed to have active RF ports

to overcome the challenge of field excitation, which is explained in section 3.4. As the filling factor of the coil in this approach was very low, it was at the limits to detect magnetic moment dipole. Hence, the resonator design was abandoned to a microstrip-based design. The first microstrip-based resonator design was explained in section 3.6, where it was possible to maintain the k-value requirement by switching between B_1 and E_2 ports. Since this was difficult to achieve the final design was based on a conventional NMR microstrip-based detector with additional capacitor plates for E_2 excitation. This allowed decoupling the B_1 and E_2. The proposed the approach of flipping the magnetisation by π. The results of this approach and the final detector design are discussed in the next chapter.

4 Chiral distinction in NMR using a microstrip based transceiver

In the previous chapter, the design of a chiral transceiver is explained. In this chapter, the setup and the experimental routines that were used for chirality distinction are described.

The detector has three RF-ports. One for the exciting and detecting magnetic dipoles, mentioned as B_1 port, and two for the excitation of the electric dipoles, mentioned as E_2 port.

As the detection of the signal is from the B_1 port, it was important to make it as sensitive as possible to the magnetic dipole. This was achieved by tuning to the desired frequency and matching it as close as possible to $50\,\Omega$. Proper matching ensured low reflection losses.

Since the detector also has electric ports, it was necessary to ensure that these ports remains capacitive. This helps to reduce stray magnetic fields, and increases the excitation sensitivity of the electric dipoles. The fig. 3.15 shows the smith of the B_1 and E_2 ports.

The tuned and matched detector was mounted on a probe provided by Voxalytic GmbH, Germany. The probe was used as a interface between the detector, and the spectrometer. The spectrometer was a vertical bore superconducting magnet, AVANCE III, from Bruker, Germany, and had a magnetic field strength of 11.74 T. The ^{1}H Larmor frequency was 500.13 MHz

The magnetic and electric fields were generated using the pre-amplifier 1H LNA MODULE 500, from Bruker, Germany. For the E_2 since the impedance of the port was measured, the voltage delivered to the port could be calculated from the power applied to the ports.

4.1 NMR characterisation of the detector's magnetic moment detection capabilities

The first step was to characterise the B_1 port of the detector. The NMR signal acquired was used to shim the sample region. The shimming procedure was done to homogenise the B_0 fields.
The sample used for the characterisation was a racemate (equal concentration of enantiomer pairs) of 1,1,1-trifluoropropan-2-ol. The sample was sealed in a square glass capillary of inner dimension 0.7 mm, up to a height of 6 mm. This gave an effective volume of 2.94 µL.
The $\pi/2$ pulse calibration was done on the signal at -85 ppm. The power used for the pulse calibration was 20 W. The pulse length for the $\pi/2$ flipping of magnetisation was measured to be at 7 µs.
The nutation plot was also used to measure the RF homogeneity of the microstrip. It was calculated as the ratio of the amplitude at $9\pi/2$ with the amplitude at $\pi/2$, which was 98.46%.
The next step was to repeat the measurement when an electric field was applied to the detector.

4.2 Proof of principle using ^{19}F spectroscopy on 1,1,1-trifluoropropano-2-ol

As discussed in Chapter 2, the probability of detecting a chiral signal increases, when the net magnetization is flipped by π rad. Since it was impossible to control the magnetic fields produced by the E_2, the magnetic port was used to add additional field strength to obtain the required B_1 flip. The pulse lengths for the E_2 and B_1 were set at 14 µs because from the nutation plot in fig 4.1 this was the pulse length for π rad flipping. Though there were stray magnetic fields from E_2; however, they were not strong enough to produce a large deviation from π. Hence, the measurements can be considered as discussed in chapter 2, "Magnetisation flipped at an arbitrary angle".

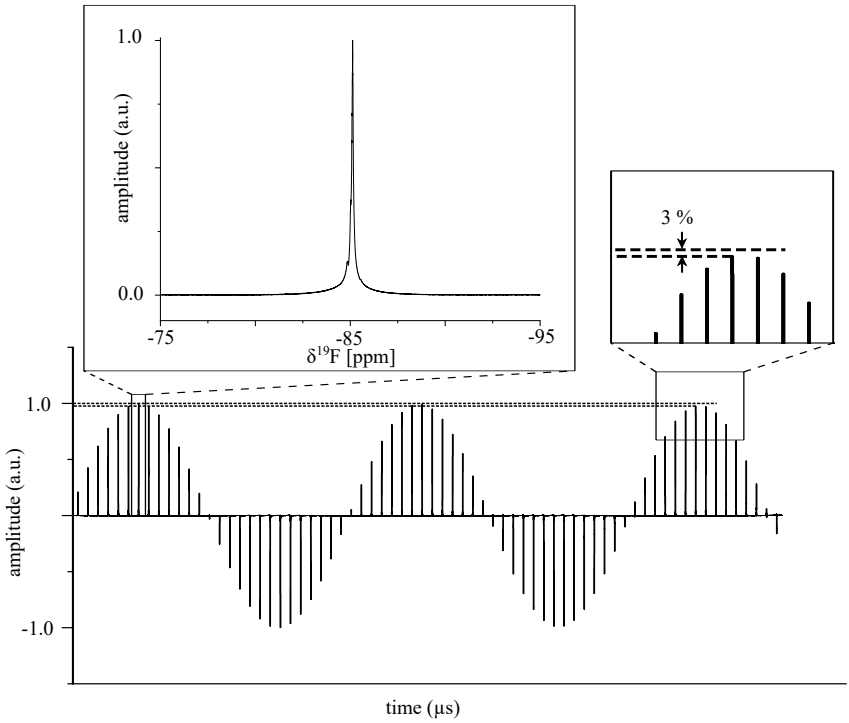

Figure 4.1: Nutation plot of 1,1,1-trifluoropropano-2-ol using ^{19}F NMRspectroscopy. The difference in the amplitude ratio at $\pi/2$ and $9\pi/2$ was 3%. The signal obtained at $\pi/2$ was used as a reference for NMR characterisation, where the linewidth measured at full width at half maximum (FWHM) was approx. 35 Hz.

For the experiments, a new pulse program was developed. The logic behind the pulse program was that it excites B_1 with a certain phase and the E_2 with a respective phase difference of $\pi/2$ from B_1, and only detects the magnetisation relaxation from the B_1 port. The receiver phase was set equal to the excitation phase of B_1. The pulse program was written in the TopSpin version 4.1.3 from Bruker, Germany and is shown in the listing below

```
;zg equivalent of chiral detection
;developed by S. Wadhwa & J.G. Korvink
```

```
;March 2023
#include <Avance.incl>
#include <De.incl>

"acqt0=-p1*2/3.1416"

1 ze1
  30m
2 d1 pl1:f1 pl2:f2
  (ralign (p1 ph1):f1 (p2 ph1):f2)
  ACQ_START1(ph30,ph31)
  0.1u DWELL_GEN1
  (aq1)
  eosc1
  ;rcyc=2
  lo to 2 times ns
  30m wr1 #0
exit


ph1=0
ph2=1
ph31=0

;F1:magnetic port, transceive operations
;F2:electric port, transmission operations
```

Listing 4.1: Pulse program for chiral distinction.

After finding the pulse parameters that produce the desired result with the racemic mixture, it was replaced with a 100% enantiomeric excess (ee) sample. The enantiomer used for the measurement was (R)-1,1,1,-trifluoropropan-2-ol (from Merck, Germany).

Before starting the measurement for the chirality detection, a standard NMR routine was repeated to shim the sample. This was necessary as any orientation changes because of unloading and loading the probe had to be corrected to ensure that the line width and shape were similar in all the experiments.

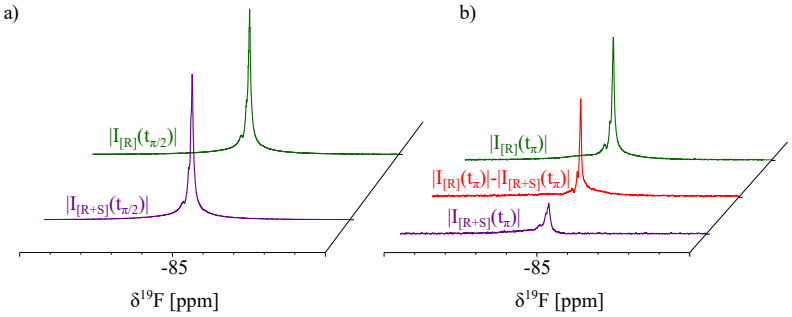

Figure 4.2: (a) The comparison of the spectrum obtained for a racemic, and the enantiopure sample at $\pi/2$ pulse length. The signal magnitude for both samples was equal. The spectra were obtained with identical pulse parameters. (b) The comparison of the signal magnitude when an electric field is applied together with a π pulse. The red curve is the difference between the magnitude of racemic, and the (R)-. The intensity of the curve $\neq 0$ was the proof for the chiral signal.

The fig. 4.2, shows the spectra acquired and the table 4.1 compares the relative intensity values for different scenarios. The results showed a difference in the

Table 4.1: Ratio of the intensities compared to the intensity obtained by a $\pi/2$ pulse on racemic sample.

Intensity ($\|I\|$)	$\|I\|/\|I_{[R+S]}(t_{\pi/2})\|$
$\|I_{[R]}(t_{\pi/2})\|$	1
$\|I_{[R+S]}(t_{\pi})\|$	0.025
$\|I_{[R]}(t_{\pi})\| - \|I_{[R+S]}(t_{\pi})\|$	0.08
$\|I_{[R]}(t_{\pi})\|$	0.1

magnitude observed between the racemic, and the 100% ee sample for the same pulse parameters. This is a clear indication of the presence of a chiral signal, where the coupling between the electric dipole and the magnetic field led to a change in the flip angle of the net magnetisation.

To calculate the chirality constant eq. (2.159) was used, where the magnitude of intensity for a sample with ee can be related as

$$I_{\text{ee}} \propto \mp \hat{I}_x \sin \omega_{E_2} t_1 \cos \omega_{B_1} t_1 + \hat{I}_y \sin \omega_{B_1} t_1 . \tag{4.1}$$

Since for a racemic sample, the chirality constant should cancel out, therefore,

$$I_{\text{racemic}} \propto \hat{I}_y \sin \omega_{B_1} t_1 , \tag{4.2}$$

The signal acquired for this sample at π-pulse had intensity $\neq 0$, and was roughly 2.5% of the intensity at $\pi/2$ pulse lengths. From these observations, the actual angle by which the net magnetisation was flipped in the presence of E_2 is calculated, where the pulse lengths for both the ports were 14 µs,

$$.025 = \sin(\omega_{B_1} x), \tag{4.3}$$

where, ω_{B_1} is known from the $\pi/2$ pulse calibration to be, $\omega_{B_1} = \pi/14$. Using this in the above equation

$$x = \frac{14 \arcsin(.025)}{\pi} = 13.889\,\mu\text{s}, \tag{4.4}$$

assuming that the analogous pulse length should be close to 14 µs. With this, the effect of applying the E_2 with the B_1 is known. If we use this in the eq. (2.159)

$$|I_{[R]}|(t_\pi) = \mp \sin(\omega_{E_2} 14) \cos\left(\frac{13.889\pi}{14}\right) + \sin\left(\frac{13.889\pi}{14}\right) \tag{4.5}$$

the ratio of the intensities results in

$$\frac{|I_{[R]}|(t_{\pi/2})}{|I_{[R]}|(t_\pi)} = \frac{1}{\sin(\omega_{E_2} 14)(-0.999) + 0.0249}. \tag{4.6}$$

The ratio of the intensity from table 4.1 was 10%, which results in ω_{E_2} =0.053 rad µs^{-1}. Using it in eq. (2.133) where, γ_r for ^{19}F is 251.815 rad µs^{-1} T^{-1}, B_0 was 11.74 T.

The magnitude of E_2 was calculated by calculating the port impedance of the electric port from the Smith's chart shown in fig. 3.15 (c) and the power applied for the excitation. For 1 W of power the voltage drop across the port was 25.721 V. Since the distance between the metal plates was 1 mm, this corresponds to electric field of 25.721 $\mathrm{kV\,m^{-1}}$ Using these values in eq. (2.133), the value of the chirality constant (σ_c) is $1.4 \times 10^{-10}\,\mathrm{m\,V^{-1}}$.
Compared to the value estimated by [46] the chirality constant was 10^5 times more. Due to the deviation from the theoretical value, and lack of measurement data to compare, additional experiments were performed to investigate the method.
The results obtained from these measurements are discussed further.

4.3 1,1,1-trifluoropropano-2-ol using ^{1}H spectroscopy

In the previous section, the theory of chirality distinction explained in chapter 2 was proved, i.e., for the magnetisation flipped by approximately π in the presence of an electric field produces a chiral signal, and for the magnetisation flipped by $\pi/2$ the chiral signal vanishes. To check the method's applicability range a new set of measurements were acquired using ^{1}H spectroscopy. The measurements were started by standard NMR routines which include pulse calibration for $\pi/2$ flip angle, shimming and intensity adjustment for the racemic and (R)- sample. Figure 4.3 shows the comparison of spectra acquired at $\pi/2$ pulse time for the racemic and (R)- sample. These acquisitions were done in the absence of E_2. A difference to the ^{19}F spectroscopy was that instead of single peak there were multiple peaks from ^{1}H nuclei. Since the relative intensities of **B** and **C** with respect to **A** were different for the two samples, another technique was used to determine the chiral constant. In this method, the spectra for calculating the chiral constant were done in the presence of an E_2 field with different E_2 pulse lengths. The pulse program used for this measurement was

```
1 ;zg equivalent of chiral detection with independent electric
      and magnetic field pulse lengths
```

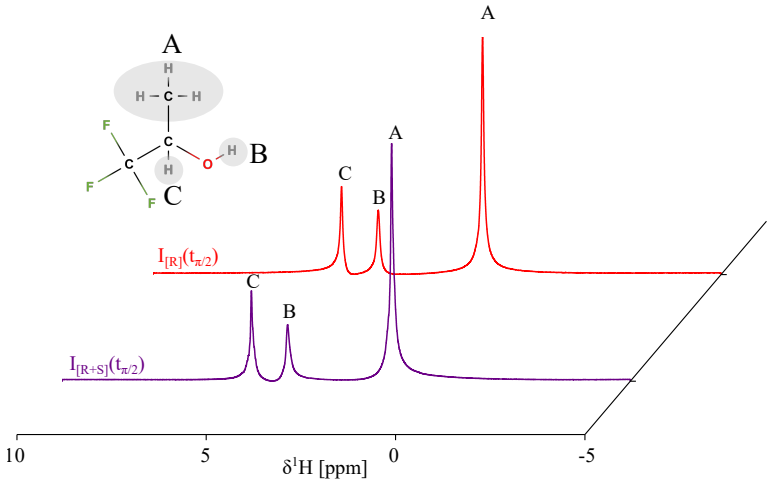

Figure 4.3: ^{1}H NMR spectrum acquired for 1,1,1-trifluoropropan-2-ol at $\pi/2$ pulse length for the racemic and a (R)- sample. The letter labelled on top of the peaks represents the signal from the ^{1}H labelled in the chemical structure. The chemical structure shown is a 2-D representation of (R)-1,1,1-trifluoropropan-2-ol.

```
;developed by S. Wadhwa, R.Kampmann & J.G. Korvink
;October 2023
#include <Avance.incl>
#include <De.incl>

"acqt0=-p1*2/3.1416"

1 ze1
  30m
2 d1 pl1:f1
  (ralign (p1 ph1):f1)
  d2 pl2:f2
  (ralign (p2 ph2):f2)
  ACQ_START1(ph30,ph31)
  0.1u DWELL_GEN1
  (aq1)
  eosc1
```

```
  ;rcyc=2
  lo to 2 times ns
  30m wr1 #0
exit


ph1=0
ph2=1
ph30=0
ph31=0

;F1:magnetic port, trasnceive operations
;F2:electric port, transmission operations
```

Listing 4.2: Pulse program for chiral distinction with independent electric and magnetic field pulse lengths.

The intensities obtained were a function of two variables t_1 and t_2 such that

$$I_{ee}(t_1,t_2) \propto \mp\hat{I}_x \sin\omega_{E_2} t_2 \cos\omega_{B_1} t_1 + \hat{I}_y \sin\omega_{B_1} t_1 . \tag{4.7}$$

Here the interaction between different ^{1}H nuclei was neglected for the ease of explanation and calculation. The pulse length at the B_1 port was set fixed at 10 µs, the above equation could be rewritten as

$$I_{ee}(t_2) \propto \mp\hat{I}_x \sin\omega_{E_2} t_2 \cos(\omega_{B_1} 10\,\mu s) + \hat{I}_y \sin\omega_{B_1} 10\,\mu s. \tag{4.8}$$

From the normal routine the $\pi/2$ pulse was found to be at 5.5 µs, therefore,

$$\omega_{B_1} = \frac{\pi}{(2)(5.5\,\mu s)}, \tag{4.9}$$

which simplifies the chiral intensity equation to

$$I_{ee}(t_2) \propto \mp\hat{I}_x \sin\omega_{E_2} t_2 \cos(0.91\pi) + \hat{I}_y \sin(0.91\pi). \tag{4.10}$$

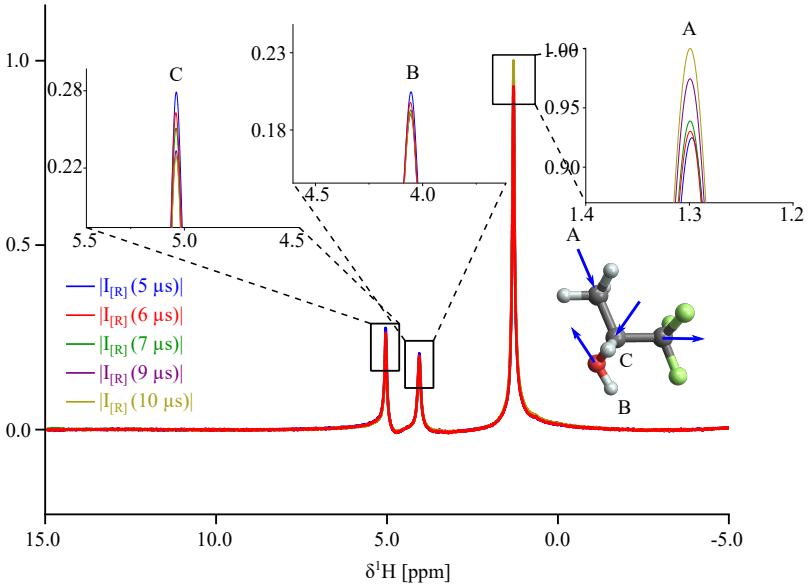

Figure 4.4: ^{1}H NMR spectrum acquired for 1,1,1-trifluoropropan-2-ol close to π pulse length for the (R)- sample. The letter labelled on top of the peaks represents the signal from the ^{1}H labelled in the chemical structure. The blue arrows on the chemical structure show the direction of the electric dipoles. The length of the arrows is not scaled to the actual magnitudes. The intensity of the peak labelled **A** increases with increasing pulse lengths of E_2, and the intensity of peaks labelled **B** and **C** reduces.

The spectra acquired for different t_2 values and the behaviour of different peaks are shown in the fig. 4.4 for the (R)- and in fig. 4.5 for the racemic sample. The table 4.2 and 4.3 summarises the measurement relative intensities for different frequency shifts and different t_2 values. As observed from the measurement, the intensities of the peaks labelled **B**, and **C** in fig 4.4 reduced when increasing the E_2 pulse duration. This trend was opposite to the one observed in the ^{19}F acquisitions. However, the intensity of the peak labelled **A** increased with increasing the E_2 pulse duration. These phenomena can be explained if instead of 2-D, we look at the 3-D structure of the molecule as shown in the fig. 4.4, the electric dipoles

Table 4.2: Ratio of the intensities compared to the intensity obtained at different E_2 pulse lengths for the (R)- sample. The intensity from the ^{1}H position is referred from fig. 4.4 and all the peak intensities were calculated relative to the peak intensity at 1.3 ppm for $t_2 = 5\,\mu s$.

Intensity $\lvert I_{[R]}(t_2)\rvert$	A (@1.3 ppm)	B (@4.5 ppm)	C (@5.04 ppm)
$\lvert I_{[R]}(5\,\mu s)\rvert$	1	0.2353	0.2977
$\lvert I_{[R]}(6\,\mu s)\rvert$	1.0056	0.2283	0.2843
$\lvert I_{[R]}(7\,\mu s)\rvert$	1.0151	0.2229	0.2743
$\lvert I_{[R]}(9\,\mu s)\rvert$	1.0538	0.2199	0.2597
$\lvert I_{[R]}(10\,\mu s)\rvert$	1.0814	0.2208	0.2559

Table 4.3: Ratio of the intensities compared to the intensity obtained at different E_2 pulse lengths for the racemic sample. The intensity from the ^{1}H position is referred from fig. 4.5 and all the peak intensities were calculated relative to the peak intensity at 1.3 ppm for $t_2 = 5\,\mu s$.

Intensity $\lvert I_{[R+S]}(t_2)\rvert$	A (@1.3 ppm)	B (@4.05 ppm)	C (@5.04 ppm)
$\lvert I_{[R+S]}(5\,\mu s)\rvert$	1	0.1401	0.1635
$\lvert I_{[R+S]}(6\,\mu s)\rvert$	1.0612	0.1434	0.1549
$\lvert I_{[R+S]}(7\,\mu s)\rvert$	1.1343	0.1502	0.1526
$\lvert I_{[R+S]}(9\,\mu s)\rvert$	1.2664	0.1705	0.1675
$\lvert I_{[R+S]}(10\,\mu s)\rvert$	1.3349	0.1823	0.1840

associated with peaks **B** and **C** are in the opposite directions as compared to the peak of **A**, which is in the same direction as ^{19}F atoms.

We can now use the relative intensities values from the table 4.2, to measure the chirality constant. The general form for the calculating ω_E was

$$\frac{I_{ee}(t_1)}{I_{ee}(t_2)} = \frac{\hat{I}_x \sin(\omega_{E_2} t_1)\cos(0.91\pi) + \hat{I}_y \sin(0.91\pi)}{\hat{I}_x \sin(\omega_{E_2} t_2)\cos(0.91\pi) + \hat{I}_y \sin(0.91\pi)}. \tag{4.11}$$

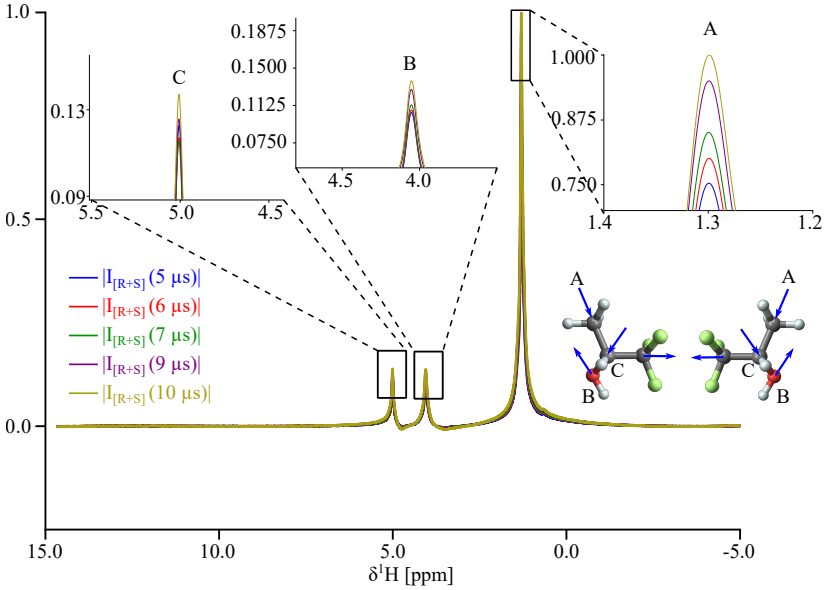

Figure 4.5: ^{1}H NMR spectrum acquired for 1,1,1-trifluoropropan-2-ol close to π pulse length for the racemic sample. The letter labelled on top of the peaks represents the signal from the ^{1}H labelled in the chemical structure. The blue arrows on the chemical structure show the direction of the electric dipoles are not scaled to the actual values. The intensity of the peak labelled **A**, **B**, and **C** increases with increasing pulse lengths of E_2.

The tables 4.4, 4.5, 4.6 shows the results from solving eq. (4.11) for different E_2 pulse lengths. The power applied to the E_2 port was 20 W, the voltage delivered to the port was calculated by using the impedance value from Smith's chart in 3.15 (c) at 500 MHz. The voltage magnitude was 54 V. This resulted in the electric field magnitude of 54 kV m^{-1}. B_0 was 11.74 T, and the γ_r for ^{1}H is 267.522 rad µs^{-1} T^{-1}. Using eq. (2.133) the chiral constant at different frequency shifts was calculated and is shown in the table 4.7. Therefore, from the values calculated in the table 4.7, the σ_c values for ^{1}H is a magnitude of 10 lower than the σ_c value calculated for ^{19}F. In [46] the chirality constant at different positions was calculated for ^{13}C and ^{19}F atoms of 1,1,1-trifluoropropan-2-ol. Due to

Table 4.4: Value of ω_E rad µs^{-1} calculated using the eq. (4.11) for the peak at 1.3 ppm.

Pulse length of E_2	5 µs	6 µs	7 µs	9 µs	10 µs
5 µs	-	-0.0017	-0.0023	-0.0042	-0.0052
6 µs	-0.0017	-	-0.0029	-0.0052	-0.0062
7 µs	-0.0023	-0.0029	-	-0.0064	-0.0075
9 µs	-0.0042	-0.0052	-0.0064	-	-0.01
10 µs	-0.0052	-0.0062	-0.0075	-0.01	-

Table 4.5: Value of ω_E rad µs^{-1} calculated using the eq. (4.11) for the peak at 4.05 ppm.

Pulse length of E_2	5 µs	6 µs	7 µs	9 µs	10 µs
5 µs	-	0.0076	0.0068	0.0044	0.0034
6 µs	0.0076	-	0.0062	0.0057	0.0023
7 µs	0.0068	0.0062	-	0.0019	0.0010
9 µs	0.0044	0.0057	0.0019	-	-0.0012
10 µs	0.0034	0.0023	0.0010	-0.0012	-

the lower natural abundance of ^{13}C, and the inability to use decoupling sequence to enhance the ^{13}C signal due to the single nucleus device, the measurements at ^{13}C could not be recorded. Therefore, comparing the σ_c values is impossible. However, the isotropic component of the nuclear magnetic shielding polarizability tensor $\overline{\sigma^{(1)}}^{(N)}$ (as denoted in [14]), first computed by [14] was found to have a magnitude difference of approximately 10 times between ^{1}H and ^{19}F nuclei. Following this, the calculation for the same tensor by [46] reported in Table 2 had the same order of difference between ^{1}H and ^{19}F. Therefore, the effect of the permanent electric dipole in chiral signals as reported by [46, 51, 63] were not observed or the magnitudes were similar to the isotropic component of the nuclear magnetic shielding polarizability tensor.

Table 4.6: Value of ω_E rad µs^{-1} calculated using the eq. (4.11) for the peak at 5 ppm.

Pulse length of E_2	5 µs	6 µs	7 µs	9 µs	10 µs
5 µs	-	0.01	0.0097	0.0081	0.0072
6 µs	0.01	-	0.0085	0.0072	0.0064
7 µs	0.0097	0.0085	-	0.0066	0.0057
9 µs	0.0081	0.0072	0.0066	-	0.0038
10 µs	0.0072	0.0064	0.0057	0.0038	-

Table 4.7: The average value of σ_c calculated using the eq. (2.133) for all the peaks at different frequency shifts. The other variables in the equation and their values used were, E_2 was 54 kV m^{-1}, with the sample placed in the magnetic field of 11.74 T, and the gyromagnetic ratio of ^{1}H is 267.522 rad µs^{-1} T^{-1}. The σ_c value obtained from ^{1}H spectroscopy is compared to the σ_c value calculated from ^{19}F spectroscopy.

Frequency shift	$\lvert\sigma_c\rvert$
1.3 ppm	6×10^{-11} m V^{-1}
4.05 ppm	4.8×10^{-11} m V^{-1}
5 ppm	8.6×10^{-11} m V^{-1}

4.4 2-(2,6-Dioxo-3-piperidyl)isoindol-1,3-dion (thalidomide or Contergan) using ^{1}H spectroscopy

The next set of molecules which were used for the chiral distinction were the enantiomers of 2-(2,6-Dioxo-3-piperidinyl)-1H-isoindole-1,3(2H)-dione. The molecule is also known as thalidomide or Contergan. It is infamous as one of its enantiomer was found to be teratogenic [23]. This was the motivation to use this chemical for the investigation to explore if it would be possible to distinguish its enantiomers. The samples were the racemic, (S)-, and (R)-. Since thalidomide is a solid powder, it was dissolved in Dimethylsulfoxid-d_6 (DMSO-d_6) with the concentration of 0.113 M.

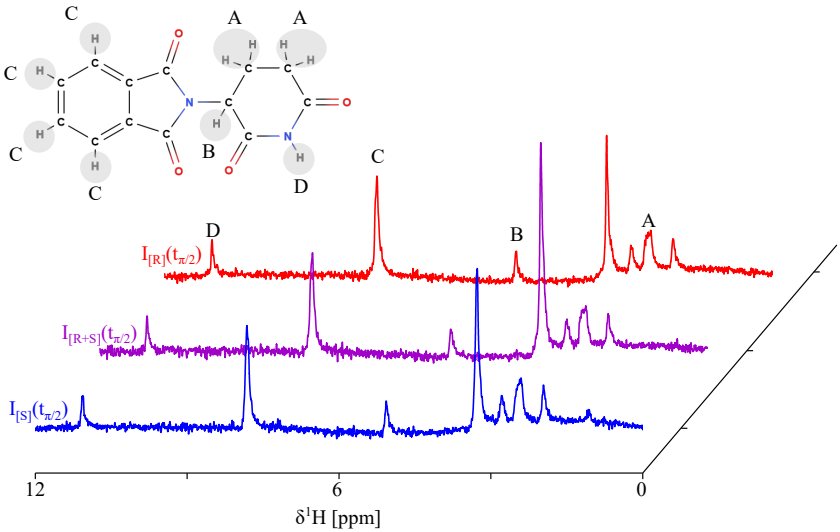

Figure 4.6: Plot of the ^{1}H NMR spectra of (R)-, (S)-, and the racemic of 0.113 M thalidomide in DMSO-d_6 at $\pi/2$ pulse length in the absence of E_2. The ^{1}H labelling on the chemical structure represents the frequency shifts. The frequency shifts were calibrated from the supplementary information in [64]. The peak assignment was referred from [65].

The first steps in the measurements were the conventional NMR-routines, i.e., shimming, frequency shifts alignment, pulse calibrations etc. The fig. 4.6 shows the spectra acquired for all three sample types, and the frequency shifts for different ^{1}H positions. The spectra were recorded with 4 dummy scans, 4 scans with a delay of 5 s between each acquisition.

4.4.1 (R)-2-(2,6-Dioxo-3-piperidyl)isoindol-1,3-dion

The next step in the measurements was similar to the one repeated in 4.3, i.e., applying E_2 fields with different pulse lengths. The pulse program used for the measurements is shown in the listing 4.2. The measurement results are shown in the fig 4.7. As can be seen from the acquisitions the only peak, which showed

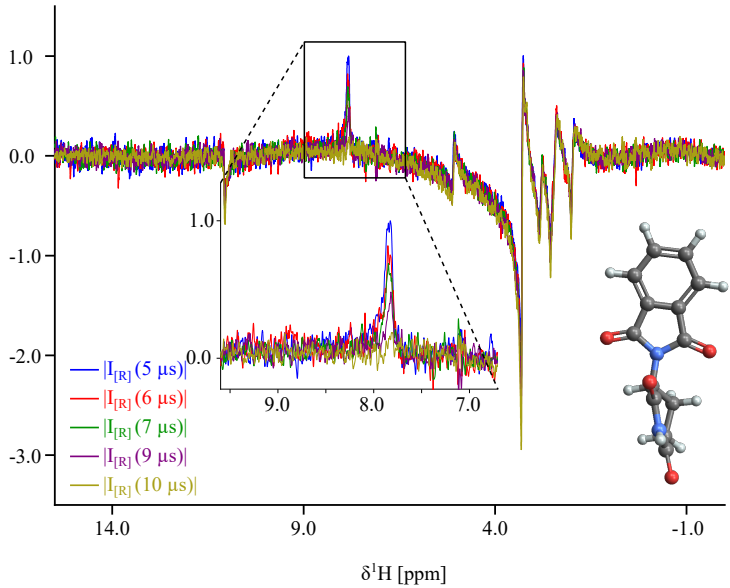

Figure 4.7: ^{1}H NMR spectrum acquired for (R)-thalidomide close to π pulse lengths. Only the peak at 8 ppm showed sensitivity to the varying E_2 pulse lengths. The intensity of this peak is reduced with the increasing pulse lengths of E_2 and reaches almost zero at 10 µs.

a sensitivity to the E_2 fields was the peak at 8 ppm, which is labelled **C** in the spectrum.

4.4.2 (S)-2-(2,6-Dioxo-3-piperidyl)isoindol-1,3-dion

The measurements were then repeated for (S)-. The measurement results are shown in the fig 4.8. Similar to the (R)- measurements, the peak labelled **C** in the spectrum was sensitive to the E_2.

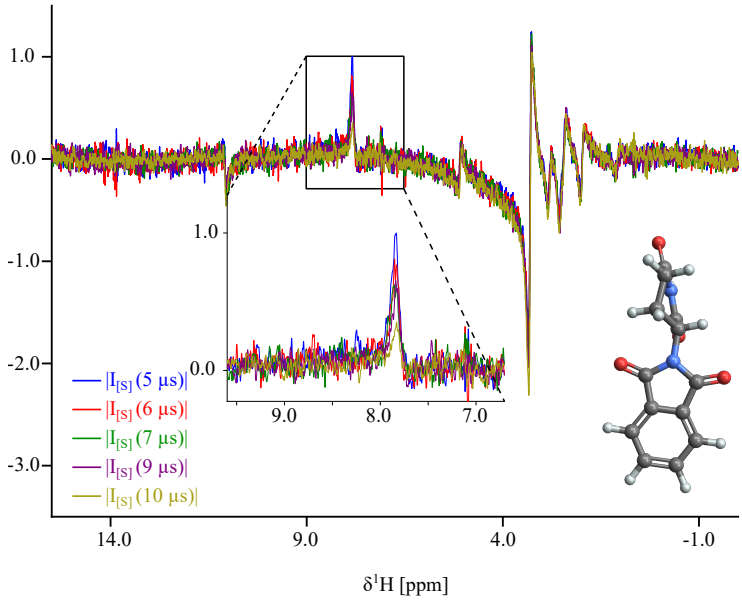

Figure 4.8: ^{1}H NMR spectrum acquired for (S)-thalidomide close to π pulse lengths. Only the peak at 8 ppm showed sensitivity to the varying E_2 pulse lengths. The intensity of this peak is reduced with the increasing pulse lengths of E_2, however, did not reach zero at 10 µs like the (R)-Thalidomid.

4.4.3 Chiral constant calculation for 2-(2,6-Dioxo-3-piperidyl)isoindol-1,3-dion

From the measurement for the (R)-, and (S)- the peak values at 10 µs are different. The reason is that depending on the handedness chiral constant the time taken to reach the effective π flipping will be more for one enantiomer than the other, and the value for the racemic sample should lie between the two. This is also shown in the fig. 4.9, where the spectra plotted are using 10 µs pulse length of E_2 and B_2.

Therefore, to estimate the exact value of the chirality constant, a pulse optimisation algorithm was run, where the pulse length of E_2 was set at 10 µs, and the

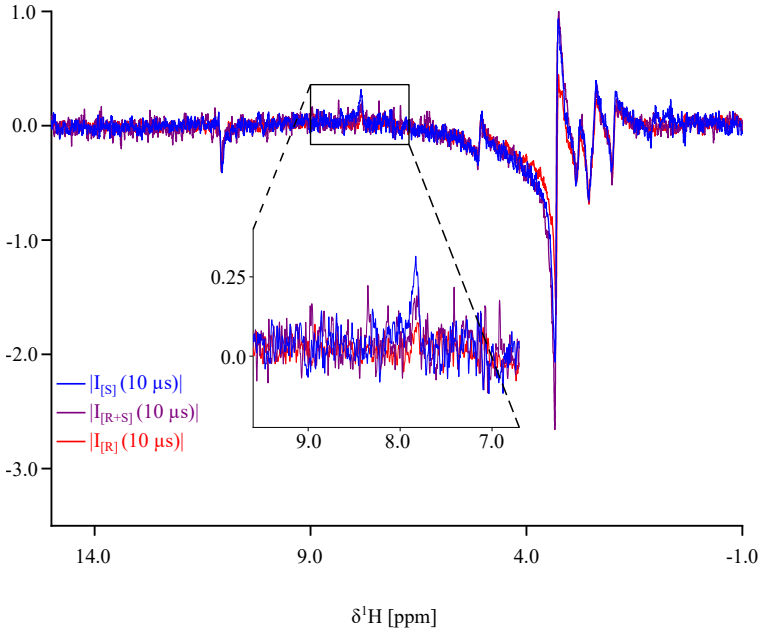

Figure 4.9: ^{1}H NMR spectra comparison for (S)-thalidomide, (R)-thalidomide and racemic for a pulse length of 10 µs for the B_1 and the E_2 port. The signal at 8 ppm was then used to run the pulse calibration to find the exact π-pulse lengths for each sample.

pulse length of B_1 was varied in the steps of 0.25 µs. The π flip values for the three samples measured are shown in fig. 4.9, and the exact values in the table 4.8, which was calculated from the nutation plot shown in the fig. A.4.

Table 4.8: π-pulse length values measured for different samples, with an E_2 pulse length 10 µs. The power used to excite the B_1 and E_2 ports was 20 W.

Sample	pulse length
(R)-	9.875 µs
racemic	10.0 µs
(S)-	10.25 µs

Since σ_c for a racemic mixture should cancel each other out, therefore, simplifying eq. (2.159) results in

$$I_{\text{racemic}} = \hat{I}_y \sin \omega_{B_1} t_1. \tag{4.12}$$

Using the value of π pulse length from the table 4.8 in the eq. (4.12)

$$\omega_{B_1} = \frac{\pi}{10}. \tag{4.13}$$

With the value of ω_{B_1}, and the π pulse length we can calculate the electrical nutation frequencies, which are

$$\hat{I}_x \sin(\omega_{E_2} 10) \cos(\frac{9.875\pi}{10}) + \hat{I}_y \sin(\frac{9.875\pi}{10}) = 0, \text{for (R)-}, \tag{4.14}$$

$$\hat{I}_x \sin(\omega_{E_2} 10.25) \cos(\frac{10.25\pi}{10}) + \hat{I}_y \sin(\frac{10.25\pi}{10}) = 0, \text{for (S)-}. \tag{4.15}$$

The value of the ω_{E_2} on solving the above two equations was $0.0039\,\text{rad}\,\mu\text{s}^{-1}$ for (R)-enantiomer, and $-0.0078\,\text{rad}\,\mu\text{s}^{-1}$ for (S)-enantiomer. The value of σ_c was calculated using the eq. (2.133). The other variables in the equation and their values used were, E_2 was $54\,\text{kV}\,\text{m}^{-1}$, with the sample placed in the magnetic field of 11.74 T, and the gyromagnetic ratio of ^{1}H is $267.522\,\text{rad}\,\mu\text{s}^{-1}\,\text{T}^{-1}$. This resulted in σ_c of $4.6 \times 10^{-11}\,\text{m}\,\text{V}^{-1}$ and $-9.2 \times 10^{-11}\,\text{m}\,\text{V}^{-1}$ for (R)- and (S)-enantiomers respectively.

The difference in the chirality tensor can be explained by the fact that the enantiomer went under racemisation over time. For thalidomide it is now a well-documented process where the (R)-enantiomer converts to the (S)-enantiomer [66]. However, since the sample were stored in a sealed capillaries, it may have slowed down the conversion process due to which an enantiomeric excess of (R)- still shows a deviation from the racemic.

4.5 2-(4-(2-methylpropyl)phenyl)propanoic acid (ibuprofen) using ^{1}H spectroscopy

The next molecule tested was ibuprofen, an easily available over-the-counter drug. Ibuprofen is used as a non-steroidal anti-inflammatory medicine (NSAIM) [67]. The (S)-enantiomer has a therapeutic effect, and the (R)-enantiomer, though non-toxic, has no beneficiary effect on human body. The salts were mixed in $CDCl_3$ with a molar concentration of 0.5 M, where the racemic was self-prepared by mixing 50:50 by weight of (R)-, and (S)-.
The first set of measurements were the routine NMR experiments to shim the system, calibrate the pulse lengths, and adjust the receiver gain. Figure 4.10 shows the acquired spectra for the (R)-ibuprofen,(S)-ibuprofen and the racemic of ibuprofen at $\pi/2$-pulse lengths.

4.5.1 (R)-2-(4-(2-methylpropyl)phenyl)propanoic acid

The next steps in the measurements were similar to the one repeated in 4.3, i.e., applying E_2 fields with different pulse lengths. The pulse program used for the measurements is shown in listing 4.2. The measurement results are shown in the fig 4.11. The spectra were plotted without any phase correction applied. Only the peak at 1.48 ppm (peak labelled **B**) was examined as this was at the chiral centre. As can be seen from the image, with increasing pulse of the E_2, the spectrum intensity increased. However, since E_2 has some stray field, the spectrum intensity should have decreased since the π flipping of the magnetisation was found to be at 11.7 µs for the B_1 at E_2 pulse length of 10 µs. Therefore, each spectrum recorded at a pulse length lower than 10 µs should have increased the signal intensity. This meant that the chiral tensor deferred the net magnetisation flipping.

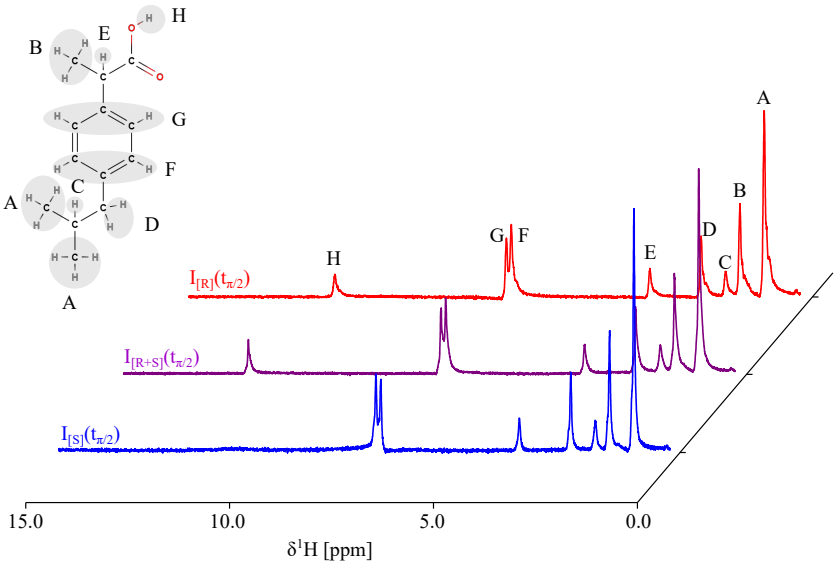

Figure 4.10: Plot of the ^{1}H NMR spectra of (R)-, (S)-, and the racemic of 0.5 M ibuprofen in $CDCl_3$ at $\pi/2$ pulse length in the absence of E_2. The ^{1}H labelling on the chemical structure represents the frequency shifts.

4.5.2 (S)-2-(4-(2-methylpropyl)phenyl)propanoic acid

Similar to thalidomide, the measurements were repeated for (S)-enantiomer. The measurement results are plotted in fig 4.12, without any phase corrections. Also for these measurements only the peak at 1.48 ppm (peak labelled **B**) was examined. In these measurements, with the increasing E_2 pulse length, no intensity variations were observed. This variation can be explained by the fact that the π flipping of the magnetisation was found to be at 10.85 µs for the B_1 at E_2 pulse length of 10 µs. This value was close to the value found for the racemic sample which was 11 µs. This meant that even though the electric field variation affected the chiral tensor, it was not strong enough and if there were no electric field applied the π flip should be close to the 11 µs mark. Therefore, for E_2 pulse lengths from 5 µs to 9 µs there is no intensity variation observed, and for the pulse length

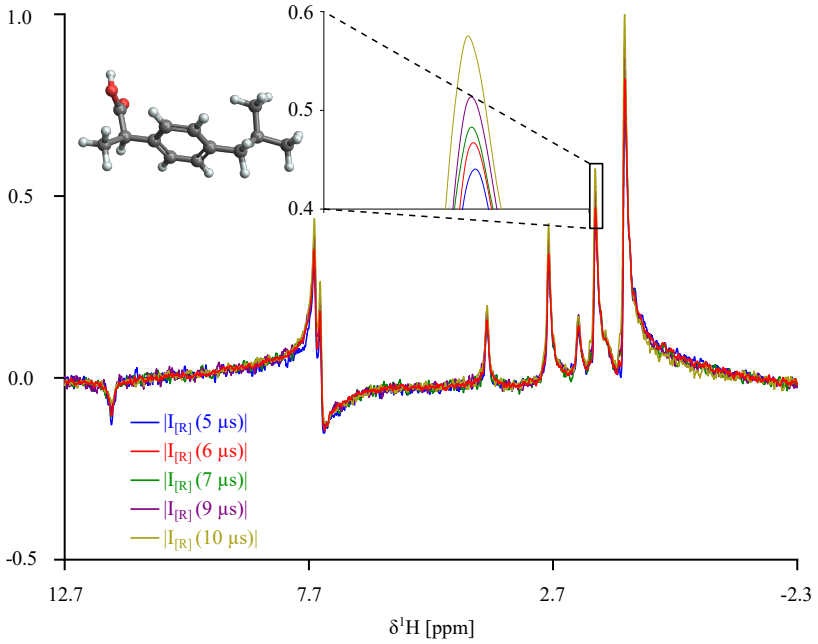

Figure 4.11: ^{1}H NMR spectrum acquired for (R)-ibuprofen. Only the peak at 1.48 ppm was observed for analysis. The intensity of all the peaks increased with the increasing pulse lengths of E_2.

10 µs the intensity increases. This spectrum if plotted with phase correction will be inverted relative to the other peaks.

4.5.3 chiral constant calculation for 2-(4-(2-methylpropyl)phenyl)propanoic acid

The measurement result comparison amongst the (R)-,(S)-, and the racemic for different E_2 pulse lengths showed different behaviour. This can be due to the fact that the duration of the π-pulse lengths were different as compared to the thalidomide experiments, which indicates different chiral coupling strengths. The (R)-

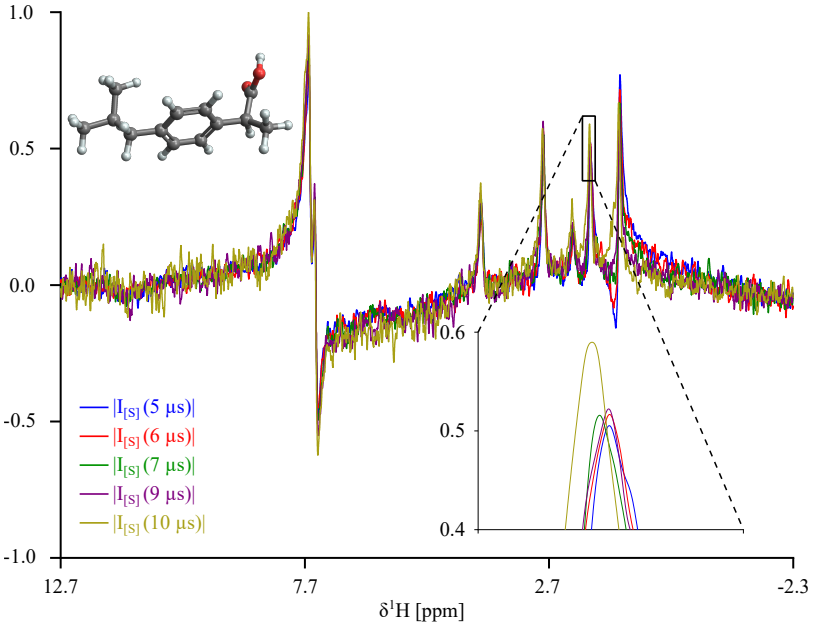

Figure 4.12: ^{1}H NMR spectrum acquired for (S)-ibuprofen close to π pulse lengths. Only the peak at 1.48 ppm was used for analysis as varying E_2 pulse lengths had different effects on each frequency shift. The intensity of this peak remained unaffected with the increasing pulse lengths of E_2, however, did not increase uniformly like the (R)-ibuprofen.

enantiomer was found to be more sensitive to changes than the (S)-enantiomer. Table 4.9 shows the pulse length required on the B_1 port, where the pulse length of the E_2 port was kept constant at 10 µs. The power applied to both the ports was kept constant at 20 W. The pulse lengths were measured for the peak labelled with a frequency shift of 1.48 ppm. As can be seen from the table above, the (R) had a larger difference from the racemic, as compared to the (S) enantiomer. To

Table 4.9: π-pulse length values measured for different samples, with an E_2 pulse length 10 µs. The power used to excite the B_1 and E_2 ports was 20 W.

Sample	pulse length
(R)-	11.5 µs
racemic	11 µs
(S)-	10.85 µs

calculate the chiral constant (σ_c), we use the same method as for the thalidomide. There using eq. (4.12), and table 4.9

$$\omega_{B_1} = \frac{\pi}{11}. \tag{4.16}$$

Therefore,

$$\hat{I}_x \sin(\omega_{E_2} 10) \cos(\frac{10.85\pi}{11}) + \hat{I}_y \sin(\frac{10.85\pi}{11}) = 0, \text{for (S)-}, \tag{4.17}$$

$$\hat{I}_x \sin(\omega_{E_2} 10) \cos(\frac{11.5\pi}{11}) + \hat{I}_y \sin(\frac{11.5\pi}{11}) = 0, \text{for (R)-}. \tag{4.18}$$

The value of the ω_{E_2} on solving the above two equations was $-0.014\,\mathrm{rad\,\mu s^{-1}}$ for (R) and $0.0042\,\mathrm{rad\,\mu s^{-1}}$ for (S). The value of σ_c was calculated using the eq. (2.133). The other variables in the equation and their values used were, E_2 was $54\,\mathrm{kV\,m^{-1}}$, with the sample placed in the magnetic field of 11.74 T, and the gyromagnetic ratio of ^{1}H is $267.522\,\mathrm{rad\,\mu s^{-1}\,T^{-1}}$. This resulted in σ_c of $-1.65 \times 10^{-10}\,\mathrm{m\,V^{-1}}$ for (R)- and $4.89 \times 10^{-11}\,\mathrm{m\,V^{-1}}$ for (S)-. The difference in the value of the chirality constant could be due to the (S)-enantiomer going under structural change as certain conformers of ibuprofen are preferred in a solution of $CDCl_3$ as shown by [68]. The quality report from the supplier shows that the peak around 12 ppm from the carboxyl group should not be present for the (S)-enantiomer [69]. However, it was observed over time that the peak started to

appear as shown in fig. A.5. This may have altered the electric dipole interaction and the difference in the chirality constant measured.

5 Conclusions and future outlook

5.1 Conclusion

This dissertation deals with the invention of a detector and methods which made direct chirality distinction in NMR possible. It started with the explanation of the NMR and its Hamiltonian. Using the NMR Hamiltonian, the evolution of the magnetisation during conventional NMR routine was described mathematically. The explanation was used for deriving a NMR Hamiltonian with the chiral coupling tensor. The difference to a conventional Hamiltonian was an odd-parity term σ_c included in it. The chiral NMR Hamiltonian was then transformed from a laboratory to a rotating frame of reference. The transformation enabled the derivation for the evolution of the magnetisation coupled with the σ_c tensor, which led to three scenarios:

- flipping of the magnetisation by an arbitrary angle but close to π,
- flipping of the magnetisation by $\pi/2$,
- flipping of the magnetisation by π.

From these possibilities, it was shown that the chiral signal vanishes for the second case, i.e., when the magnetisation is flipped by $\pi/2$. It was also shown that the chiral signal will be the strongest when the magnetisation flip angle is exactly π. Based on the theory established we started with the design of the detector.
The first series of detector designs were based on the ring loop resonator presented by [54]. The design had its limitations, mainly the placement of a magnetic moment-sensitive transponder. This was due to the size of the detector. Hence, an improvement to the design was suggested, which was the miniaturised version of the ring loop resonator. It fulfilled all the requirements for chiral detec-

tion and could have fit inside a 10 mm saddle coil. However, a method to excite the resonator remained unresolved, as the magnitude of E_2 required was in the order of kV, which would have been difficult to achieve using an energy coupler. This led to the evolution of the second design series, which was the active ring loop resonator. The design of the resonator and its functioning was similar to the ones described above, in addition, it had an excitation port to achieve the required E_2 magnitudes. The resonator was placed between the magnetic detector and a spectrum was recorded, but the spectrum did not have a sufficient SNR. The reason was due to the low-filling factor of the coil. This was the last design tried with ring loop resonators, and the next designs were based on the microstrips.
The microstrip-based detector was designed to have a target k-value ($< 10^{-4}$) [46, 54]. This was to be achieved by switching between B_1 and E_2 ports during the detector's excitation and detection phase. As maintaining the k-value volume when placing material with different dielectric constants and fast switching between the circuits was technically challenging the detector design was abandoned.
The final design, which led to successful signal detection was based on the microstrip design. The improvement to all the previous approaches was that it had independent control of the E_2 and B_1. This helped to overcome the issue of maintaining a detection-sensitive region ($k < 10^{-4}$), which was influenced by the mismatch of dielectric constants making sample placement challenging. The flexibility of independently controlling E_2 and B_1, allowed inversion of the magnetisation by a π-RF pulse and simultaneously applying a E_2 on larger volumes as compared to ring loop resonators. As the SNR depends directly on the sample volume, this directly helped in solving the sensitivity challenges. Therefore, the detector design has all the features required for chiral signal detection, i.e., it could apply high-magnitude E_2, detect oscillating magnetic dipoles, accommodate large sample volumes, and flexibly handle pulse sequences for signal enhancement.
With this detector, we were able to distinguish chiral molecules. The measurements were recorded for three chiral molecules which were,

- **1,1,1-trifluoropropan-2-ol**: The chiral signal were recorded using ^{19}F, and ^{1}H spectroscopy. The magnitude of the chirality tensor was calculated to be larger than what was previously predicted by [14,46]. Though the ratio of chirality tensor of ^{19}F, and ^{1}H were in the same order of magnitudes as calculated by [14].
- **2-(2,6-Dioxo-3-piperidyl)isoindol-1,3-dion (thalidomide)**: The next molecule chosen was thalidomide. From the measurement results it was shown that it was possible to distinguish its enantiomers, however, it was observed that (R)-enantiomer may have undergone racemisation. This phenomenon is a known physical effect which led to the infamous thalidomide scandal.
- **2-(4-(2-methylpropyl)phenyl)propanoic acid (ibuprofen)**: ibuprofen was chosen for the next tests as it is one of the widely known NSAIM, where only one of the enantiomer is effective. The measurement results showed a difference in the chiraliy constant for the (R)- and the (S)-enantiomers. The reason for this could be due to the structural changes in the (S)-enantiomer, where one conformed is preferred over the other. This may have led to a change in the chiral tensor which correlates the spin-electric dipole coupling.

5.2 Future works

The detector developed in this dissertation allowed for the first time the direct distinction of enantiomers in NMR. The function of the detector was proven with three different molecules. However, there are some important aspects which still need to be studied, investigated and developed. Some of these points are:

- **Pulse sequence**: The pulse sequence used can be considered as a basic one, which would be analogous to the NMR sequence with a single hard RF pulse. A routine needs to be developed which would help in enhancing the chiral signal.

- **Pulse optimisation**: Similar to a multi-spin system, we have a bi-dipole system, i.e., investigation of coupling between electric and magnetic dipole moment. Therefore, similar to pulse sequences like INEPT [70] it should be possible to optimise the pulse to enhance only the signal obtained from the chiral centre.
- **Detection method optimisation**: The gradients were not used as the space limitation did not allow its integration. Another improvement to the detection method could be the use of gradients. They help to create a de-phasing and refocusing of the spins. If we assume that the coupling between the spins and electric dipole have different diffusion coefficients than a non-chiral spins we may have a chance to saturate the non-chiral spin and observe only the signal due to chirality.
- **Detector optimisation**: It was shown by [4] (List of Own Publications, Journal articles) that it is possible to optimise a detector to enhance the magnetic field topologically. Following the same principle by tweaking the target function it may be possible to design a chiral-detector, which has the function of enhancing the chiral signal. One approach could be to enhance E_2, while minimising B_1. Therefore, the detection scheme followed will be similar to the one described for the ring loop resonators.
- **Study of different molecules and nuclei**: Within the scope of the dissertation, to prove the theory and the functioning of the detectors the molecule, 1,1,1-trifluoropropan-2-ol, suggested by [46, 54] to have the strongest chiral signal was measured. This was followed by two other molecules; thalidomide and ibuprofen. From the measurements and calculations, it was found that the chirality tensor is several orders of magnitudes higher than reported by [46]. This creates a hope that it may be possible to observe chiral signals for other molecules, and even for nuclei other than ^{19}F and ^{1}H. The interesting nuclei to be investigated would be ^{13}C and ^{15}N, which are the building blocks for amino acids. This would help to study

the interaction between chiral-based drugs and proteins to make drug use safe and avoid another thalidomide-like misjudgment.

- **Chiral detection in solid-state NMR:** The chiral detection theory proposed by A.D. Buckingham, and presented in this dissertation is for the liquid-state NMR. However, it was observed by [71] that the magnitude of signal acquired for different enantiomers were different. The author concluded the effect to CISS (chiral induced spin-selectivity). Therefore, it may be possible to probe the enantiomers in solid-state using the detector presented, and an appropriate pulse-sequence.

A Appendix

A.1 Laser parameters

The parameters given were found using UV-source laser Pirhana from ACSYS, Germany.

Table A.1: Laser cutting parameter for copper (Cu) plate of 500 µm thick and borosilicate glass (MEMpax from Schott AG) of thickness 500 µm. The laser repetition rate used was 20 kHz with pulse width of 1.2 µs and cutting speed of 100 mm s^{-1}. The laser power was set to 80% of the total output power, which resulted in 2.4 W.

Material	Line spacing (µm)	No. of lines	No. of receptions
Cu	5	35	50
Fused Silica glass	10	10	12

A.2 Technical drawings for active ring loop resonator

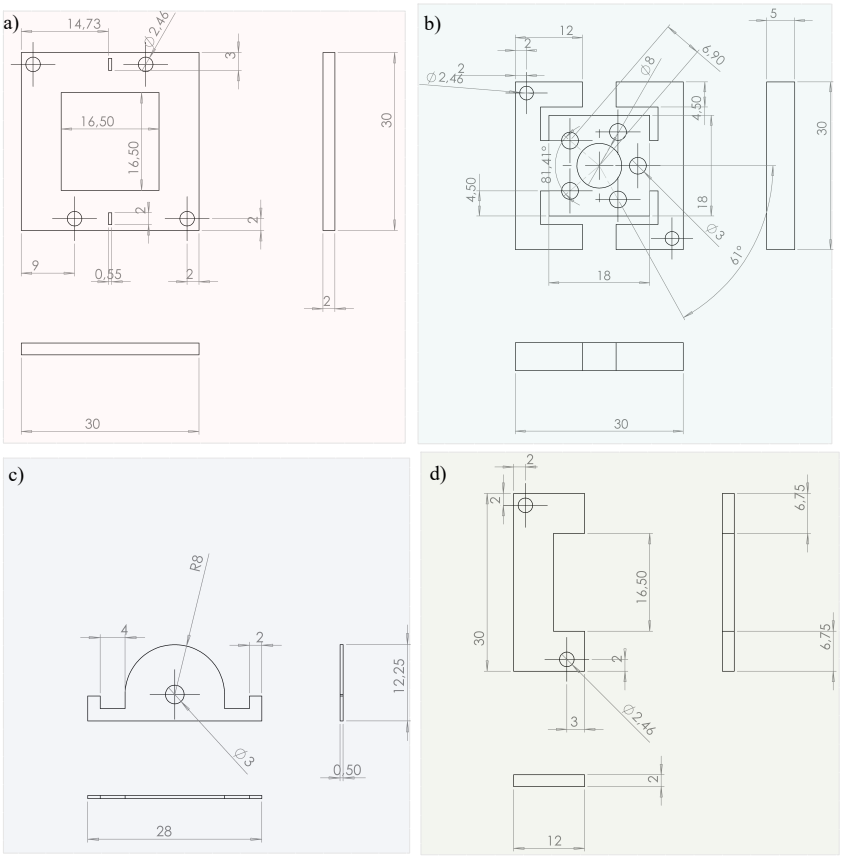

Figure A.1: Technical drawings for the components used to mount the active ring loop resonator on Micro5 probe head from Bruker, Germany. (a) The top plate where the detector and the sample holder are mounted. (b) The bottom plate is the interface between the probe head and the detector's assembly. (c) The sample holder. (d) The spacer disk was used to align the centre of the active ring loop centre to the iso-centre of the magnet.

A.3 NMR spectrum plots

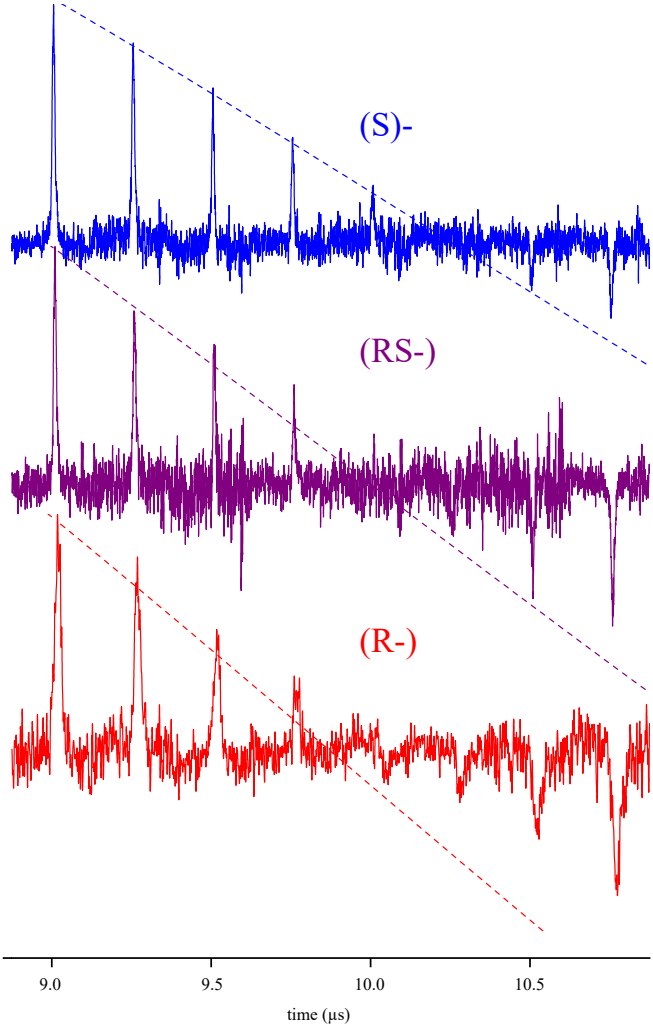

Figure A.2: Nutation spectra of different enantiomers and racemic of thalidomide. The parameter search was performed by keeping the E_2 magnitude and pulse length constant at 20 W, and 10 µs respectively, and varying the B_1 pulse length from 10 µs to 12 µs in the steps of 0.25 µs. The power on the B_1 port was kept constant at 20 W.The dotted line represents the curve plotted from the equation (4.1), with the values used from the measurement results to show the exact point at which the curve reaches zero signal intensity.

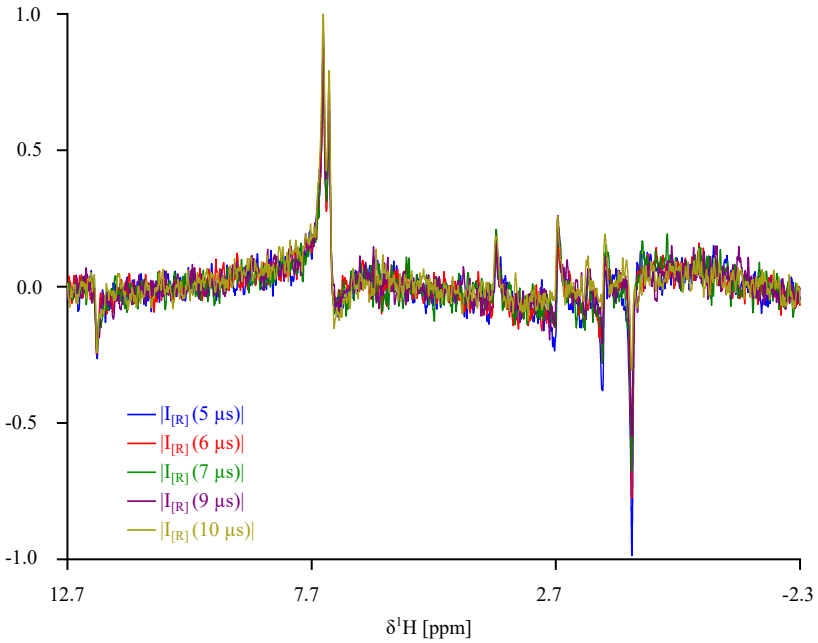

Figure A.3: ^{1}H NMR spectrum acquired for racemate ibuprofen. Only the peak at 1.48 ppm was observed for analysis. The intensity of all the peaks decreased with the increasing pulse lengths of E_2.

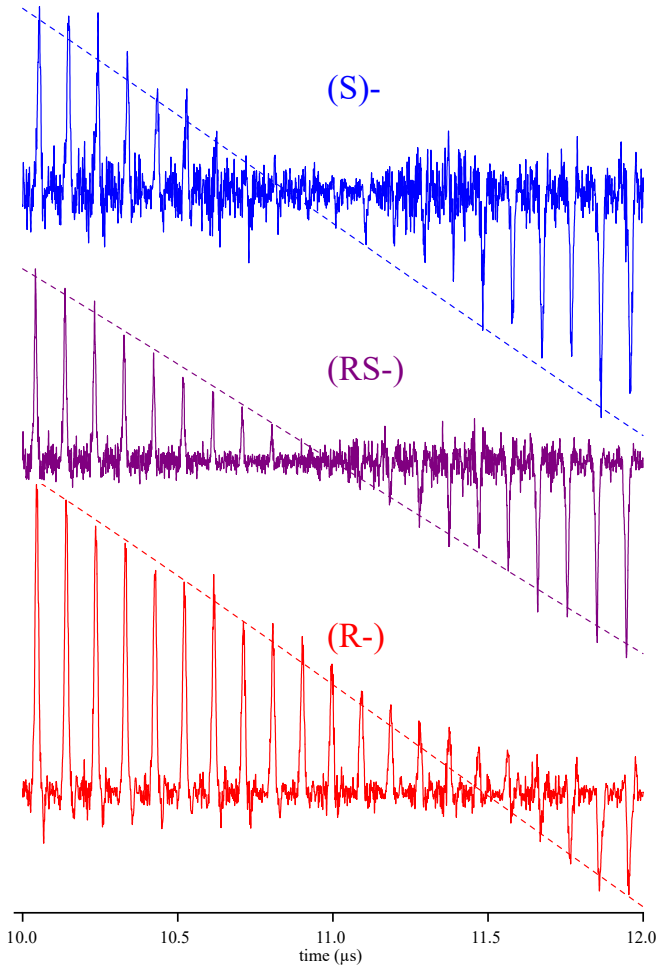

Figure A.4: Nutation spectra of different enantiomers and racemic of ibuprofen. The parameter search was performed by keeping the E_2 magnitude and pulse length constant at 20 W, and 10 µs respectively, and varying the B_1 pulse length from 10 µs to 12 µs in the steps of 0.1 µs. The power on the B_1 port was kept constant at 20 W. The dotted line represents the curve plotted from the equation (4.1), with the values used from the measurement results to show the exact point at which the curve reaches zero signal intensity.

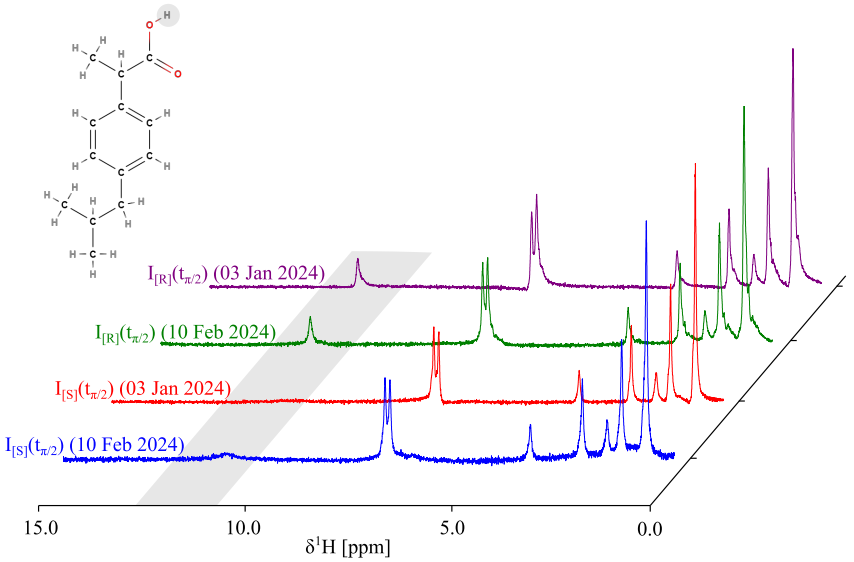

Figure A.5: ^{1}H NMR spectra of (R)-, (S)-, of 0.5 M ibuprofen in $CDCl_3$at $\pi/2$ pulse length in the absence of E_2 recorded on the date mentioned in the figure. The ^{1}H highlighted on the chemical structure is on the carboxyl group. It was observed that after a certain time duration, the signal from this particular ^{1}H in (S)- started to appear, whereas it was not present in the initial measurements. According to the manufacturer's datasheet, for the (S)-, the ^{1}H at this site should be silent [69].

List of Figures

List of Tables

List of Own Publications

Journal articles

[1] E. R. Mamleyev, F. Falk, P. G. Weidler, S. Heissler, S. Wadhwa, O. Nassar, C. N. Shyam Kumar, C. Kübel, C. Wöll, M. Islam, D. Mager, and J. G. Korvink. Polyaramid-Based Flexible Antibacterial Coatings Fabricated Using Laser-Induced Carbonization and Copper Electroplating. *ACS Applied Materials & Interfaces*, 12(47):53193–53205, 2020.

[2] O. Nassar, M. V. Meissner, S. Wadhwa, J. G. Korvink, and D. Mager. Load Sensitive Stable Surrent Source for Complex Precision Pulsed Electroplating. *Review of Scientific Instruments*, 90(10):104704, 2019.

[3] S. Wadhwa, D. Buyens, and J. G. Korvink. Direct chiral discrimination with NMR. (submitted).

[4] S. Wadhwa, M. Jouda, Y. Deng, O. Nassar, D. Mager, and J. G. Korvink. Topologically Optimized Magnetic Lens for Magnetic Resonance Applications. *Magnetic Resonance*, 1(2):225–236, 2020.

Conference contributions

[1] V. Vlnieska, A. Voigt, S. Wadhwa, J. Korvink, M. Kohl, and K. Poletkin, "Development of control circuit for inductive levitation micro-actuators," in *Proceedings*, vol. 64, MDPI, 2020.

[2] S. Wadhwa, M. Jouda, Y. Deng, D. Mager, and J. Korvink, "Topologically optimized magnetic lens alters helmholtz coil field to produce B1 gradient

with field amplification," Experimental Nuclear Magnetic Resonance Conference, 2021.

[3] M. Bastawrous, R. G. Biswas, R. Soong, S. Wadhwa, N. Mackinnon, M. Jouda, D. Mager, J. Korvink, and A. Simpson, "Integrating paramagnetic lenses and cryoprobe: a powerful tool for environmental monitoring," in *Proceedings of the 18th NMR users meeting*, Galoá, 2021.

Bibliography

[1] I. I. Rabi, J. R. Zacharias, S. Millman, and P. Kusch, "A New Method of Measuring Nuclear Magnetic Moment," *Phys. Rev.*, vol. 53, no. 4, pp. 318–318, 1938.

[2] G. Bodenhausen and D. J. Ruben, "Natural abundance nitrogen-15 NMR by enhanced heteronuclear spectroscopy," *Chemical Physics Letters*, vol. 69, no. 1, pp. 185–189, 1980.

[3] M. Piotto, V. Saudek, and V. Sklenář, "Gradient-tailored excitation for single-quantum NMR spectroscopy of aqueous solutions," *Journal of biomolecular NMR*, vol. 2, no. 6, pp. 661–665, 1992.

[4] V. Sklenar, M. Piotto, R. Leppik, and V. Saudek, "Gradient-Tailored Water Suppression for 1H-15N HSQC Experiments Optimized to Retain Full Sensitivity," *Journal of Magnetic Resonance, Series A*, vol. 102, no. 2, pp. 241–245, 1993.

[5] K. Nagayama, A. Kumar, K. W. thrich, and R. Ernst, "Experimental techniques of two-dimensional correlated spectroscopy," *Journal of Magnetic Resonance (1969)*, vol. 40, no. 2, pp. 321–334, 1980.

[6] A. D. Gossert and W. Jahnke, "NMR in drug discovery: A practical guide to identification and validation of ligands interacting with biological macromolecules," *Progress in Nuclear Magnetic Resonance Spectroscopy*, vol. 97, pp. 82–125, 2016.

[7] C. M. Thiele, “Residual Dipolar Couplings (RDCs) in Organic Structure Determination,” *European Journal of Organic Chemistry*, vol. 2008, no. 34, pp. 5673–5685, 2008.

[8] G. Kummerlöwe and B. Luy, “Residual dipolar couplings as a tool for the structure determination of organic molecules,” *Trends in Analytical Chemistry*, vol. 28, no. 4, pp. 483–493, 2009.

[9] D. Parker, “NMR determination of enantiomeric purity,” *Chemical Reviews*, vol. 91, no. 7, pp. 1441–1457, 1991.

[10] T. J. Wenzel and C. D. Chisholm, “Assignment of Absolute Configuration using Chiral Reagents and NMR Spectroscopy,” *Chirality*, vol. 23, no. 3, pp. 190–214, 2011.

[11] H. Duddeck and E. D. Gomez, “Chiral recognition of ethers by NMR spectroscopy,” *Chirality*, vol. 21, no. 1, pp. 51–68, 2009.

[12] R. Schwenninger, J. Schlögl, J. Maynollo, K. Gruber, P. Ochsenbein, H.-B. Bürgi, R. Konrat, and B. Kräutler, “Metal Complexes of a Biconcave Porphyrin with D4-Structure-Versatile Chiral Shift Agents,” *Chemistry - A European Journal*, vol. 7, no. 12, pp. 2676–2686, 2001.

[13] A. D. Buckingham, “Chirality in NMR spectroscopy,” *Chemical Physics Letters*, vol. 398, no. 1-3, pp. 1–5, 2004.

[14] A. D. Buckingham and P. Fischer, “Direct chiral discrimination in NMR spectroscopy,” *Chemical Physics*, vol. 324, no. 1, pp. 111–116, 2006.

[15] W. Kelvin, *The Molecular Tactics of a Crystal*. Boyle lecture, Clarendon Press, 1894. ISBN 1163958557.

[16] A.-J. Fresnel and G. R. Putland (tr. /ed.), “Memoir on the double refraction that light rays undergo in traversing the needles of quartz in the directions parallel to the axis,” 2021.

[17] M. Laska, A. Liesen, and P. Teubner, "Enantioselectivity of odor perception in squirrels, monkeys and humans," *American Journal of Physiology-Regulatory, Integrative and Comparative Physiology*, vol. 277, no. 4, pp. R1098–R1103, 1999.

[18] J. C. Brookes, A. Horsfield, and A. Stoneham, "Odour character differences for enantiomers correlate with molecular flexibility," *Journal of The Royal Society Interface*, vol. 6, no. 30, pp. 75–86, 2009.

[19] T. J. Leitereg, D. G. Guadagni, J. Harris, T. R. Mon, and R. Teranishi, "Chemical and sensory data supporting the difference between the odors of the enantiomeric carvones," *Journal of Agricultural and Food Chemistry*, vol. 19, no. 4, pp. 785–787, 1971.

[20] M. Inaki, J. Liu, and K. Matsuno, "Cell chirality: its origin and roles in left-right asymmetric development," *Philosophical Transactions of the Royal Society B: Biological Sciences*, vol. 371, no. 1710, p. 20150403, 2016.

[21] L. A. Nguyen, H. He, and C. Pham-Huy, "Chiral drugs: an overview," *International journal of biomedical science : IJBS*, vol. 2, no. 2, pp. 85–100, 2006.

[22] I. P. Silvestri and P. J. J. Colbon, "The Growing Importance of Chirality in 3D Chemical Space Exploration and Modern Drug Discovery Approaches for Hit-ID," *ACS Medicinal Chemistry Letters*, vol. 12, no. 8, pp. 1220–1229, 2021.

[23] N. Vargesson, "Thalidomide-Induced Teratogenesis: History and Mechanisms," *Birth Defects Res C Embryo Today*, vol. 105, no. 2, pp. 140–156, 2015.

[24] N. Vargesson, "The Teratogenic Effects of Thalidomide on Limbs," *J Hand Surg Eur Vol*, vol. 44, no. 1, pp. 88–95, 2018.

[25] W. Song and S. Si, "The Rare Ethambutol-Induced Optic Neuropathy: A Case-Report and Literature Review," *Medicine (Baltimore)*, vol. 96, no. 2, p. e5889, 2017.

[26] Y. Zhao, A. N. Askarpour, L. Sun, J. Shi, X. Li, and A. Alù, "Chirality Detection of Enantiomers using Twisted Optical Metamaterials," *Nature Communications*, vol. 8, no. 1, p. 14180, 2017.

[27] K. Yao and Y. Liu, "Enhancing Circular Dichroism by Chiral Hotspots in Silicon Nanocube Dimers," *Nanoscale*, vol. 10, no. 18, pp. 8779–8786, 2018.

[28] S. Zhu and M. Sun, "Electronic Circular Dichroism and Raman Optical Activity: Principle and Applications," *Applied Spectroscopy Reviews*, vol. 56, no. 7, pp. 553–587, 2020.

[29] L. D. Barron and A. D. Buckingham, "Raman Optical Activity of Bromocamphor Solutions," *Journal of the Chemical Society, Chemical Communications*, no. 24, pp. 1028–1029, 1974.

[30] L. D. Barron, L. Hecht, I. H. McColl, and E. W. Blanch, "Raman Optical Activity Comes of Age," *Molecular Physics*, vol. 102, no. 8, pp. 731–744, 2004.

[31] H. Kong, X. Sun, L. Yang, X. Liu, H. Yang, and R.-H. Jin, "Chirality Detection by Raman Spectroscopy: The Case of Enantioselective Interactions between Amino Acids and Polymer-Modified Chiral Silica," *Analytical Chemistry*, vol. 92, no. 21, pp. 14292–14296, 2020.

[32] G. Blaschke, H. P. Kraft, K. Fickentscher, and F. Kohler, "Chromatographic Separation of Racemic Thalidomide and Teratogenic Activity of its Enantiomers.," *Arzneim.-Forsch.*, vol. 29, pp. 1640–1642, 1979.

[33] T. J. Wenzel, *Differentiation of Chiral Compounds Using NMR Spectroscopy*. John Wiley Sons, Ltd, 2018. ISBN 9781119323914.

[34] W. P. Aue, E. Bartholdi, and R. R. Ernst, "Two−Dimensional Spectroscopy. Application to Nuclear Magnetic Resonance," *The Journal of Chemical Physics*, vol. 64, no. 5, pp. 2229–2246, 2008.

[35] M. D. Herbst and J. Goldstein, "A Review of Water Diffusion Measurement by NMR in Human Red Blood Cells," *American Journal of Physiology-Cell Physiology*, vol. 256, no. 5, pp. C1097–C1104, 1989.

[36] J. H. Noggle and R. E. Schirmer, "CHAPTER 8 - Applications of the Nucelar Overhauser Effect: A Review of the Literature," in *The Nuclear Overhauser Effect*, pp. 167–225, Academic Press, 1971. ISBN 9780125206501.

[37] P. Atkins and R. Friedman, *Molecular Quantum Mechanics*. OUP Oxford, 2011. ISBN 0199541426.

[38] M. H. Levitt, *Spin Dynamics - Basics of Nuclear Magnetic Resonance*. New York: Wiley, 2nd ed., 2008. ISBN 0470511176.

[39] J. Keeler, *Understanding NMR Spectroscopy*. New York: John Wiley and Sons, 2nd ed., 2011. ISBN 0470746084.

[40] D. J. Griffiths, *Introduction to Quantum Mechanics*. Cambridge, England: Cambridge University Press, 2 ed., 2016. ISBN 0131244051.

[41] H.-P. Breuer and F. Petruccione, *The Theory of Open Quantum Systems*. London, England: Oxford University Press, 2002. ISBN 0199213909.

[42] R. M. Wilcox, "Exponential Operators and Parameter Differentiation in Quantum Physics," *Journal of Mathematical Physics*, vol. 8, pp. 962–982, 04 1967.

[43] E. Frankel, "Corpuscular Optics and the Wave Theory of Light: The Science and Politics of a Revolution in Physics," *Social Studies of Science*, vol. 6, no. 2, pp. 147–154, 1976.

[44] T. Sleator, E. Hahn, M. B. Heaney, C. Hilbert, and J. Clarke, "Nuclear-Quadrupole Induction of Atomic Polarization," *Physical Review B*, vol. 38, no. 13, pp. 8609 – 8624, 1988.

[45] J. D. Walls and R. A. Harris, "Measuring Chirality in NMR in the Presence of a Time-Dependent Electric Field," *The Journal of Chemical Physics*, vol. 140, no. 23, p. 234201, 2014.

[46] P. Garbacz, J. Cukras, and M. Jaszunski, "A Theoretical Study of Potentially Observable Chirality-Sensitive NMR Effects in Molecules," *Phys. Chem. Chem. Phys.*, vol. 17, no. 35, pp. 22642–22651, 2015.

[47] N. Spengler, J. Höfflin, A. Moazenzadeh, D. Mager, N. MacKinnon, V. Badilita, U. Wallrabe, and J. G. Korvink, "Heteronuclear Micro-Helmholtz Coil Facilitates m-Range Spatial and Sub-Hz Spectral Resolution NMR of nL-Volume Samples on Customisable Microfluidic Chips," *PLOS ONE*, vol. 11, no. 1, pp. 1–16, 2016.

[48] F. Bonetto, E. Anoardo, and M. Polello, "Saddle Coils for Uniform Static Magnetic Field Generation in NMR Experiments," *Concepts in Magnetic Resonance Part B: Magnetic Resonance Engineering*, vol. 29B, no. 1, pp. 9–19, 2006.

[49] C. V. Grant, Y. Yang, M. Glibowicka, C. H. Wu, S. H. Park, C. M. Deber, and S. J. Opella, "A Modified Alderman-Grant Coil Makes Possible an Efficient Cross-Coil Probe for High Field Solid-State NMR of Lossy Biological Samples," *Journal of Magnetic Resonance*, vol. 201, no. 1, pp. 87–92, 2009.

[50] M. Jouda, S. M. Torres Delgado, M. A. Jouzdani, D. Mager, and J. G. Korvink, "ArduiTaM: Accurate and Inexpensive NMR Auto Tune and Match System," *Magnetic Resonance*, vol. 1, no. 1, pp. 105–113, 2020.

[51] A. D. Buckingham, P. Lazzeretti, and S. Pelloni, "Chiral Discrimination in NMR Spectroscopy: Computation of the Relevant Molecular Pseudoscalars," *Molecular Physics*, vol. 113, no. 13-14, pp. 1780–1785, 2015.

[52] D. B. Davidson, *Computational Electromagnetics for RF and Microwave Engineering*. Cambridge University Press, 2 ed., 2010. ISBN 0521518911.

[53] D. M. Pozar, *Microwave Engineering*. Hoboken, NJ: Wiley, 3rd ed., 2005. ISBN 0471448788.

[54] P. Garbacz, P. Fischer, and S. Krämer, "A Loop-Gap Resonator for Chirality-Sensitive Nuclear Magneto-Electric Resonance (NMER)," *The Journal of Chemical Physics*, vol. 145, no. 10, p. 104201, 2016.

[55] *RF Module User's Guide, COMSOL Multiphysics v. 5.4*. COMSOL AB, Accessed: 14-June-2024. `https://doc.comsol.com/5.4/doc/com.comsol.help.rf/RFModuleUsersGuide.pdf`.

[56] D. Hoult and R. Richards, "The Signal-to-Noise Ratio of the Nuclear Magnetic Resonance experiment," *Journal of Magnetic Resonance (1969)*, vol. 24, no. 1, pp. 71–85, 1976.

[57] Y. Chen, H. S. Mehta, M. C. Butler, E. D. Walter, P. N. Reardon, R. S. Renslow, K. T. Mueller, and N. M. Washton, "High-Resolution Microstrip NMR Detectors for Subnanoliter Samples," *Phys. Chem. Chem. Phys.*, vol. 19, no. 41, pp. 28163–28174, 2017.

[58] M. Sharma and M. Utz, "Modular Transmission Line Probes for Microfluidic Nuclear Magnetic Resonance Spectroscopy and Imaging," *Journal of Magnetic Resonance*, vol. 303, pp. 75–81, 2019.

[59] Bahl I. J., "A Designer's Guide To Microstrip Line," *Microwaves*, vol. 0, pp. 1–380, 1977.

[60] K. Gupta, R. Garg, and I. Bahl, *Microstrip Lines and Slotlines*. Artech House microwave library, Artech House, 1979. ISBN 1608075354.

[61] J. D. Jackson, *Classical Electrodynamics*. New York, NY: Wiley, 3rd ed., 1999. ISBN 047130932X.

[62] M. C. Wapler, J. Leupold, I. Dragonu, D. von Elverfeld, M. Zaitsev, and U. Wallrabe, "Magnetic Properties of Materials for MR Engineering, Micro-MR and Beyond," *Journal of Magnetic Resonance*, vol. 242, pp. 233–242, 2014.

[63] A. D. Buckingham, "Communication: Permanent Dipoles Contribute to Electric Polarization in Chiral NMR Spectra," *The Journal of Chemical Physics*, vol. 140, no. 1, p. 011103, 2014.

[64] Z. Zhang, Y. Deng, M. Hou, X. Lai, M. Guan, F. Zhang, R. Qi, and G. Qiu, "Iron/Photoredox Dual Catalysis for Acyl Nitrene-Based C-O Bond Formation towards Phthalides," *Chem. Commun.*, vol. 58, no. 98, pp. 13644–13647, 2022.

[65] Guidechem, "Thalidomid 50-35-1," Accessed: 04-March-2024. `https://www.guidechem.com/dictionary/de/50-35-1.html`.

[66] E. Tokunaga, T. Yamamoto, E. Ito, and N. Shibata, "Understanding the Thalidomide Chirality in Biological Processes by the Self-disproportionation of Enantiomers," *Scientific Reports*, vol. 8, p. 17131, Nov 2018.

[67] W.H.O, "World Health Organization Model List of Essential Medicines: 22nd list (2021)," technical documents, 2021. WHO reference no. WHO/MHP/HPS/EML/2021.02.

[68] I. Khodov, S. Efimov, V. Klochkov, G. Alper, and L. Batista de Carvalho, "Determination of Preferred Conformations of Ibuprofen in Chloroform by 2D NOE Spectroscopy," *European Journal of Pharmaceutical Sciences*, vol. 65, pp. 65–73, 2014.

[69] Sigma-Aldrich, "FT-NMR Spectra," Accessed: 04-March-2024. `https://www.sigmaaldrich.com/deepweb/assets/sigmaaldrich/quality/spectra/287/458/FNMR008613.pdf`.

[70] G. A. Morris and R. Freeman, “Enhancement of nuclear magnetic resonance signals by polarization transfer,” *Journal of the American Chemical Society*, vol. 101, no. 3, pp. 760–762, 1979.

[71] Santos, Jose I. and Rivilla, Iván and Cossío, Fernando P. and Matxain, Jon M. and Grzelczak, Marek and Mazinani, Shobeir K. S. and Ugalde, Jesus M. and Mujica, Vladimiro, “Chirality-Induced Electron Spin Polarization and Enantiospecific Response in Solid-State Cross-Polarization Nuclear Magnetic Resonance,” *ACS Nano*, vol. 12, no. 11, pp. 11426–11433, 2018.

Acknowledgement

As with all projects, the success of this dissertation would not be possible without the efforts of many who were directly or indirectly involved in this journey. Therefore, it becomes crucial to show my gratitude to them.

First to my supervisor Prof. Dr. Jan G. Korvink for his patience and generous time in allowing me to familiarise myself with the topic, and for trying out all the ideas till we finally made it. Even with his busy schedule he always had time for meetings, which led to interesting discussions. His continuous inspiration, and catchphrase "just try and see", brought the motivation to try and finally, we saw the twisted invention play its charm.

Prof. Dr. Stefan Bräse for accepting to not only co-examining my thesis but also for his interest in the topic. We will ever be grateful for your suggestions and introduction to your dynamic team members.

To all the members of the low-cost MEMs group for the discussions, suggestions and sharing of ideas during the official and unofficial meetings. Special thanks to Anna Zakhurdaeva, Dr. Omar Nassar, Dr. Emil Mamleyev, Ahsana Sadaf, Dr. Monsur Islam, Dr. Bharat Sharma and especially to Dr. Dario Mager for leading the group so uniquely. His help and suggestions to tackle all the bureaucratic and administrative efforts made things quite easy.

I would like to mention Dr. Yongbo Deng for training me in the field of topology optimisation, and his collaboration on my first paper, and Dr. Mazin Jouda, for the collaboration on my first paper, and all the corridor discussions about RF.

To all the members of Prof. Korvink's group for the group meetings, lunchtime discussions, and birthday cards.

To all the supportive staff at IMT, Heike Fornasier for training me in the clean-room fabrication process, Alexandra Moritz for perfectly done machining jobs, and Marco Heiler for agreeing to all the unconventional metal coating requests.

To my current and former colleagues at Voxalytic GmbH for their support in allowing me to work on my dissertation even during work hours. Special thanks to Dr. Ronald Kampmann who introduced me to the technique of capillary sealing without which the chances of detecting the chiral signal would be similar to detecting ^{2}H on the ^{1}H channel.

To all the people who I missed. It was not intentional, it was just the stress to finish.

I would also like to thank the funding agencies for supporting me financially during the research period, which was "Deutsche Forschungsgemeinschaft (METACOILS (grant no. KO 1883-20))" and "KIT (Virtual Materials Design, VIRTMAT)".

To all my family and friends all around the world especially, Mummy, Papa, Ramit Bhaiya, Deeksha Bhabhi, Chacha, Chachi, Samridhi, Rohan, Ritika, Saanjh, from G-17 and Mummy, Papa, Abhay, and Dadi from EC-76. Their continuous support and encouragement kept me going.

In the end, to my wife Shiti Handa for her continuous encouragement, sacrifices and for allowing me to work after hours and even on weekends. I will always be grateful to you and now let's enjoy the next phase of our life together with Shubh.